



Electrical control of spin dynamics in spin-orbit coupled ferromagnets

Timothy Skinner

Jesus College

This dissertation is submitted for the degree of Doctor of
Philosophy

April, 2014

Declaration

This dissertation is my own work and contains nothing which is the outcome of work done in collaboration with others, except where specified in the text. This dissertation is not substantially the same as any that I have submitted for a degree or diploma or other qualification at any other university. This dissertation does not exceed the prescribed limit of 60,000 words.

Abstract

This thesis describes the control of magnetisation dynamics using electricity. Direct electrical control of magnetisation is desirable for the development of efficient scalable magnetic memories. In materials with broken inversion symmetry and spin-orbit coupling, electrical current can exert a torque on a local magnetisation. In the studies presented here, a microwave current-induced ferromagnetic resonance (spin-orbit FMR) technique is used to characterise the dynamical magnetic properties and to determine the symmetries of the spin-orbit torques of ferromagnetic layers with broken inversion symmetry.

Ultra-thin ferromagnetic/heavy metal bilayers have recently become an important area of study in spintronics. Magnetic torques originating from the spin-Hall effect and a Rashba spin-orbit field have both been reported in these materials. These spin-orbit torques may allow commercialisation of magnetic random access memories with higher efficiency than previous technologies. However, the exact origin of the torques is still not well understood.

In the first study of this thesis, dynamic pumping of spin current induced by an external waveguide is used to investigate the dependence of the inverse spin-Hall effect in Co/Pt on the magnet thickness. An enhancement of the inverse-spin Hall effect is seen in devices with the thinnest cobalt layers which can not be explained by a conventional understanding of the spin-Hall effect.

In the second study, spin-orbit FMR is used to identify the symmetries of the current-induced torques in the same Co/Pt layers. Anti-damping and field-like torque symmetries are identified, consistent in thicker cobalt layers with origins from the spin-Hall effect and an Oersted field respectively. In thinner cobalt layers, an additional field-like torque opposing the Oersted torque appears, consistent with a Rashba origin.

(Ga,Mn)As is a dilute magnetic semiconductor with a record highest Curie temperature of around 180 K. At low temperatures, large spin-orbit torques with a Dresselhaus symmetry are known to exist in the material. In the final study of the thesis, spin-orbit FMR measurements demonstrate that the broken symmetry of unannealed $\text{Ga}_{0.03}\text{Mn}_{0.97}\text{As}$ can generate torques with the same Dresselhaus symmetry in an adjacent iron layer at room temperature. This enables the spin-orbit torque to be distinguished from the torque due to the spin-Hall effect by symmetry.

Acknowledgements

I would like to thank my supervisor, Dr. Andrew Ferguson, for all his help and support throughout the last three and a half years. Without his knowledge and guidance, I do not think I would have enjoyed these studies nearly as much as I have.

There are many people without whom this work would not have been possible. In particular I am indebted to: Andy Irvine and Radoslav Chakalov for all their help, particularly for training me in the cleanroom and helping with the fabrication of samples; Hide Kurebayashi for many long afternoons talking about my research and Nick Lambert for many discussions, particularly everything to do with microwaves. I am grateful to everyone who has helped me in the lab, particularly Dong Fang, Chiara Ciccarelli and Lucy Cunningham. Thanks also to Vahe Tshitoyan for his help with proofreading.

I have many collaborators to thank, particularly those at the University of Nottingham for growing all of the materials. In particular, Richard Champion for all the beautiful (Ga,Mn)As samples; Mu Wang, Andrew Rushforth and Aidan Hindmarch for the Co/Pt sputtering as well as all the additional SQUID and XRR measurements. Kamil Olejník in Prague helped me enormously by making some excellent Fe/(Ga,Mn)As samples.

I could not have chosen a more welcoming place to work than in the Microelectronics group. I would like to thank Adam, Andi, Chiara, Fernando, James, Julia, Megan, Nick and Vahe for all their companionship in the lab and in the pub.

Finally, I must thank my parents who have been so encouraging throughout all of my studies and Jessica who has been supportive and patient with me for the past few years and throughout the writing of this dissertation.

List of publications

- [1] D. Fang, **T. D. Skinner**, H. Kurebayashi, R. P. Campion, B. L. Gallagher, and A. J. Ferguson. Electrical excitation and detection of magnetic dynamics with impedance matching. *Appl. Phys. Lett.* **101**, 182402 (2012).
- [2] H. Kurebayashi, **T. D. Skinner**, K. Khazen, K. Olejník, D. Fang, C. Ciccarelli, R. P. Campion, B. L. Gallagher, L. Fleet, A. Hirohata and A. J. Ferguson. Uniaxial anisotropy of two-magnon scattering in an ultrathin epitaxial Fe layer on GaAs. *Appl. Phys. Lett.* **102**, 062415 (2013).
- [3] **T. D. Skinner**, H. Kurebayashi, D. Fang, D. Heiss, A. C. Irvine, A. T. Hindmarch, M. Wang, A. W. Rushforth, and A. J. Ferguson. Enhanced inverse spin-Hall effect in ultrathin ferromagnetic/normal metal bilayers. *Appl. Phys. Lett.* **102**, 072401 (2013).
- [4] **T.D. Skinner**, M. Wang, A.T. Hindmarch, A.W. Rushforth, A.C. Irvine, D. Heiss, H. Kurebayashi and A.J. Ferguson. Spin-orbit torque opposing the Oersted torque in ultrathin Co/Pt bilayers. *Appl. Phys. Lett.* **104**, 062401 (2014).
- [5] H. Kurebayashi, Jairo Sinova, D. Fang, A. C. Irvine, **T. D. Skinner**, J. Wunderlich, V. Novak, R. P. Campion, B. L. Gallagher, E. K. Vehstedt, L. P. Zarbo, K. Vyborny, A. J. Ferguson and T. Jungwirth. An antidamping spin-orbit torque originating from the Berry curvature. *Nature Nanotechnol.* **9**, 211-217 (2014).

Contents

1	Introduction	1
2	Theoretical background	5
2.1	Magnetic anisotropy	5
2.1.1	Shape anisotropy	5
2.1.2	Magnetocrystalline anisotropy	6
2.1.3	Magnetic switching	8
2.2	Magnetisation dynamics	8
2.2.1	FMR	8
2.2.2	FMR in thin films	10
2.3	Magneto-transport	11
2.3.1	Anisotropic magnetoresistance	12
2.3.2	Anomalous Hall effect	12
2.3.3	Tunnel magnetoresistance	13
2.4	Spin-current and the spin-transfer torque	14
2.4.1	Spin filtering	14
2.4.2	Spin-Hall effect	16
2.4.3	Spin-pumping and inverse spin-Hall effect	17
2.5	Current-induced spin-accumulation	18
2.5.1	Dresselhaus spin-orbit interaction	19
2.5.2	Rashba spin-orbit interaction	19
2.5.3	Response to current	20
2.6	Ferromagnets with inversion-asymmetry	21
2.6.1	Dilute magnetic semiconductors	21
2.6.2	Metal bilayers	23

3	Experimental methods	25
3.1	Spin-orbit FMR	25
3.2	Electromagnet system	29
3.2.1	Field calibration	30
3.2.2	Hysteresis	36
3.3	Clean room fabrication	37
3.3.1	Electron-beam lithography	37
3.3.2	Ion-beam milling	38
3.3.3	Bond pad evaporation	38
3.3.4	Sample mounting	39
4	Spin-pumping in Co/Pt bilayers	41
4.1	Device fabrication	41
4.2	Detection of resonance	42
4.3	Calculating the pumped spin-current	48
4.4	Calculating the spin-Hall angle	51
5	Current induced torques in Co/Pt bilayers	55
5.1	SO-FMR in Co/Pt bilayers	56
5.2	Results and analysis	59
5.3	Heating calibration	68
5.4	Conclusions	70
6	A room temperature crystal spin-orbit torque	73
6.1	SO-FMR in Fe/(Ga,Mn)As bilayers	75
6.2	Results and analysis	76
6.3	Calibration of current-induced torques	80
6.4	Efficiency of the bulk torques	81
6.5	Calibration of the spin-Hall angle	84
6.6	Discussion	85
6.7	Conclusions	87
7	Conclusions and outlook	89
	Appendices	91

A	Impedance matching	93
A.1	Microstrip resonators	94
A.1.1	Loaded half-wavelength resonator	95
A.2	Measurements of half-wavelength resonators	95
A.3	Compact microstrip resonators for FMR	97
A.3.1	Shunted quarter-wavelength resonators	98
A.3.2	Inverted half-wavelength resonators	102
A.4	Q factor calibration	105
A.4.1	Series resonator	105
A.4.2	External coupling	106
A.4.3	Calibration using half-wavelength microstrip resonators . . .	109
A.5	Effects of sample substrate	110
A.6	Conclusions	111
	Bibliography	113

Chapter 1

Introduction

A number of research areas can be brought together within the term ‘spintronics’. Most broadly defined, spintronics research is the study of the properties of electron and nuclear spins, with the aim of using the additional spin degree of freedom to create electronic devices with higher efficiencies and new functionalities.¹ This encompasses fields such as quantum information processing, in which the quantum states of single spins can be manipulated and entangled.² However, spintronics is more often thought of as the study of the collective behaviour of many spins.

In this latter area, which we might refer to as macroscopic spintronics, the behaviour of a spin population can be measured in simple magneto-transport properties.* At first glance, it might seem remarkable that we can see the effects of quantum mechanical spin on a macroscopic scale. However, ferromagnetism itself is a macroscopic effect, known since ancient times,[†] which is the result of spin.[‡] The spontaneous alignment of the individual electron magnetic moments can only arise because of the existence of the electron spin and the Pauli exclusion principle.⁶

The success story of spintronics research so far has been the development of ultra-sensitive field sensors now ubiquitous in hard drives, started by Albert Fert and Peter Grünberg’s Nobel prize-winning discovery of giant magnetoresistance in 1988.^{7,8} Further advancements in read-head field sensors have continued with

*For example, the anomalous Hall effect and the anisotropic magneto-resistance.

†For example, see the works of Roman poet Titus Lucretius Carus.³

‡Magnetism in solids is a purely quantum mechanical effect which can not arise classically. This is the Bohr-van Leeuwen theorem first shown in the doctoral dissertations of Niels Bohr⁴ and Hendrika Johanna van Leeuwen⁵

research into tunnelling magnetoresistance.^{9–13} Many other possible spintronic devices have been outlined by researchers,[§] including those for spin-based logic, which have yet to be realised. However, an area which has made significant technological progress in recent years is spin-based memory. These memories possess additional functionalities such as non-volatility, which provides devices which are fast to write but which have low power consumption. This thesis fits broadly into this latter area of research and the key topic: the electrical control of magnets.

The simplest way to control a magnet using electricity is by using the Oersted field generated around a current-carrying wire. Unfortunately, memory technologies built on this effect quickly reach scaling limits as, below a certain size, the Oersted fields start writing neighbouring magnetic bits. As a ferromagnet can simplistically be thought of as a collection of ordered spins, an important question to ask is whether we can manipulate magnets by interactions with other spins. Slonczewski first proposed in 1996 that a current, spin-polarised by a ferromagnet, could exert a torque when injected into another magnet.¹⁵ This torque is known as the spin-transfer-torque (STT), because angular momentum of the flowing spins is transferred to the magnetisation.¹⁶ The prediction and experimental observation of this torque was a major achievement in the development of spintronic memories. Indeed, magnetic random access memory (MRAM) using the STT has already been brought to market by Everspin Technologies.¹⁷

It was only a decade ago that the spin-Hall effect¹⁸ (SHE) was first experimentally verified,^{19,20} having been predicted by Dyakanov and Perel in 1971.^{21,22} In the SHE, pure spin-currents (the net flow of spin angular momentum without charge-current) are generated in perpendicular directions to a charge-current. Recent research by Liu *et al.* in ferromagnet/heavy metal bilayers has shown a sizeable spin-current, generated by the SHE in the heavy metal layer, exerting a STT on the adjacent ferromagnet.²³ Compared to the previous generation of MRAMs based on the STT in magnetic tunnel junctions (MTJs), MRAMs based on these bilayers may be more efficient due to the lower current densities needed for writing and more reliable due to the physical separation of the read and write currents.²⁴

The STT is not, however, the only way to electrically manipulate a magnet. The spin-Hall effect is itself a consequence of spin-orbit coupling. The spin-orbit

[§]For examples, see these reviews by Wolf *et al.*¹ and Žutić *et al.*¹⁴

coupling is a relativistic term in the single-spin Hamiltonian which couples the orbital and spin angular momentum. One consequence of this coupling is that in a non-centrosymmetric potential, the degeneracy of the spin states is split as a function of the linear momentum of the particle.^{25–28} The accumulation of spins in a majority state which results from passing a current through such a potential is known as the inverse spin-galvanic or Edelstein effect.^{29,30} Torques arising from the exchange interaction between this spin-accumulation and local magnetic moments were first demonstrated by Chernyshov *et al.* in (Ga,Mn)As,³¹ a low-temperature magnetic semiconductor which has a non-centrosymmetric crystal structure.

These torques can be measured using low-frequency or dc techniques, where the magnetisation deflection^{32–37} or switching^{31,38–44} is measured as a response to current, or by using microwave frequency currents to induce ferromagnetic resonance (FMR).^{23,45–49} This latter technique, spin-orbit FMR (SO-FMR), not only allows sensitive determination of the symmetry of the current-induced torques which excite the resonance, but also provides information about the equilibrium and dynamic properties of the ferromagnet.

Torques in ultra-thin ferromagnet/heavy metal bilayers have also been attributed to the Edelstein effect.^{39,40,50} The inversion-asymmetry of the interface can potentially induce a spin-accumulation in the ferromagnet with ‘Rashba’ symmetry. However, this effect can not be easily distinguished from a SHE-STT by symmetry. Simplistically, the STT is an anti-damping torque; a magnetisation dependent torque that can induce precession by opposing the magnetisation damping. Contrastingly, the exchange coupling between the spin-accumulation and magnetisation should exert a field-like torque. However, in magnetic tunnel junctions with ultra-thin ferromagnets, the spin-transfer torque is known to have a significant field-like component.^{51–53} Equally, it was recently shown in (Ga,Mn)As that the spin-accumulation has an associated anti-damping symmetry component, due to precession of the spins around the sum of the magnetisation and spin-orbit fields as they are accelerated under the applied electric field.⁴⁹ Therefore, by symmetry, either effect can explain the observed field-like and anti-damping torques.

The thermodynamically reciprocal effect to the STT is often studied in bilayer systems. This process, in which a precessing magnetisation can induce a spin-current in a neighbouring layer, is known as spin pumping.^{54–57} This dynamic exchange of spin angular momentum at the interface can achieve higher

spin-injection efficiencies into semiconductors than through ferromagnetic ohmic contacts.⁵⁸ The pumped spin-current is normally measured in these experiments by the inverse spin-Hall effect, in which a spin-current generates a perpendicular charge-current.⁵⁹ In Chapter 4, spin pumping is investigated in ultra-thin Co/Pt bilayers, where an inverse Edelstein effect may also contribute to the detected charge-current.

To distinguish the Rashba torques and STT in ferromagnet/heavy metal bilayers, there have been some studies where the strength of the torques have been measured as a function of layer thicknesses.^{33,58} In Chapter 5, SO-FMR is used to measure the torques in ultra-thin Co/Pt bilayers as a function of Co thickness. As the Co thickness is reduced, a field-like torque increasingly opposes the Oersted torque, consistent with the emergence of a Rashba field. However a contribution from a field-like component of the SHE-STT can not be ruled out.

In Chapter 6, a torque originating from the Edelstein effect in a room temperature (Ga,Mn)As layer is observed in an adjacent iron layer. Unlike ferromagnetic/heavy metal bilayers, this torque can be unambiguously distinguished from the accompanying SHE-STT due to the cubic crystal symmetry of the spin-accumulation. This is the first reported room temperature spin-orbit torque arising from a non-centrosymmetric crystal. The observation of this torque should motivate studies of room temperature single-layer ferromagnets with a broken inversion symmetry.

Chapter 2

Theoretical background

This chapter is intended to introduce the reader to the physics explored in this thesis as well as most of the mathematics used in the later experimental chapters.

2.1 Magnetic anisotropy

Magnetic anisotropy describes how the energy required for a magnetisation to lie in a particular direction varies in space. There are two main sources of anisotropy: the shape of the sample and the crystal structure. Later, in Chapter 4, we will see that there can also be an anisotropy due to the interfaces of the material.

2.1.1 Shape anisotropy

The demagnetisation field is the magnetic field produced from a ferromagnet, originating from the long range magnetic interaction of the surface dipoles. For a magnetised sphere, the demagnetisation energy is independent of the direction of the magnetisation. However, for a non-spherical object, the reduced symmetry means that the strength of the demagnetisation field, and therefore the demagnetisation energy, varies with the magnetisation direction. For an elliptical object the demagnetising field is given by,⁶⁰

$$\mathbf{H}_d = -\mathcal{N}\mathbf{M}, \tag{2.1}$$

where \mathbf{M} is the magnetisation vector and \mathcal{N} is a shape-dependent tensor. For a thin film, the only non-zero tensor element is perpendicular to the plane: $\mathcal{N}_\perp = 1$. The magnetostatic demagnetisation energy density is given by the volume integral,

$$F_d = -\frac{\mu_0}{2V} \int \mathbf{H}_d \cdot \mathbf{M} dv, \quad (2.2)$$

which for a thin film gives a shape anisotropy energy density of⁶¹

$$F_d = \frac{1}{2} \mu_0 M^2 \cos^2 \psi, \quad (2.3)$$

where the magnetisation is at an angle ψ from the normal to the plane.

2.1.2 Magnetocrystalline anisotropy

The magnetocrystalline anisotropy terms arise from the spin-orbit coupling of the magnetic moments with the crystal electric potential. Hence the symmetry of the lattice leads to a particular set of magnetocrystalline anisotropies. The two common types of crystal anisotropy are cubic and uniaxial.

Cubic anisotropy

Cubic crystal structures can exhibit cubic anisotropy with three orthogonal easy axes determined by the cubic lattice vectors. The anisotropy energy density is parametrised by a power series of the cosines of the angles between the cubic lattice vectors and the magnetisation⁶²

$$F_B = F_{B0} + K_4(\alpha_1^2 \alpha_2^2 + \alpha_2^2 \alpha_3^2 + \alpha_3^2 \alpha_1^2) + K_6(\alpha_1^2 \alpha_2^2 \alpha_3^2) + \dots, \quad (2.4)$$

where α_1, α_2 and α_3 are the cosines. In spherical polar coordinates (as defined in Figure 2.1), to the lowest order this simplifies to

$$F_B = F_{B0} + \frac{1}{4} K_4 (\sin^4 \psi \sin^2 2\phi + \sin^2 2\psi). \quad (2.5)$$

For epitaxially grown layers on a substrate with different lattice parameters, for example (Ga,Mn)As grown on GaAs, there exists a lattice-mismatch strain which breaks the symmetry between the in-plane and perpendicular axis. This modifies

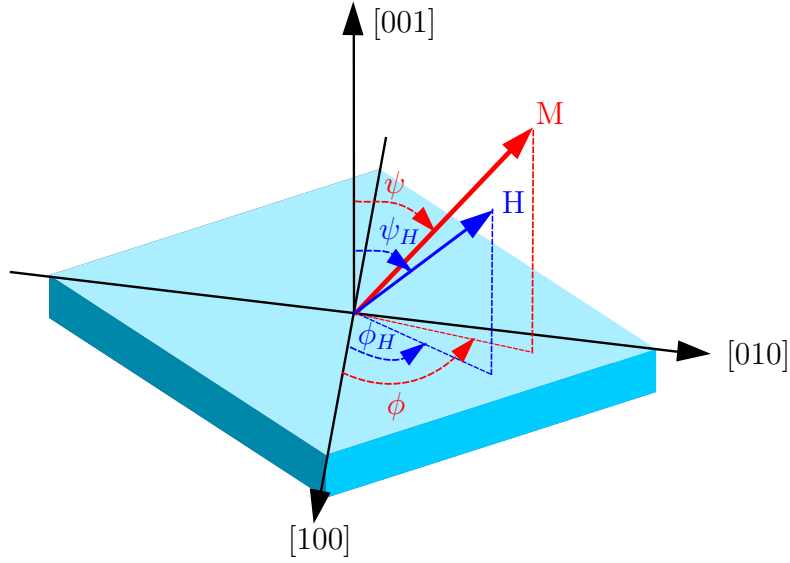


Figure 2.1: Angles used to define the position of the magnetisation and external field relative to the crystal.

the cubic anisotropy. First note that $\alpha_1^2\alpha_2^2 + \alpha_2^2\alpha_3^2 + \alpha_3^2\alpha_1^2 \equiv \frac{1}{2} - \frac{1}{2}(\alpha_1^4 + \alpha_2^4 + \alpha_3^4)$. The cubic anisotropy can now be described by two parameters, $K_{4\parallel}$ and $K_{4\perp}$, so that the cubic anisotropy in, and perpendicular to, the plane can be distinguished:⁶³

$$F_B = F_{B0'} - \frac{1}{2}K_{4\parallel}(\alpha_1^4 + \alpha_2^4) - \frac{1}{2}K_{4\perp}\alpha_3^4. \quad (2.6)$$

With some trigonometric manipulation the more commonly used expression,

$$F_B = F_{B0'} - \frac{1}{2}K_{4\parallel}\frac{1}{4}(3 + \cos 4\phi)\sin^4\psi - \frac{1}{2}K_{4\perp}\cos^4\psi, \quad (2.7)$$

is found.

Uniaxial anisotropy

Uniaxial anisotropy describes a preference for the magnetisation to lie in one particular direction. The anisotropy energy density can be described by a power series of the sine of the angle between the magnetisation and the uniaxial easy axis⁶⁴

$$F_U = F_{U0} + K_2 \sin^2 \theta + K_4 \sin^4 \theta + \dots \quad (2.8)$$

Usually only the lowest order term, K_2 is used. Apart from a crystal origin, a uniaxial anisotropy can also arise from a strain in the material or an interface.

2.1.3 Magnetic switching

Magnetic storage relies on magnetic anisotropies to retain a magnetisation along a particular easy axis. When designing technologies based on magnetic switching the figure of merit for storage is thermal stability, given by $F_{\text{ani}}V/k_{\text{B}}T$, where V is the magnetic volume. Whilst smaller values require less energy for switching, values > 40 are typically needed for MRAMs to reliably retain their state between operations.⁶⁵

A key development in magnetic tunnel junction (MTJ) MRAM technology was to engineer the easy axis of the free layer to be out-of-plane.⁶⁶ In this configuration, the out-of-plane uniaxial anisotropy is the only barrier to switching in the system, and this reduces the overall torque needed to write the magnetisation.⁶⁷

2.2 Magnetisation dynamics

2.2.1 FMR

Ferromagnetic Resonance (FMR) is a powerful technique often used to characterise the magnetic properties of a material. The principle of FMR is similar to that of nuclear magnetic resonance (NMR) or electron spin-resonance (ESR), but in FMR, resonant precession is driven in the magnetisation of the sample instead of the nuclear magnetic moments or unpaired electron spins. In NMR (or ESR), for a spin-half nucleus (or electron), the energy splitting of the up and down spin states in a magnetic field is given by $\Delta E = \gamma\hbar\mu_0H$, where γ is the gyromagnetic ratio of the particle in its particular environment. There is a peak in absorption of photons with energy $\hbar\omega = \Delta E$ as the energy of the photon matches the energy splitting of the spin states. The resonant frequency is then simply described by the Larmor frequency⁶⁸

$$\omega = \gamma\mu_0H, \tag{2.9}$$

where H is an externally applied field. However, in FMR, the precession is complicated by the magnetic anisotropies of the sample, which create effective internal

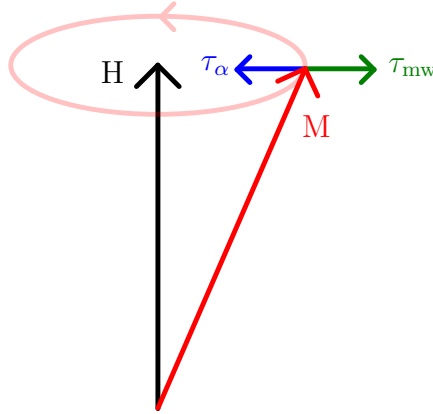


Figure 2.2: During FMR, a driving microwave field, τ_{mw} , balances the damping torque, τ_α , allowing the magnetisation, M , to precess around the external field.

magnetic fields. Hence the precession occurs around an effective magnetic field vector.

Conventionally in FMR, the magnetisation is saturated along a vector by a large external field. The sample is held in a microwave cavity and, at resonance, a microwave field excites precession around the external field vector at the resonant frequency of the cavity and sample. Resonance is achieved by varying the strength of the external field until the resonant frequency of the sample matches the cavity. Resonance is measured as a peak in absorption of the incident microwaves.

In the regime where the external field saturates the magnetisation, the microwave field can be treated as a small perturbing field, with a corresponding small perturbation in the magnetisation. The precession of the magnetisation is well described by the phenomenological Landau-Lifshitz-Gilbert (LLG) equation⁶⁹

$$\frac{\partial \mathbf{m}}{\partial t} = -\mu_0 \gamma \mathbf{m} \times \mathbf{H}_{\text{eff}} + \alpha \mathbf{m} \times \frac{\partial \mathbf{m}}{\partial t}, \quad (2.10)$$

where $\mathbf{m} = \mathbf{M}/M_S$, a dimensionless parameter.

The first term on the right hand side of the equation is similar to the torque acting on individual magnetic moments in Larmor precession, but in this case the torque is acting on the overall magnetisation vector. The second term is the Gilbert damping which describes the dissipation of energy in the system. γ is the gyromagnetic ratio of the magnetic moments, and α is the Gilbert damping parameter; a material parameter which has to be experimentally measured. A

schematic of the FMR precession and the torques acting on the magnetisation is shown in Fig. 2.2. The effective magnetic field, \mathbf{H}_{eff} , represents the external and microwave magnetic fields and effective fields from the magnetic anisotropies of the material. It can be found from the functional derivative of the free energy density with respect to the magnetization:⁷⁰

$$\mathbf{H}_{\text{eff}} = -\frac{1}{\mu_0} \nabla_{\mathbf{M}} F. \quad (2.11)$$

Smit and Beljers developed an approach where the resonance condition for any field can be found independently of the damping parameter, from the free energy density of the system:⁷¹

$$\left(\frac{\omega}{\gamma}\right)^2 = \frac{1}{M_S^2 \sin^2 \psi} \left[\frac{\partial^2 F}{\partial \psi^2} \frac{\partial^2 F}{\partial \phi^2} - \left(\frac{\partial^2 F}{\partial \psi \partial \phi} \right)^2 \right], \quad (2.12)$$

where the angles of the magnetisation relative to the crystal are defined as in Figure 2.1.

2.2.2 FMR in thin films

The free energy density of a thin magnetic film can be described generally as⁶¹

$$F = \frac{1}{2} \mu_0 M \left\{ -2H [\cos \psi \cos \psi_H + \sin \psi \sin \psi_H \cos(\phi - \phi_H)] + (M - H_{2\perp}) \cos^2 \psi - \frac{1}{2} H_{4\perp} \cos^4 \psi - \frac{1}{2} H_{4\parallel} \frac{1}{4} (3 + \cos 4\phi) \sin^4 \psi - H_{2\parallel} \sin^2 \psi \cos^2(\phi - \phi_{2\parallel}) \right\}, \quad (2.13)$$

where the first term is the Zeeman energy; the second is the shape anisotropy and the perpendicular uniaxial anisotropy; and the other three terms are magnetocrystalline cubic and in-plane uniaxial anisotropy terms. The effective magnetic anisotropy fields are given by their corresponding anisotropy energies, $H_i = 2K_i/\mu_0 M_S$. As the symmetry of the shape and perpendicular uniaxial anisotropies are the same they are often written as $M_{\text{eff}} = M - H_{2\perp}$

Using equations 2.12 and 2.13, and for an arbitrary angle minimising the free energy with respect to ψ and ϕ , we can derive the angle-dependent resonant fre-

quency of the ferromagnetic precession (Kittel's equation)⁷²

$$\left(\frac{\omega}{\gamma}\right)^2 = \mu_0^2 [(aH_{\text{res}} + H_1)(aH_{\text{res}} + H_2) - H_3^2], \quad (2.14)$$

where

$$\begin{aligned} a &= \cos \psi \cos \psi_H + \sin \psi \sin \psi_H \cos(\phi - \phi_H), \\ H_1 &= - (M_{\text{eff}} + H_{2\parallel} \cos^2(\phi - \phi_{2\parallel})) \cos 2\psi \\ &\quad + H_{4\perp} \frac{\cos 2\psi + \cos 4\psi}{2} + H_{4\parallel} \frac{\cos 4\psi - \cos 2\psi}{2} \frac{3 + \cos 4\phi}{4}, \\ H_2 &= - M_{\text{eff}} \cos^2 \psi + H_{4\parallel} \sin^2 \psi \left(\cos 4(\phi - \phi_{4\parallel}) - \cos^2 \psi \frac{3 + \cos 4\phi}{4} \right) \\ &\quad + H_{4\perp} \cos^4 \psi + H_{2\parallel} \left(\sin 2(\phi - \phi_{2\parallel}) - [\cos \psi \cos(\phi - \phi_{2\parallel})]^2 \right) \end{aligned}$$

and

$$H_3 = \frac{1}{2} \cos \psi \left(\frac{3}{2} H_{4\parallel} \sin 4\phi \sin^2 \psi + H_{2\parallel} \sin 2(\phi - \phi_{2\parallel}) \right). \quad (2.15)$$

For a polycrystalline thin film, this is greatly simplified due to the absence of the magneto-crystalline anisotropies, and the resonance condition can be expressed as

$$\left(\frac{\omega}{\gamma}\right)^2 = \mu_0^2 (H_{\text{res}} - M_{\text{eff}} \cos 2\psi) (H_{\text{res}} - M_{\text{eff}} \cos^2 \psi). \quad (2.16)$$

2.3 Magneto-transport

Because of the fundamentally relativistic nature of electromagnetism, charged particles experience a force due to what we classically think of as electric and magnetic fields. This force, $\mathbf{F} = q(\mathbf{E} + \mathbf{v} \times \mathbf{B})$, is the Lorentz force that we are familiar with. When considering electron transport, the action of a perpendicular magnetic field is to deflect the charge carriers in a transverse direction, leading to a transverse resistance, $\rho_{xy} = R_H H_z$, where R_H is the Hall coefficient. However, in samples with magnetisation, the relativistic spin-orbit coupling term in the Hamiltonian allows interaction between the spin- $\frac{1}{2}$ charge carriers and magnetisation. The electrical

transport in magnetic materials can then depend on the internal magnetisation direction as well as the external magnetic field. These magneto-transport effects are experimentally very important for measuring magnetisation direction and strength. Below, we will study two of these effects as well as the tunnel magnetoresistance, which does not rely on spin-orbit coupling but instead relies upon the tunnelling current between two ferromagnets.

2.3.1 Anisotropic magnetoresistance

The anisotropic magnetoresistance (AMR) was first measured by William Thomson in 1856,⁷³ when he observed an increase in the longitudinal resistance of iron and nickel with a magnetic field applied longitudinally, and a decrease with a field applied transversely. The longitudinal resistivity can be formulated as⁷⁴

$$\rho_{xx} = \rho_{\perp} + (\rho_{\parallel} - \rho_{\perp}) \cos^2 \theta, \quad (2.17)$$

where θ is the angle between the magnetisation and current. There is also a corresponding term in the transverse resistivity, given by⁷⁵

$$\rho_{xy} = -(\rho_{\parallel} - \rho_{\perp}) \cos \theta \sin \theta, \quad (2.18)$$

which is known as the planar Hall effect.

The resistance in most 3d ferromagnets is dominated by s-d inter-band scattering.⁷⁶ The anisotropy in this scattering, which leads to the magnetoresistance effect, is thought to be due to the symmetry-breaking of the spin-orbit coupling.⁷⁷ The size of the AMR effect is defined by the magnetoresistance ratio $(\rho_{\parallel} - \rho_{\perp})/\rho_{av}$, where $\rho_{av} \equiv \frac{1}{3}\rho_{\parallel} + \frac{2}{3}\rho_{\perp}$.⁷⁴

2.3.2 Anomalous Hall effect

Since 1930,⁷⁸ the Hall resistivity in a ferromagnet has been known to have an additional contribution, that is proportional to the perpendicular magnetisation⁷⁹

$$\rho_{xy} = R_H H_z + R_s M_z. \quad (2.19)$$

Note that this is not an additional term due to the additional magnetic field from the magnetisation of the sample, but is an intrinsic property of the material, independent of the external field.

The anomalous Hall effect (AHE) can have extrinsic contributions from the spin-dependent scattering of impurities in the material. Within this extrinsic contribution there are two competing scattering mechanisms: skew scattering⁸⁰ and side-jump⁸¹ scattering. There is also an intrinsic anomalous Hall effect⁸² which can be viewed as a consequence of the Berry-phase curvature of the band structure.⁸³ The contributions of each mechanism can be distinguished by their dependence on ρ_{xx} .⁷⁹ Fundamentally, all of these mechanisms rely on the spin-orbit coupling, which is present either intrinsically or from extrinsic impurities.

2.3.3 Tunnel magnetoresistance

The AMR and AHE are very useful experimentally because, by measuring the magnetisation dependence of ρ_{xx} and ρ_{xy} , the magnetisation vector can be read out. However, for technological purposes these effects are very small (typically less than 5% at room temperature⁷⁴). In magnetic memories they are superseded by other magnetoresistive effects such as giant magnetoresistance (GMR)^{7,8} and tunnel magnetoresistance (TMR)⁸⁴, which involve multiple ferromagnets.

TMR is the magnetoresistance that occurs across a MTJ, consisting of two ferromagnets separated by an insulating barrier. The insulating barrier dominates the transport characteristics so that the resistance is determined by the tunnelling rates across the barrier. The tunnelling rate for each spin-band is primarily determined by the density of states of the spin-band at the Fermi energy in each ferromagnet.

In the Jullière model, the tunnelling rate for a particular spin-band (in this case up), from magnetic layer 1 to magnetic layer 2, is proportional to the product of the Fermi energy density of states in the two magnets, $\mathcal{D}_{\uparrow,1}(E_F)\mathcal{D}_{\uparrow,2}(E_F)$.⁸⁵ When the magnetic layers are parallel aligned, the tunnelling is dominated by the majority spins, and the overall conductance is higher than in the anti-parallel configuration. The polarisation of a single ferromagnetic layer is, in this model, given by⁸⁶

$$P = \frac{\mathcal{D}_{\uparrow}(E_F) - \mathcal{D}_{\downarrow}(E_F)}{\mathcal{D}_{\uparrow}(E_F) + \mathcal{D}_{\downarrow}(E_F)}. \quad (2.20)$$

This allows the magnetoresistance ratio to be defined as⁸⁷

$$\text{TMR} = \frac{2P_1P_2}{1 - P_1P_2}, \quad (2.21)$$

where P_1 and P_2 are the conduction spin polarisation of the two ferromagnets, defined in equation 2.22.

TMR allows the read-out of the magnetisation of a ferromagnet by reference to a fixed magnetic layer. TMR ratios can be much larger than those of the AMR (the current record is 1010%⁸⁸), and MTJs have already found technological uses as field sensors in the magnetic read-heads of hard-drives, as well as in MRAMs.

2.4 Spin-current and the spin-transfer torque

A major challenge in spintronics is the efficient generation of spin-polarised and pure spin-currents. Pure spin-currents do not suffer the Joule heating losses of a charge-current, because there is no flow of charge. For this reason, sometimes spin-currents are referred to as ‘dissipationless’.⁸⁹ This is not strictly true, as spin is not a conserved quantity in the presence of spin-orbit coupling or other interactions (for instance, exchange coupling with magnets). These interactions can actually be useful, firstly in generating the spin-currents, but also for using the spin-currents to manipulate magnets. Described below are three ways used to create spin-polarised or pure spin-currents, and how the interaction of spin-current and magnetisation leads to the spin-transfer torque.

2.4.1 Spin filtering

When a non-spin-polarised current (that is, a current with no net spin vector) passes through a spin filter, the result is that it acquires a degree of spin polarisation, defined by⁹⁰

$$P = \frac{n_{\uparrow} - n_{\downarrow}}{n_{\uparrow} + n_{\downarrow}}, \quad (2.22)$$

where n_{\uparrow} and n_{\downarrow} are the number densities of the conducting electrons or holes in the spin sub-bands .

A simple spin filter can be made from a single ferromagnet because of its spin-dependent electronic properties. For instance, when injecting carriers into Fe from Cr, the minority spins are more likely to be transmitted. This is because of differences in scattering at the interface caused by a mismatch in the band-structure.⁹¹

Spin filtering is exploited in MTJs to generate a spin-polarised current which can reorientate a free magnetic layer. The first magnetic layer is ‘pinned’ by an antiferromagnetic layer, and spin-polarises the current along the magnetisation direction.⁹² An insulating tunnel barrier separates the ferromagnets and allows the magnetic state to be read out by TMR.

An insulator such as MgO can filter wave-functions depending on their symmetries.^{10,93} In the right combination of magnet and insulator, one spin-band will have the preferred symmetry and the other will be filtered very strongly. A ferromagnet/insulator/ferromagnet configuration such as CoFeB/MgO/CoFeB can produce a very large TMR ratio of up to 1010%,⁸⁸ which indicates excellent spin filtering.

The spin-polarised current, filtered by the pinned ferromagnet, exerts a torque on the second ferromagnet when the two magnetisations are not co-linear. This is the spin-transfer torque, and is the result of angular momentum conservation.¹⁶ In the second ferromagnet, the spin-polarised current is again filtered, and the spins of the charge carriers rotate to follow the magnetisation. This process necessitates a flow of angular momentum between the spins and magnetisation, and hence the spins must exert a torque on the magnetisation.

The generalised spin-transfer torque can be formulated (for an in-plane magnetisation) as an in-plane and out-of-plane torque⁵¹

$$\mathbf{T}_S = a\mathbf{M}_f \times (\mathbf{M}_p \times \mathbf{M}_f) + b\mathbf{M}_p \times \mathbf{M}_f. \quad (2.23)$$

\mathbf{M}_f and \mathbf{M}_p are the magnetisations of the free and pinned layers respectively. The first term is the Slonczewski torque,¹⁵ also known as the adiabatic or anti-damping torque. Usually the Slonczewski torque dominates the second torque (the non-adiabatic or field-like torque), although this second torque can become significant in MTJs, particularly at high bias.⁹⁴ A vector diagram of the magnetisations and torques is shown in Fig. 2.3.

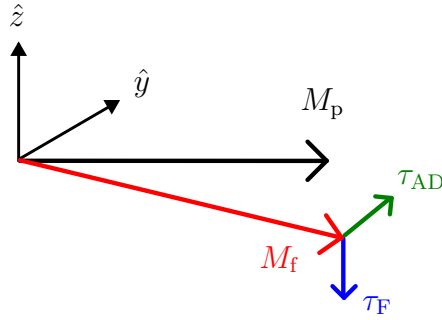


Figure 2.3: The spin-transfer torque acting on the free magnetisation, M_f , consists of an anti-damping torque, τ_{AD} and a field-like torque, τ_F .

2.4.2 Spin-Hall effect

In contrast to spin-filtering, which can spin-polarise a current, in the spin-Hall effect a longitudinal charge-current generates a perpendicular pure spin-current.¹⁸ A pure spin-current can be defined as the flow of spins without a net flow of charge.

The spin-Hall effect has its origins in the spin-orbit coupling. A distinction can be made between the intrinsic and extrinsic spin-Hall effects. In the extrinsic spin-Hall effect, because of spin-orbit coupling, spins are selectively scattered from impurities in the material through side-jump and skew scattering mechanisms.⁹⁵ In the intrinsic effect,⁸⁹ the Berry curvature, derived from the band structure,^{96,97} can make a contribution to the spin-Hall effect if there exists an electric potential with inversion-asymmetry.

The spin-Hall angle is a dimensionless number which describes the efficiency of the conversion between charge-current and spin-current

$$\theta_{SH} = \frac{2e}{\hbar} \frac{J_S}{J_C}, \quad (2.24)$$

where J_S is the spin-current density.

Reports of large spin-Hall angles have generated much interest in the technological applications of the spin-Hall effect in heavy metals. Spin-Hall angles of 1-8% in platinum,⁹⁸ 12-15% in tantalum²⁴ and more recently, 30% in tungsten⁴⁶ have been reported. Devices have been demonstrated which replace the spin-filtering ferromagnet in a MTJ with a paramagnetic layer with large θ_{SH} . The pure spin-current can then directly drive a spin-transfer torque in an adjacent magnetic layer. These devices have a major advantage over conventional MTJs in that the read

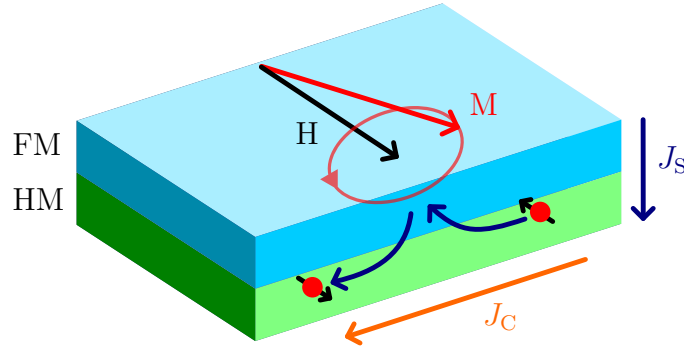


Figure 2.4: A precessing magnetisation, M , in a ferromagnetic (FM) layer, loses angular momentum to an adjacent heavy metal (HM) layer by inducing a transverse spin-current, J_S . The inverse spin-Hall effect in the heavy metal layer generates a longitudinal charge-current, J_C , from the spin-current.

and write paths are separated, improving device reliability.²⁴

2.4.3 Spin-pumping and inverse spin-Hall effect

We have seen that a spin-current can impart a torque on a magnetic layer, causing the magnetisation to precess. The reverse is also true; a precessing magnetisation is a source of spin-current for an adjacent, non-magnetic layer.^{99,100} This process is called spin-pumping, because by causing the magnetisation to precess, one can ‘pump’ spins into an adjacent layer. This loss of angular momentum from the precessing magnetisation to the normal metal layer can be observed as enhanced damping.¹⁰¹

The expression for the pumped spin-current is given by¹⁰²

$$J_S = \frac{\omega}{2\pi} \int_0^{2\pi/\omega} \frac{\hbar g^{\uparrow\downarrow}}{4\pi M_S^2} \left[\mathbf{M}(t) \times \frac{d\mathbf{M}(t)}{dt} \right]_x dt, \quad (2.25)$$

where x is the direction of the precession axis. $g^{\uparrow\downarrow}$ is the spin mixing conductivity, a constant describing the transmission of the spin-current across the ferromagnet/normal metal interface.

Typically, spin-pumping is detected via the inverse spin-Hall effect (see Fig. 2.4). Because of thermodynamic reciprocity, if a material has a spin-Hall effect, it will also have an inverse spin-Hall effect where a spin-current is converted to a

charge-current with the same efficiency, θ_{SH} .^{59,103} The expression for the charge-current generated is

$$\mathbf{J}_C = \frac{2e}{\hbar} \theta_{\text{SH}} \mathbf{J}_S \times \hat{\boldsymbol{\sigma}}. \quad (2.26)$$

A spin-current is typically pumped into a layer such as platinum by driving FMR in the magnetic layer with a cavity or waveguide.^{104–106} Because of its large spin-Hall angle, the platinum layer produces a voltage corresponding to the pumped current, which is proportional to the square of the cone angle of the magnetisation precession.

2.5 Current-induced spin-accumulation

In Chapter 2.4.2, it was shown that the spin-orbit coupling in a material could lead to the generation of spin-current from a charge-current (the spin-Hall effect). The spin-orbit coupling can, in particular materials, also create spin-accumulation from a charge-current. We will see later in Chapter 2.5.3 how the spin-accumulation can exert a torque on a local magnetisation.

The single-particle Hamiltonian, including the relativistic spin-orbit term, is given by

$$H = \frac{p^2}{2m} + V(\mathbf{r}) + \frac{\hbar}{4m^2c^2} [\nabla V(\mathbf{r}) \times \mathbf{p}] \cdot \boldsymbol{\sigma}, \quad (2.27)$$

where V is the electric potential and $\boldsymbol{\sigma}$ is the Pauli spin operator. If the charge carriers are holes, then $\boldsymbol{\sigma}$ should be replaced by the total angular momentum \mathbf{J} .³¹

The form of the eigenenergies can be found from symmetry arguments.¹⁰⁷ Without the symmetry-breaking application of a magnetic field, the Hamiltonian is invariant under time reversal, implying that $E(\mathbf{k}, \uparrow) = E(-\mathbf{k}, \downarrow)$ (Kramer's degeneracy). If the electric potential is inversion-symmetric, then $E(\mathbf{k}, \uparrow) = E(-\mathbf{k}, \uparrow)$ as only the sign of \mathbf{k} is reversed. Hence $E(\mathbf{k}, \uparrow) = E(\mathbf{k}, \downarrow)$, and therefore the spin bands can only be split in energy if there is inversion-asymmetry.

For structures with an inversion-asymmetry, the spin-orbit term in the Hamiltonian causes a spin-splitting in energy levels if $\mathbf{k} \neq 0$. The splitting can be described as $\frac{1}{2} \hbar \boldsymbol{\Omega}(\mathbf{k}) \cdot \boldsymbol{\sigma}$ ¹⁰⁷ where $\boldsymbol{\Omega}(\mathbf{k})$ is the precession vector describing the direction and magnitude of the spin-splitting. $\boldsymbol{\Omega}(\mathbf{k})$ can be viewed as an effective internal magnetic field, odd in \mathbf{k} because of Kramer's degeneracy. The spin-splitting leads to

a spin-texture on the Fermi surface, so that for a given \mathbf{k} , there is a majority spin population.

The inversion-asymmetry can take two forms; a bulk inversion-asymmetry (BIA) originating from the crystal structure, or a structural inversion-asymmetry (SIA) from a deformation or asymmetric electric potential. Two important forms of inversion-asymmetry will now be considered.

2.5.1 Dresselhaus spin-orbit interaction

Dresselhaus showed²⁵ that for a zinc-blende structure there exists a bulk inversion-asymmetry which results in a spin-orbit coupling with \mathbf{k}^3 dependence and form

$$\boldsymbol{\Omega}_D(\mathbf{k}) \cdot \boldsymbol{\sigma} \propto k_x(k_y^2 - k_z^2)\sigma_x + k_y(k_z^2 - k_x^2)\sigma_y + k_z(k_x^2 - k_y^2)\sigma_z. \quad (2.28)$$

If a strain exists in the lattice, the Hamiltonian is modified so that the effective field is linear in \mathbf{k} ^{108,109}

$$\boldsymbol{\Omega}_D(\mathbf{k}) \cdot \boldsymbol{\sigma} \propto k_x(\epsilon_{yy} - \epsilon_{zz})\sigma_x + k_y(\epsilon_{zz} - \epsilon_{xx})\sigma_y + k_z(\epsilon_{xx} - \epsilon_{yy})\sigma_z. \quad (2.29)$$

This result is important because it shows that a bulk material can naturally possess a spin-texture in momentum space.

2.5.2 Rashba spin-orbit interaction

Aside from the Dresselhaus spin-orbit interaction, if there is a deformation or an asymmetric electric potential, another symmetry of the spin-orbit interaction due to the SIA can exist,²⁸

$$\boldsymbol{\Omega}_R(\mathbf{k}) \cdot \boldsymbol{\sigma} \propto (\mathbf{k} \times \hat{\mathbf{z}}) \cdot \boldsymbol{\sigma}, \quad (2.30)$$

where $\hat{\mathbf{z}}$ is the symmetry-breaking axis. This is known as the Rashba symmetry. Observations of current-induced torques in ultra-thin ferromagnet/heavy metal bilayers have been attributed to a Rashba field induced by an electric field at the interface. One can immediately see how the Rashba symmetry falls out of equation 2.27 when the electric field is parallel to $\hat{\mathbf{z}}$.

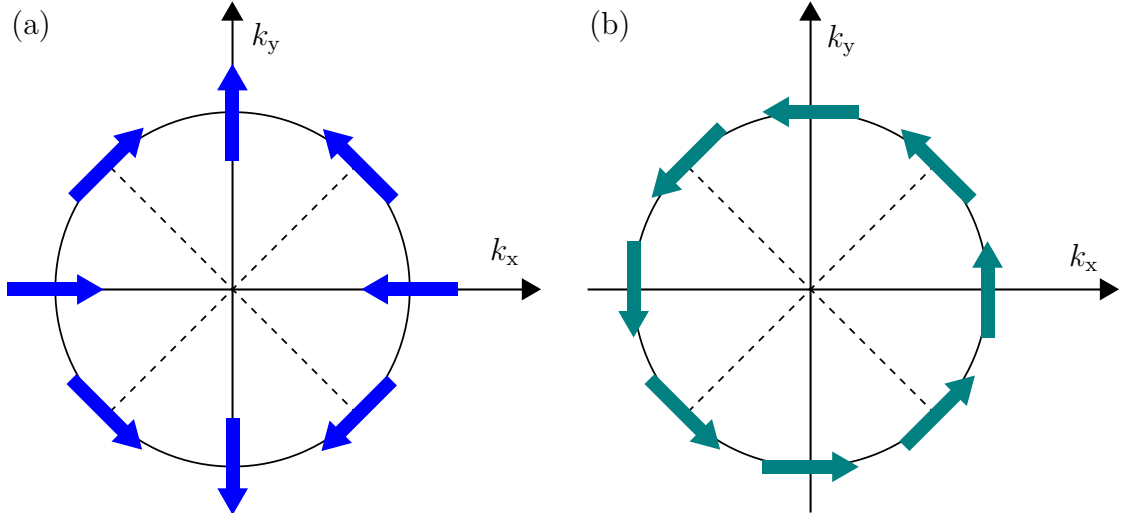


Figure 2.5: (a) The direction of the Dresselhaus symmetry fields for a given current direction. (b) The direction of the Rashba symmetry fields for a given current direction.

When a deformation exists in a zinc-blende structure, the off-diagonal elements of the strain tensor can also produce an effective field with Rashba symmetry¹⁰⁸

$$\boldsymbol{\Omega}_R(\mathbf{k}) \cdot \boldsymbol{\sigma} \propto (\epsilon_{zx}k_z - \epsilon_{xy}k_y)\sigma_x + (\epsilon_{xy}k_x - \epsilon_{yz}k_z)\sigma_y + (\epsilon_{yz}k_y - \epsilon_{zx}k_x)\sigma_z. \quad (2.31)$$

In thin films with zinc-blende crystal structures, the spin-orbit fields are in-plane as $\epsilon_{zz} \neq \epsilon_{xx} = \epsilon_{yy}$, and $\epsilon_{xy} = \epsilon_{yx}$ are the only non-zero off-diagonal elements of the strain tensor. The fields with the Dresselhaus and Rashba symmetries are shown in Figure 2.5.

2.5.3 Response to current

Now consider what happens when an electric field is applied. The whole Fermi surface is shifted in momentum space in response to the electric field. Certain \mathbf{k} states are depopulated as the opposite states are populated. Because of the spin-texture of the Fermi surface arising from the combination of spin-orbit interaction and inversion-asymmetry, the result is a net spin-accumulation, $\delta\mathbf{S}$. This is known as the inverse spin-galvanic effect,¹¹⁰ or Edelstein effect.³⁰

If a magnetisation is present in the material, the spin-accumulation exerts a

torque on it.³¹ In the first instance, because of the exchange coupling between the spin-accumulation and magnetisation, $F_{\text{ex}} = -J_{\text{ex}}\mathbf{M} \cdot \delta\mathbf{S}$, the effect of the spin-accumulation is to change the equilibrium position of the magnetisation by the effective exchange field, $H_{\text{ex}} = J_{\text{ex}}\delta\mathbf{S}$.^{111,112}

This picture is incomplete however because, between scattering events, as the charge-carriers are accelerated under the action of the applied electric field, the spins are still in their original polarisation. During acceleration, the spins begin to precess around the combination of the spin-orbit field and magnetisation. This leads to the field-like torque, as already discussed, but also to an anti-damping torque as some of the angular momentum of the spins' precession is transferred to the magnetisation.^{49,113,114} It is interesting to note that this is very similar to the origin of the intrinsic spin-Hall effect in a non-magnetic material, where the spin precession around the spin-orbit field leads to a pure spin-current.⁸⁹

2.6 Ferromagnets with inversion-asymmetry

To date, the study of ferromagnets with inversion-asymmetry has been very limited. Dilute magnetic semiconductors have been studied for their BIA, and ultra-thin metallic bilayers have been studied for their SIA. Below is a summary of both of these systems.

2.6.1 Dilute magnetic semiconductors

Dilute Magnetic Semiconductors (DMS) are a potential candidate for spintronic devices because of their integration of magnetism into semiconductors. Of these, the most widely studied class are the group IV-doped (III,V) compounds, with (Ga,Mn)As showing the most promise. These ferromagnetic materials have a Curie temperature (T_c) well below room temperature, and raising this is the focus of much research.¹¹⁵ However, for generating a strong spin-orbit torque, other DMS may be more effective.

$\text{Ga}_{1-x}\text{Mn}_x\text{As}$ is grown by low-temperature molecular-beam-epitaxy (LT-MBE) as the solubility of Mn ions in GaAs is low. By growing the material at a low temperature, the crystal structure can be kept far from thermodynamic equilibrium,

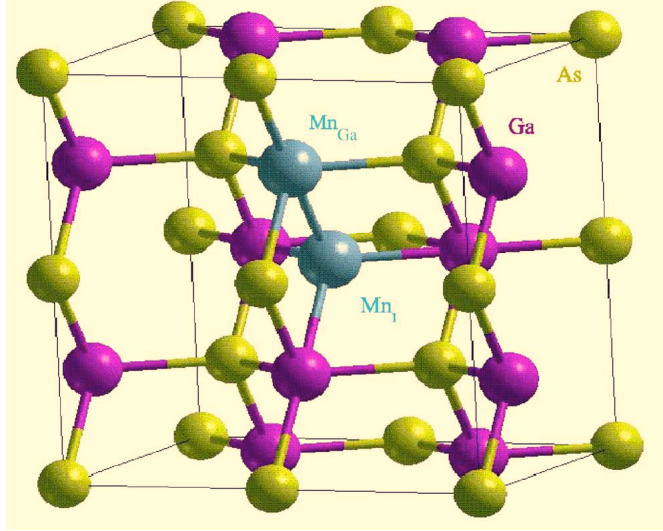


Figure 2.6: Crystal structure of (Ga,Mn)As, from Jungwirth et al.¹¹⁷ showing the substitutional (Mn_{Ga}) and interstitial (Mn_I) positions of the Mn ions within the GaAs lattice.

and concentrations of Mn up to $x \sim 10\%$ can be achieved.¹¹⁶ The MBE technique allows atomic layer-by-layer growth, resulting in good crystal quality.

The crystal structure of the material, determined by X-ray diffraction, is zincblende, similar to that of its host lattice, GaAs.¹¹⁷ The lattice mismatch between the (Ga,Mn)As and GaAs substrate leads to a compressive strain in the plane of the material. The resulting k-linear Dresselhaus spin-orbit fields (see Chapter 2.5.1) have been observed with dc switching³¹ and high-frequency FMR measurements⁴⁵.

Most of the Mn ions sit substitutionally on Ga sites, but there also exist some interstitial ions (see Figure 2.6) due to the non-equilibrium growth. The substitutional Mn ions have a spin $S = \frac{5}{2}$ and act as acceptors, creating itinerant holes which mediate the ferromagnetism of the Mn ions.¹¹⁸ However, the interstitial Mn ions act as double donors as they do not sit on a lattice site. This compensates the hole concentration and reduces the Curie temperature which is predicted by the Zener model to be roughly proportional to $p^{\frac{1}{3}}$.¹¹⁹

Low temperature annealing has been shown to significantly increase T_c .¹¹⁵ This has been explained by the out-diffusion of the interstitial Mn ions to the surface of the material, removing the hole-compensating defects.¹²⁰

To increase the spin-orbit fields, heavier ions in the lattice could be used,

introducing larger lattice electric potentials. (Ga,Mn)Sb substitutes the Arsenide ions for Antimony, increasing the spin-orbit energy splitting by ~ 2.5 times.¹²¹ (Ga,Mn)Sb has been grown by MBE on GaSb and hybrid GaAs/ZnTe substrates giving magnetic easy axes in and perpendicular to the plane respectively.¹²²

Although the prospects for room temperature DMS are currently not very promising, there has been recent interest in (I-Mn-V) dilute magnetic semiconductors, due to predictions of high-temperature antiferromagnetism and strong spin-orbit coupling.¹²³ In 2010 Novák et al. reported the first growth of LiMnAs by MBE with the expected crystal structure and showed that the optical properties were consistent with a semiconducting band structure.¹²⁴

Although these materials do not have a macroscopic magnetisation vector, methods have been proposed to couple antiferromagnets with high temperature ferromagnets for spintronic applications.^{125,126}

2.6.2 Metal bilayers

Ferromagnet/heavy metal bilayers have received much attention in recent studies because of the presence of large current-induced torques.^{23,39} These materials are easily grown by sputter deposition, and typically the ferromagnet has an additional oxide interface with the substrate or an oxidised aluminium layer. There is debate over whether the oxide interface plays a significant part in the current-induced torque mechanism, although it has been shown that the ferromagnet/heavy metal interface is sufficient for a current-induced torque to exist.⁴¹ By controlling the amount of oxidation at this interface, the perpendicular magnetic anisotropy of the ferromagnet can be controlled.¹²⁷

There are two complementary theories regarding the origin of the current-induced torques present in these layers. Firstly, the heavy metals used in the bilayers typically have a large spin-Hall effect. The spin-current generated can exert a spin-transfer torque on the magnetic layer²⁴ as discussed in Chapter 2.4.2. Secondly, there is a structural inversion-asymmetry at the interface between the ferromagnet and the heavy metal, and also at the interface between the ferromagnet and the oxide. The electric fields at these interfaces could lead to a transverse spin-orbit field (see Chapter 2.5.2), which could exert field-like and anti-damping torques on the ferromagnet.^{40,113,114}

The extent to which each of these mechanisms gives rise to the observed current-induced torques in ultra-thin bilayers is still disputed. Distinguishing the origins of the field-like and anti-damping torques requires study of their dependence on the thickness of the heavy metal and ferromagnet layers. Recently, thickness-dependent low-frequency measurements of the torques have been made in Ta/CoFeB/MgO layers³³ and in Py/Pt layers with Cu spacer layers³⁵. Although both studies clearly show that the thickness-dependence of the torques cannot be solely explained by either a spin-Hall effect STT or Rashba effective fields, further study is required to understand behaviour in the ultra-thin regime.

Chapter 3

Experimental methods

In this chapter, the main experimental techniques used in this thesis are presented. These include spin-orbit FMR, which is used in studies of Co/Pt and Fe/(Ga,Mn)As in Chapters 5 and 6 respectively. The electromagnet system constructed to measure these materials is also discussed, as well as the techniques used to fabricate the measured devices.

3.1 Spin-orbit FMR

In comparison to conventional FMR, spin-orbit FMR (SO-FMR) uses the current-induced torques due to the interaction between non-equilibrium spin density and magnetisation to drive FMR. Instead of using a microwave cavity or a waveguide to induce microwave fields over the sample area, a microwave current in the sample generates an alternating effective field via the spin-orbit interaction. Fang *et al.*⁴⁵ demonstrated this technique in bulk (Ga,Mn)As, where the fields observed were attributed to the exchange interaction between the current-induced spin-accumulation and the local Mn ions. Liu *et al.*²³ presented a similar experiment in Py/Pt bilayers in which the origin of the effective field was attributed to a spin-transfer torque in the Py layer. The current in the platinum layer generated a spin-current via the spin-Hall effect which, when entering the permalloy layer, would create an effective field with anti-damping symmetry.

An intrinsic method of detection is required in SO-FMR, since the driving fields are created intrinsically. SO-FMR is measured by using a dc self-rectification

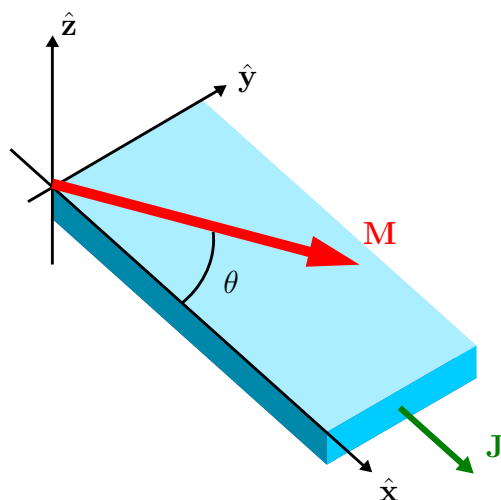


Figure 3.1: The co-ordinate system is defined such that the current is always along \hat{x} , and \hat{z} is always perpendicular to the plane. θ is defined as the angular separation of the magnetisation and current.

detection method previously used with microwave waveguides for FMR in sub-micron devices.¹²⁸ The effect exploits the AMR of the sample, which causes the sample resistance to oscillate during precession. Ignoring smaller crystal terms which may be present, the AMR can be parametrised as¹²⁹

$$R = R_0 + \Delta R \cos^2 \theta. \quad (3.1)$$

θ is defined in Fig. 3.1 as the in-plane separation of the current and magnetisation. Note that for metals, ΔR is typically positive, whereas for magnetic semiconductors such as (Ga,Mn)As, ΔR is negative. For a driving current of $I = I_0 \cos(\omega t)$, θ varies periodically with the magnetisation precession,

$$\theta(t) = \theta_0 + \theta_c \cos(\omega t), \quad (3.2)$$

where θ_c is the cone angle of the magnetisation precession. Using Ohm's law, and expanding $\cos^2 \theta$ to first order in θ_c , for small angle precession

$$R = R_0 + \Delta R [\cos^2 \theta_0 - \theta_c \sin(2\theta_0) \cos(\omega t)]. \quad (3.3)$$

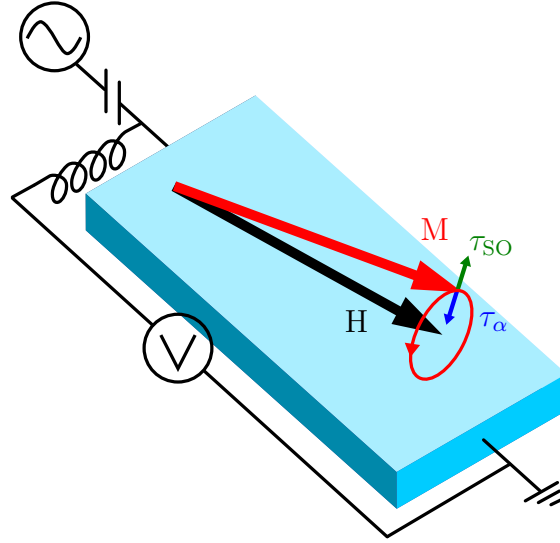


Figure 3.2: A schematic of a typical SO-FMR experiment. A bias-tee component, consisting of an inductor and capacitor, is used to separate the flow of microwave and dc currents. The microwave current flowing in the micro-bar, through spin-orbit effects, creates an alternating torque on the magnetisation, τ_{SO} , which balances the damping torque, τ_{α} , causing the magnetisation, M , to precess around the external field, H . Through a magnetoresistance rectification effect, the resonance can be measured in the dc voltage across the bar.

This produces a dc voltage given by

$$V_{\text{dc}} = -\frac{1}{2}\theta_c I_0 \Delta R \sin(2\theta). \quad (3.4)$$

In this case the sample is acting as a homodyne mixer, down-converting the GHz oscillation in the resistance to give a dc voltage which is proportional to the size of the oscillation.

The LLG equation (equation 2.10) can now be solved by assuming the saturated magnetisation is perturbed by a small effective magnetic field, $\mathbf{h} = (h_x, h_y, h_z)e^{i\omega t}$. The real part of the dc voltage, V_{dc} , is given by symmetric and antisymmetric Lorentzian parts^{45,130}

$$\Re\{V_{\text{dc}}\} = V_{\text{sym}} \frac{\Delta H^2}{(H - H_{\text{res}})^2 + \Delta H^2} + V_{\text{asy}} \frac{\Delta H(H - H_{\text{res}})}{(H - H_{\text{res}})^2 + \Delta H^2}, \quad (3.5)$$

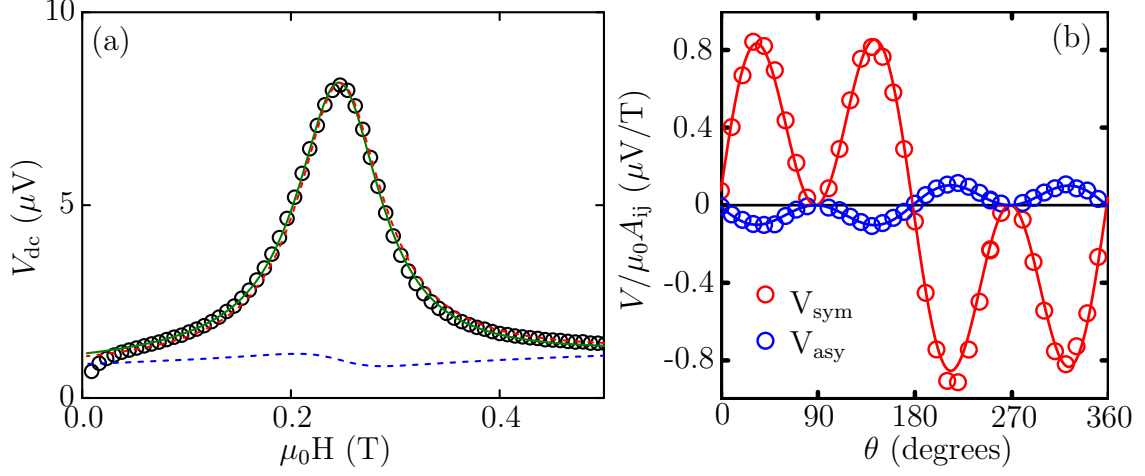


Figure 3.3: (a) A typical FMR curve measured in V_{dc} as a function of external field fitted by symmetric (red) and antisymmetric (blue) Lorentzians (data taken from a Co(1.5 nm)/Pt(3 nm) bilayer device as measured in Chpt. 5). (b) Shown also is the fitted angle dependence of the Lorentzian coefficients, normalised by the ac susceptibility. The angle dependence of the symmetric part is fitted by an anti-damping torque ($h_z \propto \cos\theta$) and the antisymmetric part is fitted by a field-like torque (constant h_y).

with

$$V_{\text{sym}} = V_{\text{mix}} A_{yz} \sin(2\theta) h_z, \quad (3.6)$$

and

$$V_{\text{asy}} = V_{\text{mix}} A_{yy} \sin(2\theta) (h_y \cos\theta - h_x \sin\theta). \quad (3.7)$$

$V_{\text{mix}} = -\frac{1}{2} I_0 \Delta R$ is the size of the mixing effect; $\Delta H = \frac{\alpha\omega}{\gamma}$ is the linewidth of the resonance; and A_{yz} and A_{yy} are related to the tensor elements of the ac magnetic susceptibility by $A_{ij} = \chi_{ij}/M_S$:¹³¹

$$A_{yz} = \frac{\gamma(H_{\text{res}} + H_1)(H_{\text{res}} + H_2)}{\omega\Delta H(2H_{\text{res}} + H_1 + H_2)}, \quad (3.8)$$

and

$$A_{yy} = \frac{H_{\text{res}} + H_1}{\Delta H(2H_{\text{res}} + H_1 + H_2)}. \quad (3.9)$$

H_1 and H_2 are terms containing the anisotropy fields derived in Kittel's equation (equation 2.14). A typical SO-FMR measurement at a single θ value of θ is shown in Fig. 3.3a and the corresponding fitted angle dependence of V_{sym} and V_{asy} is shown

in Fig. 3.3b.

Experimentally, to measure V_{dc} , a bias-tee component is used to separate the flow of alternating and direct current. A schematic of a SO-FMR measurement using the bias-tee is shown in Fig. 3.2. The bias-tee is a three-port device consisting of a capacitor and inductor. The capacitor only allows the flow of high frequencies, whilst the inductor only allows the flow of low frequencies. The microwave signal is sent through the capacitor port of the bias-tee, through the sample to ground. V_{dc} can then be measured from the inductor port to ground.

SO-FMR is a useful tool to study FMR in sub-micron devices. Whilst the electrical detection method had previously allowed resonance to be measured in non-bulk samples, a co-planar strip waveguide was needed to provide an external microwave field.¹²⁸ Now that the fields can be induced intrinsically via the spin-orbit interaction, the samples can be fabricated as simple resistors. Furthermore, SO-FMR allows the full form of the spin-orbit fields (h_x, h_y, h_z) to be studied by vector magnetometry by measuring the angular dependence of V_{dc} .⁴⁵

3.2 Electromagnet system

Whilst a superconducting magnet can produce high magnetic flux densities (due to the high amount of current that can be held in the coils), the cost of keeping the magnet cold can be prohibitive. For room temperature measurements an alternative approach is to use a large electromagnet with small pole faces and pole gap.

For the purpose of making room temperature SO-FMR measurements, a GMW Model 5403 variable pole gap electromagnet was used. The magnet poles have a diameter of 38 mm, which, with a pole spacing of 30 mm and coil current of ~ 40 A (water cooled), can produce a magnetic field in the air gap of ~ 1 T. This is sufficient for most FMR measurements, although the pole spacing restricts the amount of equipment that can be placed between the poles.

The electromagnet system can be seen in Figure 3.4. A probe is suspended from a rotation stage by four screws, which itself is mounted on two micrometre precision translation stages which allow the sample to be positioned centrally between the poles. This positioning is important, because for a 6 mm deviation off-axis, the field is reduced by 1%. Microwave and dc connections to the probe are made from

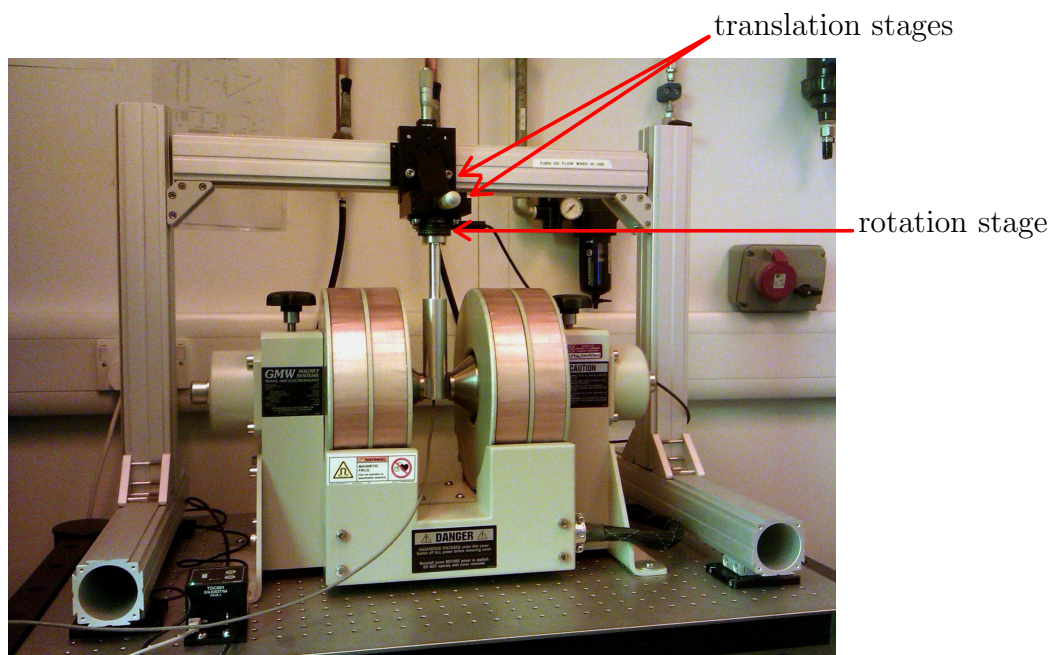


Figure 3.4: Electromagnet apparatus. The magnet and frame are bolted to an optical bench. The frame supports two translation stages and a rotation stage which allow a probe, bolted to the rotation stage, to be rotated through 360° and positioned in the centre of the magnetic field. The electromagnet is water-cooled to allow 40 A to constantly flow through the coils. Adjustable poles allow the pole gap to be varied.

underneath. A right-angled SMP connector is used to connect a semi-rigid coaxial cable to the probe without preventing rotation.

3.2.1 Field calibration

To calibrate the field produced by the electromagnet, first a Hall sensor was calibrated using a gaussmeter. The uncalibrated Hall sensor has a quoted linearity of $\sim 1\%$ and a sensitivity of $1 \text{ k}\Omega\text{T}^{-1}$. The gaussmeter has a quoted error of 1% . The uncalibrated Hall sensor and gaussmeter sensor were strapped together, both sharing the same sensitive axis. The whole ensemble was then attached to a single magnet pole face, so that they shared a common field. For a series of magnet currents, the magnetic field, B , experienced by the gaussmeter, and the Hall resistance induced R_{Hall} , were recorded.

A linear regression, shown in Figure 3.5, was then performed to determine the

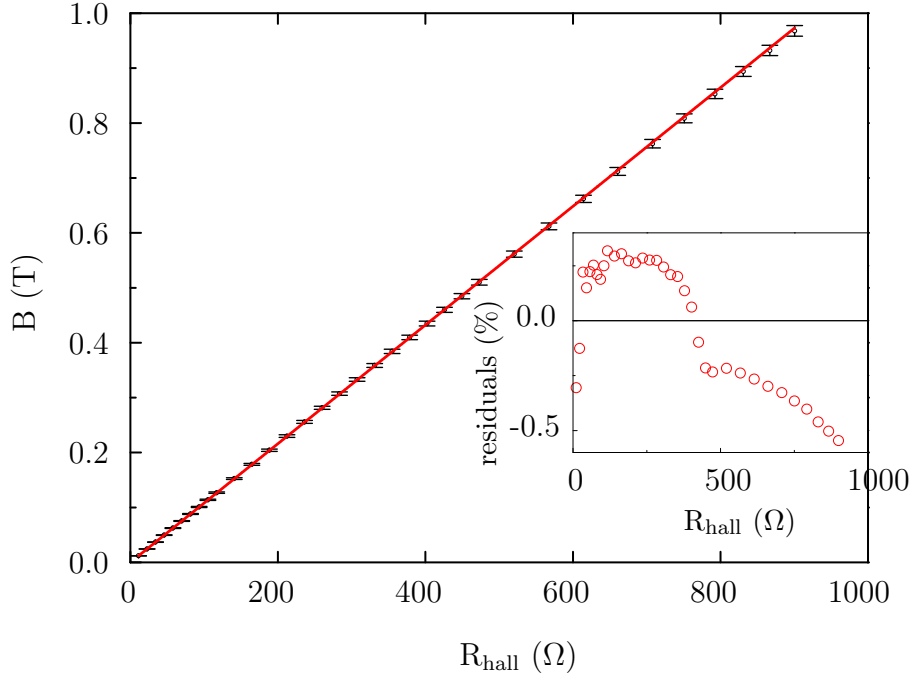


Figure 3.5: Calibration of Hall sensor using a gaussmeter. 1% error bars on the data points represent the systematic error from the gaussmeter. The linear regression is also plotted. Inset: The residuals of the linear regression, showing systematic deviations. The linearity of the sensor is good to within 0.5% in the field range measured.

relationship between B and R_{Hall} . The error in the gaussmeter should strictly be treated as a systematic error, but for the purposes of weighting the regression, the error was treated as a measurement (random) error.

The linearity of the Hall sensor is found to be $\sim 0.5\%$ for the resistance range used. This can be seen from the residuals of the fit in the inset of Figure 3.5. Note that the systematic residuals between the regression and data dominate any random error.

Next, the Hall sensor was mounted in a vertical probe designed such that the sensor is positioned on the radial axis of the probe. The translation stages were used to position the Hall sensor in the centre of the field by maximising the Hall resistance. The sensitive axis of the Hall probe was then aligned with the field by rotating the probe until the Hall resistance was maximised. For a series of pole spacings, the magnet current was ramped from 40 A to -40 A whilst R_{Hall} was

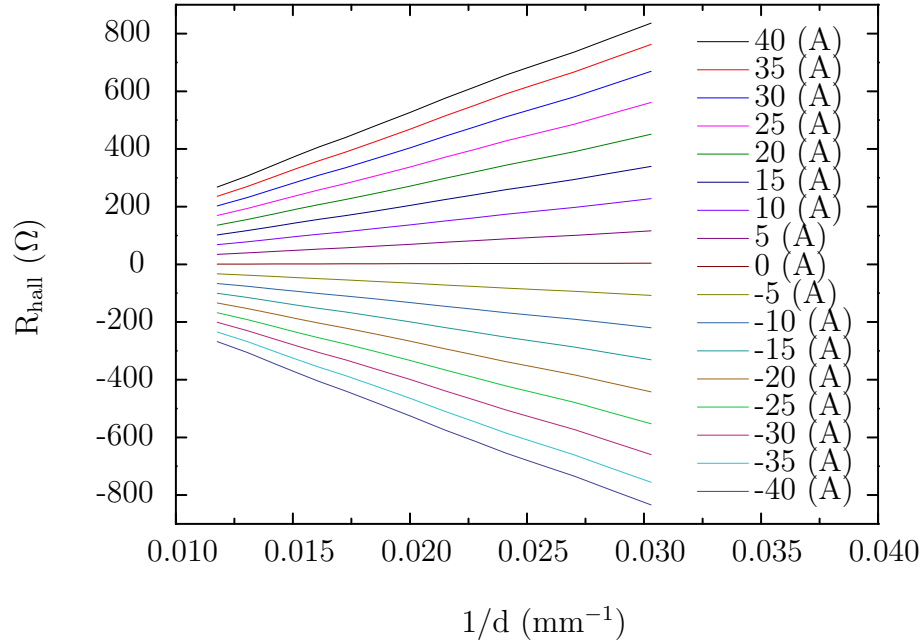


Figure 3.6: The hall resistance, shown here for a constant current, is measured and is proportional to the inverse of the pole gap in agreement with equation 3.12.

measured. The pole spacing was accurately measured with a divider and steel rule (estimated $\sigma = 0.5$ mm).

The electromagnet can be thought of as an iron core toroid with a gap. To calculate the field in the gap one should consider the integral form of Ampère's law,

$$\oint d\mathbf{l} \cdot \mathbf{H} = \int_{\mathbf{s}} d\mathbf{s} \cdot \mathbf{J}. \quad (3.10)$$

If the gap is small, one can also assume that the magnetic flux density is confined to the core area across the gap. This leads to an expression relating the fields inside the core and in the gap,

$$H_{\text{gap}} = \mu H_{\text{core}}. \quad (3.11)$$

Because the permeability of soft iron is >1000 , it is a very good approximation to

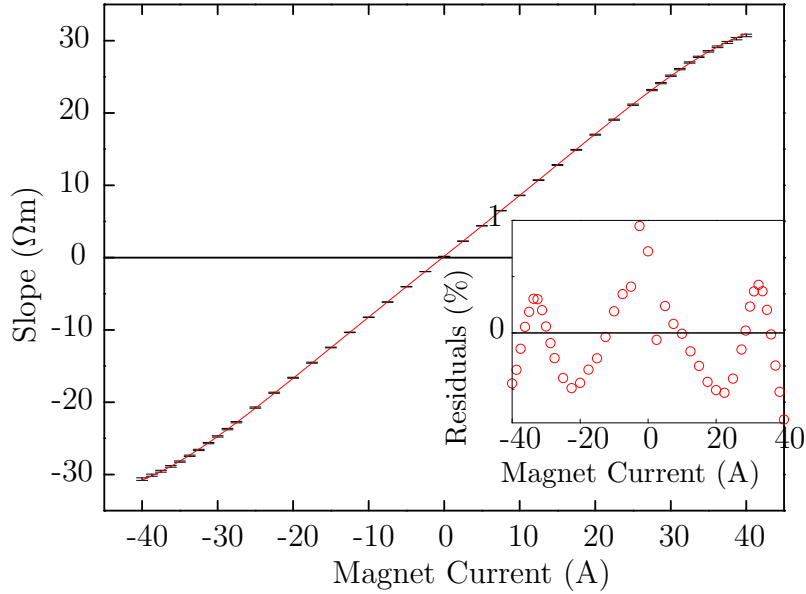


Figure 3.7: Slope of the fitted regressions for R_{Hall} versus d_{gap} as shown in Figure 3.6 as a function of magnet current, fitted with a polynomial. The sublinearity at high current shows that the soft iron core is becoming saturated. Inset: The residuals show a systematic difference between the measured data and the polynomial fit no greater than 0.5%.

assume all of the magnetic field is in the gap. Hence we can express the field as

$$H_{\text{gap}} = \frac{I_{\text{enc}}}{d_{\text{gap}}}, \quad (3.12)$$

where d_{gap} is the pole separation.

For a series of currents, the measured Hall resistance is plotted against $1/d_{\text{gap}}$. The plotted data show excellent linearity in agreement with equation 3.12, as can be seen in Figure 3.6. For each value of $1/d_{\text{gap}}$, a linear regression is performed to extract the slope and intercept, each with a standard error. The slope and intercept are then plotted as a function of the magnet current in Figure 3.7 and Figure 3.8 respectively.

The slope should be proportional to the current, according to equation 3.12, but at high currents this becomes sublinear. The reason for this is the saturation of the iron electromagnet poles. As a result μ is reduced at higher currents, and a smaller proportion of the magnetic field exists in the gap. As there is no analytical

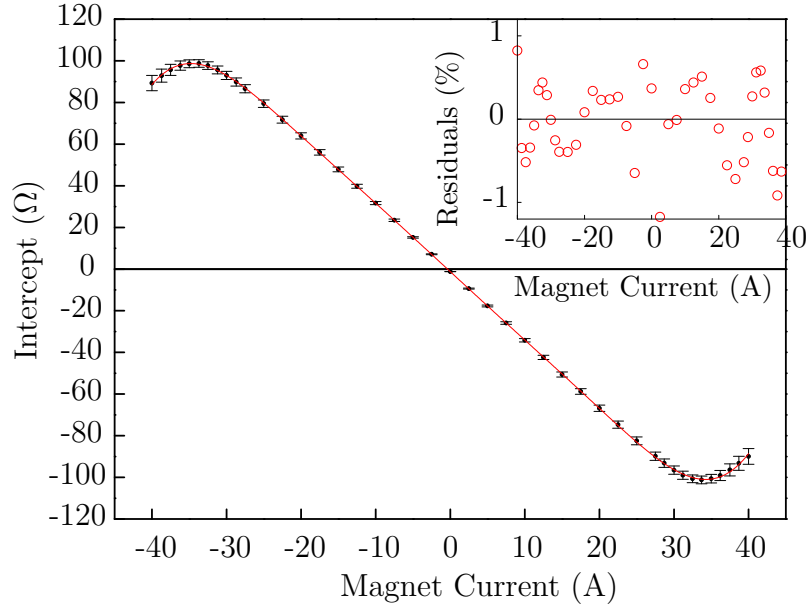


Figure 3.8: Intercept of the fitted regressions for R_{Hall} versus d_{gap} as shown in Figure 3.6 as a function of magnet current, fitted with a polynomial. Inset: The residuals show a systematic difference between the measured data and the polynomial fit no greater than 1%.

function that describes this behaviour, the slope and intercept curves are fitted by a 5th and 9th order polynomial respectively. The standard error for each slope and intercept data point is used to weight the fit.

The distribution of errors for these fits can again be seen from the residuals in Figures 3.7 and 3.8. The residuals are dominated by systematic differences between the measured data and the polynomial fitting. When calculating R_{Hall} for a given magnet current and pole spacing, using the fitted functions for the slope and intercept, for the range of pole spacings that can be used the systematic errors from the slope dominate the total error ($\sigma < 0.5\%$).

For a given pole spacing and magnet current, the central field in the electromagnet gap can now be calculated as

$$B(d_{\text{gap}}, I_{\text{enc}}) = B_0 + B_1 \left(R_0(I_{\text{enc}}) + R_1(I_{\text{enc}}) \frac{1}{d_{\text{gap}}} \right), \quad (3.13)$$

where B_0 and $B_1(R)$ are the fitted intercept and gradient of Figure 3.5, and $R_0(I_{\text{enc}})$ and $R_1(I_{\text{enc}})$ are the polynomial fits of the intercept (Figure 3.8) and gradient

(Figure 3.7) respectively for the relationship between R_{Hall} and $1/d_{\text{gap}}$.

Care has to be taken when estimating the error in the calculated field, because the errors are systematic and correlated, and therefore do not obey the central limit theorem. In the measurements shown here, the systematic error in B_1 is estimated as $\delta B_1/B_1 < 0.5\%$, and in the Hall resistance as $\delta R_{\text{Hall}}/R_{\text{Hall}} < 0.5\%$. An additional error of 1% should be included in B_1 due to the systematic error in the gaussmeter. These errors should be treated as perfectly correlated, because they do not change if the measurements are repeated. The total error is then described by

$$\begin{aligned} \delta B^2 &= \left(\delta B_1 \frac{\partial B}{\partial B_1} + \delta R_{\text{Hall}} \frac{\partial B}{\partial R_{\text{Hall}}} \right)^2 \\ &= \left(\delta B_1 \frac{R}{B_0 + B_1 R_{\text{Hall}}} + \delta R_{\text{Hall}} \frac{B_1}{B_0 + B_1 R_{\text{Hall}}} \right)^2 \\ &\approx \left(\frac{\delta B_1}{B_1} + \frac{\delta R_{\text{Hall}}}{R_{\text{Hall}}} \right)^2 B^2, \end{aligned} \quad (3.14)$$

where it has been assumed that $B_0 \ll B_1 R_{\text{Hall}}$. This gives a total error in the calibrated field of $< 2\%$. In the low current limit when this assumption breaks down, the error can be found from the residual as $R_{\text{Hall}} \rightarrow 0$, which gives $\delta B \sim 40 \mu\text{T}$. At low fields, the random error in the slope and intercept value (as shown in the error bars of Figures 3.7 and 3.8) is also significant, giving a total error (adding in quadrature) of $\delta B \sim 80 \mu\text{T}$.

Finally, one must consider the effect of the uncertainty in the pole spacing on the uncertainty in the magnetic field. For a single set of measurements, a single pole spacing will be set, and this has an estimated uncertainty of $\sigma = 0.5\%$. This leads to systematic over- or under-estimation of the magnetic field value, with a standard deviation given by,

$$\delta B \approx B_1 R_1 \delta d_{\text{gap}} \frac{\partial}{\partial d_{\text{gap}}} \left(\frac{1}{d_{\text{gap}}} \right), \quad (3.15)$$

which simplifies to,

$$\frac{\delta B}{B} \approx \frac{\delta d_{\text{gap}}}{d_{\text{gap}}}. \quad (3.16)$$

For the smallest pole spacing that can be used with the FMR probes, 30 mm,

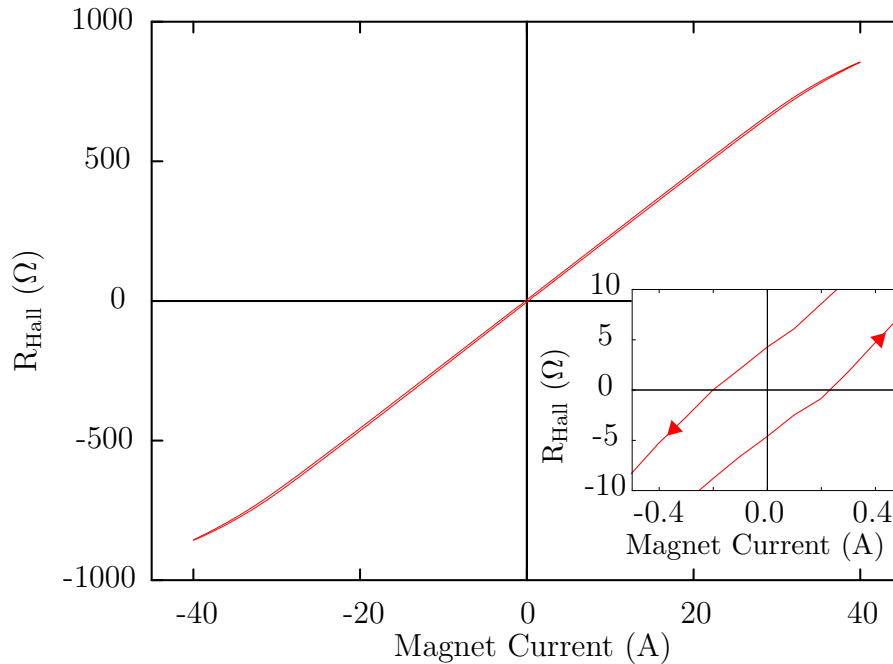


Figure 3.9: The soft iron core performs well as an electromagnet because it has low hysteresis and high saturation magnetisation. Inset: A close up of the same curve showing the hysteresis around zero current. The magnet has a coercive field of 0.1 mT and a remnant magnetisation corresponding to a magnetic field of 4 mT.

this gives a maximum uncertainty of $\sigma = 1.7\%$ in the field value. Although this error is systematic, it is a different class of systematic error from those previously considered because it arises from *random* uncertainty in the pole spacing. Thus the error is completely uncorrelated from other systematic errors and obeys the central limit theorem. To obtain a final uncertainty in the magnetic field calibration, this error can be added in quadrature with the other systematic errors, yielding a value of 2.6%.

3.2.2 Hysteresis

When making a real measurement, the hysteresis of the magnet should be a concern. During the calibration, the magnet was consistently ramped from positive to negative field, but in an experiment, this might not be true unless a strict pro-

tolcol is adhered to. To measure the hysteresis of the magnet, for a pole spacing of 33 mm, R_{Hall} was measured as the current was initially ramped to 40 A and then the cycled between -40 A and 40 A. The resulting main loop is plotted in Figure 3.9, and shows a coercive field of 0.1 mT. The remnant magnetisation corresponds to a magnetic field of 4 mT. Since the magnet has been calibrated for the top half of the main loop, for a given magnet current, the maximum deviation possible would be -8 mT.

3.3 Clean room fabrication

In nano-scale device fabrication, care has to be taken to keep the surfaces of the material free of dirt and impurities. To this extent, all fabrication is carried out in a clean room. Before each processing step, the wafers are cleaned in acetone in an ultrasound bath for two minutes before rinsing in isopropanol (IPA) and drying with N_2 gas.

There are two main steps in the fabrication of nano-bars and waveguides for SO-FMR experiments: patterning and etching of the trenches, and then patterning and evaporation of the bond pads and waveguides. Each process is described below.

3.3.1 Electron-beam lithography

To etch device trenches, or to evaporate bond pads, a patterned layer (a resist) of poly(methyl methacrylate) (PMMA) is used. Samples, preheated for one minute at 120°C on a hot-plate, are spin-coated for 30 seconds at 5000 rpm with a layer of PMMA in anisole. The sample is then baked at 120°C for an hour to drive off the excess solvent, curing the resist, before patterning by electron-beam lithography (EBL).

Patterns designed by computer-aided design software are written by EBL onto the PMMA*. The energy imparted into the PMMA by the incident electrons chemically weakens the exposed areas, allowing a developer to dissolve them away. The

*The EBL patterning for the Co/Pt samples was kindly carried out by Andrew Irvine and Dominik Heiss of the University of Cambridge. The entire fabrication of the Fe/(Ga,Mn)As bars was kindly performed by Kamil Olejník of the Institute of Physics, Prague.

samples were developed by immersing the sample in a ratio of 1:3 MIBK:IPA for 60s. MIBK is the organic compound methyl isobutyl ketone.

Using a different molecular weight of PMMA in anisole allows the thickness of the final layer to be controlled. For most lithography, a 6% solution (A6) is used, which results in a ~ 400 nm thick layer.

3.3.2 Ion-beam milling

Device trenches are dry-etched by bombardment with high-energy Ar ions, which are accelerated onto the substrate by a 500 V bias in a high vacuum system. Each Ar ion might typically have ~ 500 eV of energy. A beam current of 10 mA will etch metals at a rate of ~ 5 nm per minute, whilst for GaAs based semiconductors the rate can be much faster. Trenches are created in order to define the device geometry and to isolate the device from the rest of the wafer.

Because of the energy of the ions, the etch is very anisotropic, preventing undercutting of the trenches. The samples are etched until all of the exposed conducting material is removed. After etching, the resist is removed by immersion in acetone.

3.3.3 Bond pad evaporation

To make electrical contact with the devices, bond pads are needed. The pads must have good ohmic contact with the device to allow easy measurement. Prior to evaporation, metal sources are ‘flashed’ under high vacuum (below 10^{-7} mbar) to remove impurities. This involves heating the source with an electrical current to above the temperature needed for the source to evaporate. Prior to evaporation, organic material is removed from the surface of the sample by 30 seconds exposure in an oxygen plasma asher.

The sample is mounted in the vacuum chamber on a movable arm to allow positioning over different evaporation sources. A thin layer of chromium (typically 20 nm), and then gold (usually 100-200 nm) is deposited by evaporation under high vacuum at rates of 0.4 and 2 \AA s^{-1} respectively. The chromium is needed to allow good adhesion of the gold to the surface. The resist is then removed by ‘lift-off’ in acetone, leaving the patterned pads behind on the wafer. A short burst of ultrasound in a water bath can be used to assist the process.

3.3.4 Sample mounting

Once fabricated, a protective PMMA resist is spun onto the wafers. They are then scribed into pieces, each containing a device, with a diamond tip before cleaving over a sharp edge. The protective resist is then removed by immersion in acetone. A device is then glued to a PCB with insulating GE varnish, designed for good adhesion at very low temperatures. However, it also works equally well at room temperature. Finally, a wire-bonder machine is used to bond aluminium or gold wire between the PCB terminals and the device bond pads.

Chapter 4

Spin-pumping in Co/Pt bilayers

The detection of spin-currents is of fundamental importance to the development of spintronic devices. There has been much research investigating ferromagnetic/normal metal bilayers, where a pure spin-current generated from ferromagnetic resonance (FMR) in the ferromagnetic layer is converted to a charge current by the inverse spin-Hall effect (ISHE) in the nonmagnetic layer.^{54–57} When measuring nanoscale devices, an on-chip waveguide is typically used to provide the driving field for FMR. This complicates the detection as microwave current coupled into the device provides an additional rectification signal.¹⁰⁶ Some attempts have been made to distinguish the two signals.^{106,132–136}

In this chapter, in contrast to previous research on thicker layers,^{132,137} spin-pumping is investigated in ultra-thin Co/Pt bilayers in which the interface region is a significant proportion of the bulk ferromagnet and platinum layers. By keeping the platinum layer thickness constant, any variation in the bulk inverse spin-Hall detection is eliminated. The strength of the spin-pumping voltage in the platinum layer is examined as the thickness of the ferromagnet is varied.

4.1 Device fabrication

In this study the samples are thin bars of Co/Pt with nominal cobalt thickness $d_{\text{Co}} = 1, 1.25, 1.5, 1.75$ and 2 nm capped with a 3 nm platinum layer. From X-ray reflectivity (XRR) measurements* the uncertainty in the thickness of these

*XRR measurements were performed by Mu Wang of Nottingham University.

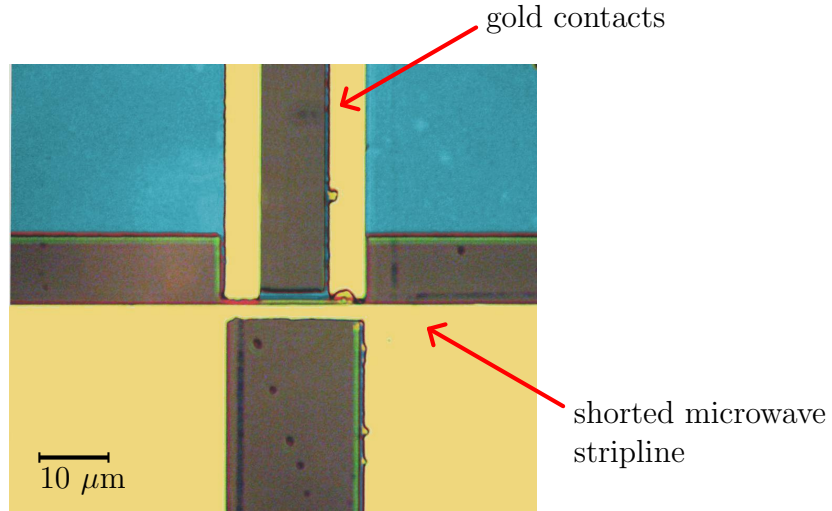


Figure 4.1: False colour optical micrograph of the fabricated device. The yellow areas are deposited gold contacts and a shorted microwave stripline. The blue areas are the remainder of the substrate after etching.

layers is estimated to be 10%. An out-of-plane microwave magnetic field ($h_z e^{i\omega t}$), to induce ferromagnetic resonance (FMR), was generated over the sample area by an on-chip coplanar stripline, shorted $1 \mu\text{m}$ away from the sample.

The devices were fabricated from films sputtered on thermally oxidised silicon.[†] Electron beam lithography was used for patterning,[‡] and then $1 \times 10 \mu\text{m}$ bars and adjacent striplines were defined with Ar ion-milling. The bars are contacted by 200 nm thick gold contacts which were deposited by evaporation at the same time as the gold striplines. An optical micrograph of the device is shown in Figure 4.1. A schematic of the device and measurement is shown in Figure 4.2.

4.2 Detection of resonance

The sample was mounted on a low loss printed circuit board (PCB) with a microstrip transmission line. A 15 GHz microwave signal was sent via a coaxial cable into the PCB microstrip. Wirebonds were used to connect the microstrip signal line to one side of the stripline and the other side of the shorted stripline to ground.

[†]Sputtering was performed by Mu Wang, Aidan Hindmarch and Andrew Rushforth of Nottingham University.

[‡]Electron beam lithography was performed by Andy Irvine and Dominik Heiss of the University of Cambridge.

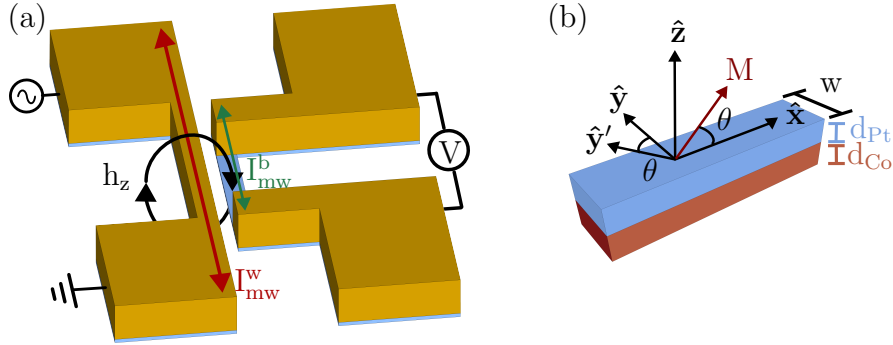


Figure 4.2: (a) Measurement schematic showing coplanar stripline on left with microwave current, I_{mw}^w , generating a perpendicular microwave field over the bar area. A microwave current, I_{mw}^b , is coupled into the bar. The voltage is measured across the bar contacts with a lock-in amplifier. (b) The bar consists of a platinum layer deposited on top of a cobalt layer. The in-plane angle θ is defined as the angle between the bar direction and the magnetisation.

No attempt was made to transform the unbalanced signal in the microstrip to a balanced signal in the stripline. The signal power in the coaxial cable directly before the PCB was directly measured by a calibrated microwave diode as 14.5 dBm. As the PCB waveguides and on-chip striplines are identical for each device, similar microwave currents, I_{mw}^w , are expected in every stripline. In this measurement it is assumed that the microwave field generated is similar for each sample.

The microwave signal was pulse modulated at a low frequency (23.45 Hz) allowing a lock-in amplifier to detect the dc voltage (V_{dc}) across the sample. The sample was positioned in a 3-axis vector magnet at a temperature of 250 K. Ideally the measurement would be made at room temperature, but the temperature of the sample takes a long time to stabilise at higher temperatures. For a particular direction, the external magnetic field was swept from high to low field, and the ferromagnetic resonance was observed as a combination of symmetric and antisymmetric Lorentzian peaks in V_{dc} .

V_{dc} is thought to be generated through two effects: the inverse spin-Hall effect (ISHE) and rectification. During steady-state precession, the driving torque is balanced by a damping torque. The platinum layer adjacent to the ferromagnet is an efficient spin-current sink and contributes to the damping by transferring angular momentum between the cobalt and platinum layers via a spin-current. The spin-current, J_s , injected into the platinum layer through the ISHE generates

a transverse charge current given by¹³⁷

$$\mathbf{J}_C = \theta_{\text{SH}} \left(\frac{2e}{\hbar} \right) \mathbf{J}_S \times \hat{\boldsymbol{\sigma}} \quad (4.1)$$

This yields a total charge current of I_c which creates a voltage $V_{\text{ISHE}} = I_c R$ across the bar. θ_{ISHE} , e , \hbar and σ represent the spin-Hall angle, the elementary charge, the reduced Planck constant and the spin polarisation vector of the spin-current respectively.

The microwave current in the shorted stripline can couple into the sample, to give another microwave current, I_{mw}^b . At resonance the magnetisation will precess at the same frequency as this current. Precession of the magnetisation causes an oscillating component to the resistance, due to the anisotropic magnetoresistance (AMR) $R = R_0 + \Delta R \cos^2 \theta$. This multiplies with the microwave current to give a measurable V_{dc} . Combining this with V_{ISHE} , the real part of the voltage is given by the sum of symmetric and antisymmetric parts^{130,133,137}

$$\begin{aligned} V_{\text{dc}} = & (V_{\text{AMR}} \cos \phi_{\text{coup}} + V_{\text{ISHE}}) \frac{\Delta H^2}{(H - H_{\text{res}})^2 + \Delta H^2} \\ & + V_{\text{AMR}} \sin \phi_{\text{coup}} \frac{\Delta H (H - H_{\text{res}})}{(H - H_{\text{res}})^2 + \Delta H^2} \end{aligned} \quad (4.2)$$

with V_{AMR} and V_{ISHE} given by

$$V_{\text{AMR}} = V_{\text{mix}} A_{yz} \sin(2\theta) h_z \quad (4.3)$$

$$V_{\text{ISHE}} = I_c R = \theta_{\text{SH}} w d_{\text{Pt}} \overline{J}_S R \sin \theta \quad (4.4)$$

In these expressions, H is the externally applied magnetic field, H_{res} is the resonant field and ΔH is the linewidth of the resonance. ϕ_{coup} is the phase difference between the coupled current and the magnetisation precession. d_{Pt} and w are the thickness of the platinum layer and the width of the bar. $V_{\text{mix}} = -\frac{1}{2} I_{\text{mw}}^b \Delta R$ is the voltage coefficient of the AMR rectifying effect and ΔR and R are the AMR coefficient and the sample resistance respectively. A_{yz} is related to the off-diagonal term of the ac magnetic susceptibility by χ_{yz}/M_S , where M_S is the saturation magnetisation.¹³¹ The magnetisation always lies in the plane of the sample due to the demagnetisation field.

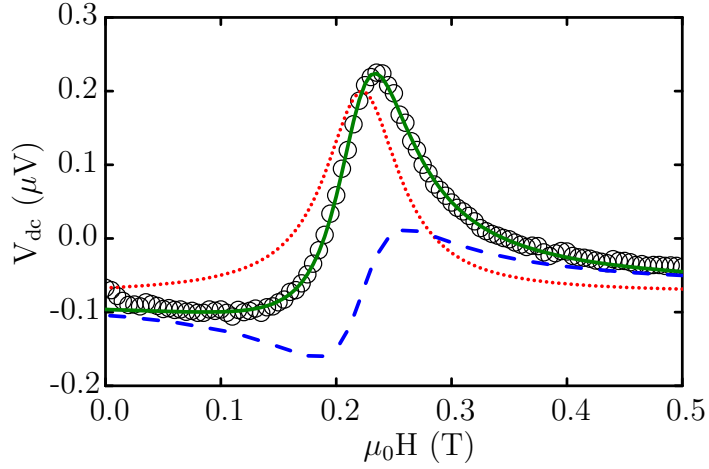


Figure 4.3: Detected voltage for a $d_{\text{Co}} = 2$ nm device for a single field sweep, with $\theta = 315$ degrees. The FMR peak is fitted (solid green line) by a combination of symmetric (dotted red line) and antisymmetric (dashed blue line) Lorentzian curves.

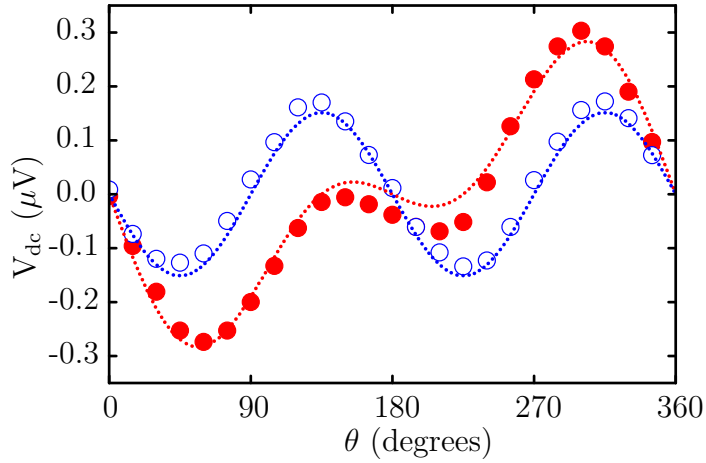


Figure 4.4: The angular dependences of the symmetric (full red circles) and antisymmetric (open blue circles) voltages are each fitted by a linear combination of $\sin \theta$ and $\sin 2\theta$ terms. The data shown is for the same $d_{\text{Co}} = 2$ nm device as measured in Fig. 4.3.

Only rectification detection can produce an antisymmetric Lorentzian, as the phase information needed to produce the asymmetry is held in the relative phase of the resistance and microwave current. Also observe that the two detection mechanisms have different angular dependencies, which allows them to be distinguished. The rectification voltage is proportional to $\sin 2\theta$ due to the symmetry of the AMR, whereas the angular dependence of the ISHE, given by the cross product in equation 4.1, makes the spin-pumping signal proportional to $\sin \theta$.

FMR resonances for a series of in-plane angles were measured and fitted with symmetric and antisymmetric Lorentzian peaks (see Figure 4.3), defining V_{sym} and V_{asy} as the coefficients of the symmetric and antisymmetric peaks in equation 4.2. The angular dependencies of both the symmetric and antisymmetric terms are fitted well by a combination of $\sin \theta$ and $\sin 2\theta$ components. Figure 4.4 shows the fitting for a sample with a 2 nm cobalt layer. Neither of the detection methods proposed explains the antisymmetric $\sin \theta$ component. This component is only significant in the 1 nm cobalt layer.

The measurements for the five cobalt thicknesses were repeated, using identical device structures, and the same experimental parameters. Measurements in a second device were repeated for all cobalt layer thicknesses except 1.75 nm to show the variation between devices. Figure 4.5 shows the detected voltages against cobalt thickness. Whilst there is a clear trend in the $\sin \theta$ components of both voltage parts, the $\sin 2\theta$ components are not consistent in magnitude or sign even between devices from the same layer structure. This can be attributed to variation in the relative phase of the microwave current coupled into each device bilayer, I_{mw}^{b} , and the microwave current in the coplanar stripline generating the magnetic field, I_{mw}^{w} . As the device and coplanar stripline microstructures are nearly identical, the amplitude and phase of I_{mw}^{b} are expected to be dominated by the milli-scale arrangement of bond wires and pads, which do vary between devices. The bond-wire lengths (~ 2 mm) are close to the free-space wavelength (20 mm) and could act as an antenna, coupling microwave current into the device bilayer. Unlike the rectification signal, the spin-pumping signal is insensitive to I_{mw}^{b} and consequently is reproducible between devices.

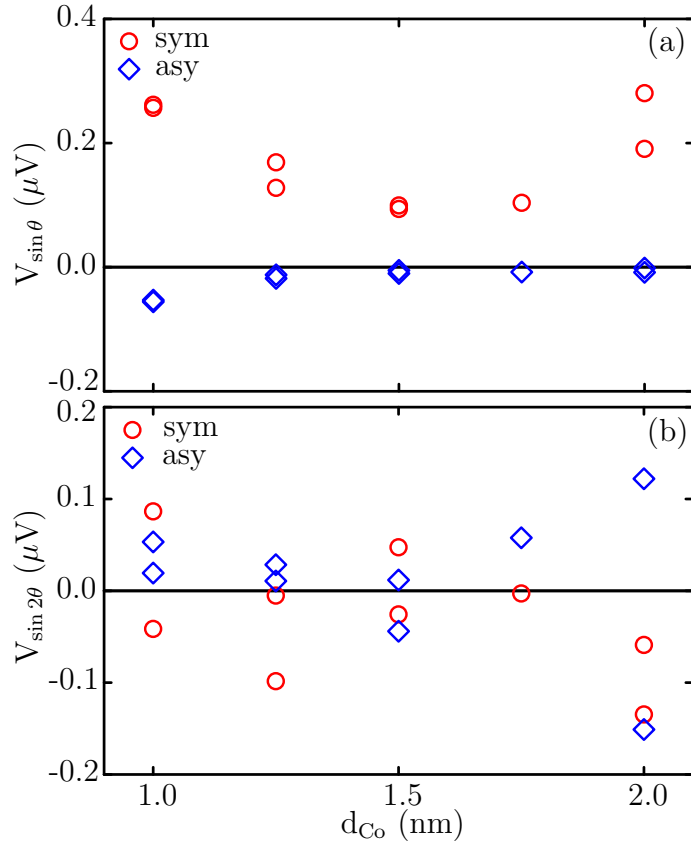


Figure 4.5: (a),(b) Cobalt thickness dependence of the fitted symmetric (red circles) and antisymmetric (blue diamonds) $\sin\theta$ and $\sin 2\theta$ voltage components.

4.3 Calculating the pumped spin-current

To determine the amount of pumped spin-current, first one must know the form of the magnetisation precession. In a small angle approximation, one can express the precession as a small perturbation of the magnetisation $M = (M_S, m'_y e^{j\omega t}, m_z e^{j\omega t})$ due to an excitation field $h = (0, 0, h_z e^{j\omega t})$, where the co-ordinate system is rotated so that the equilibrium magnetisation lies along \hat{x}' (see Figure 4.2b). Considering small angle precessions only in the plane of the material, the LLG equation can then be linearised to two coupled equations,

$$\begin{aligned} \frac{j\omega}{\mu_0\gamma} m'_y + \left(\frac{j\omega}{\mu_0\gamma} \alpha + H_0 + M_{\text{eff}} \right) m_z &= M_S h_z \\ \left(\frac{j\omega}{\mu_0\gamma} \alpha + H_0 \right) m'_y - \frac{j\omega}{\mu_0\gamma} m_z &= 0. \end{aligned} \quad (4.5)$$

Keeping terms linear in α , one finds that m'_y is purely real,

$$m'_y = - \frac{\mu_0 M_S}{\alpha \sqrt{(\mu_0 M_{\text{eff}})^2 + 4 \frac{\omega^2}{\gamma^2}}} h_z, \quad (4.6)$$

and m_z is complex, given by

$$m_z = \left(\alpha - j \mu_0 H_0 \frac{\gamma}{\omega} \right) m'_y. \quad (4.7)$$

The angular momentum dissipated from the precession can be found from the damping torque. The loss of angular momentum per precession period is proportional to

$$\int_0^{\frac{2\pi}{\omega}} \left[\mathbf{M}(t) \times \frac{d\mathbf{M}(t)}{dt} \right]_{x'} dt = \frac{2\pi}{\omega} \Re \left\{ m'_y \frac{dm_z(t)}{dt} - m_z \frac{dm'_y(t)}{dt} \right\}. \quad (4.8)$$

The spin-current density can now be calculated simply from equation 2.25 as¹³⁷

$$J_s^0 = \frac{g_{\text{eff}}^{\uparrow\downarrow} \gamma h_z^2 \hbar \mu_0 M_{\text{eff}} + \sqrt{(\mu_0 M_{\text{eff}})^2 + 4 \frac{\omega^2}{\gamma^2}}}{8\pi \alpha_{\text{eff}}^2 \left((\mu_0 M_{\text{eff}})^2 + 4 \frac{\omega^2}{\gamma^2} \right)}. \quad (4.9)$$

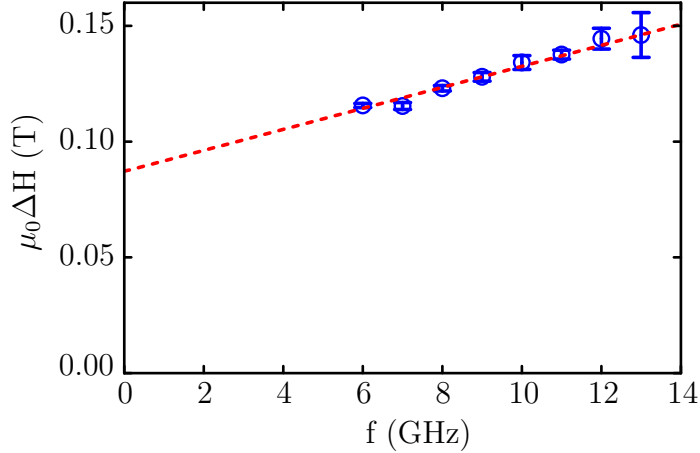


Figure 4.6: The effective Gilbert damping, α_{eff} , is proportional to the gradient of the FMR linewidth, ΔH , against frequency. The intercept gives the inhomogeneous part of the linewidth, ΔH_{in} . Data is shown for a $d_{\text{Co}} = 1$ nm device.

The Gilbert damping constant is modified to include a contribution, not only from the volume of the ferromagnet, but also from the spin pumping at the interface¹³⁷

$$\alpha_{\text{eff}} = \alpha_0 + \frac{g\mu_{\text{B}}g_{\text{eff}}^{\uparrow\downarrow}}{M_{\text{S}}d_{\text{Co}}}. \quad (4.10)$$

Likewise, the effective magnetisation has a bulk contribution from the demagnetisation field, but also from a perpendicular uniaxial anisotropy originating from the interface¹³⁸

$$M_{\text{eff}} = M_{\text{S}} - \frac{H_{\text{U}}^{\text{int}}}{d_{\text{Co}}}. \quad (4.11)$$

By measuring FMR out-of-plane of the sample and self-consistently fitting the magnetisation angle and resonant field to the Kittel equation and minimising the free energy, the effective magnetisation in each sample was determined.¹⁰² In this case the Kittel equation reduces to

$$\left(\frac{\omega}{\gamma}\right)^2 = \mu_0^2 (H_{\text{res}} - M_{\text{eff}} \cos 2\psi) (H_{\text{res}} - M_{\text{eff}} \cos^2 \psi), \quad (4.12)$$

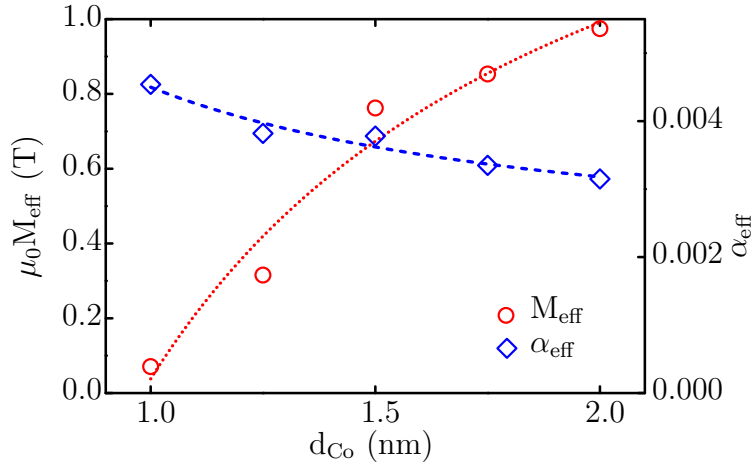


Figure 4.7: Measured values of M_{eff} (red circles) and α_{eff} (blue diamonds) are fitted well by equations 4.11 (dotted line) and 4.10 (dashed line) respectively.

and the free energy is given by

$$F = \frac{1}{2} \mu_0 M_S [M_{\text{eff}} \cos^2 \psi - 2H_{\text{res}}(\cos \psi \cos \psi_H + \sin \psi \sin \psi_H)]. \quad (4.13)$$

where ψ and ψ_H are defined in Fig. 2.1. A more comprehensive exposition of this fitting method is given in Chapter 5.2.

The effective Gilbert damping was calculated by measuring the frequency dependence of the linewidth, $\Delta H = \Delta H_{\text{in}} + \omega \alpha_{\text{eff}} / \gamma$ (Figure 4.6), where ΔH_{in} is the inhomogeneous contribution to the linewidth. Values of M_{eff} and α_{eff} are shown in Figure 4.7 and are fitted well by equations 4.10 and 4.11 when $g_{\text{eff}}^{\uparrow\downarrow}$ is constant for all the cobalt thicknesses, showing that there is no unexpected variation in the size of J_S^0 with d_{Co} .

The symmetric $\sin \theta$ voltage with the ISHE symmetry was converted to I_{dc} by dividing, for each device, by the individual resistance measured. Figure 4.8 shows both the charge current for the different layers and the relative size of the spin-current calculated from equation 4.9.

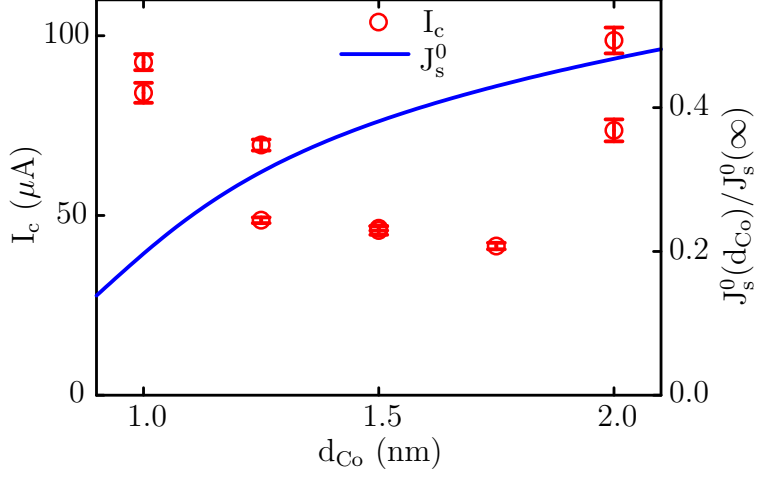


Figure 4.8: Cobalt thickness dependence of the spin-pumping charge current is plotted (red circles). The relative size of the spin-current (solid blue line), which is calculated using the fits to the measured values of M_{eff} and α_{eff} , decreases in the thinner layers. In contrast, the charge current increases in the thinner layers.

4.4 Calculating the spin-Hall angle

The initial spin-current J_S^0 at the interface decays due to spin relaxation as it penetrates the platinum layer, giving a spin-current profile,¹⁰²

$$J_S(z) = \frac{\sinh\left(\frac{d_{\text{Pt}} - z}{\lambda_{\text{sd}}}\right)}{\sinh\left(\frac{d_{\text{Pt}}}{\lambda_{\text{sd}}}\right)} J_S^0. \quad (4.14)$$

where λ_{sd} is the spin-diffusion length of the platinum. Integrating over the spin-current profile gives an average spin-current density,

$$\overline{J_S} = \int_0^{d_{\text{Pt}}} \frac{J_S(z)}{d_{\text{Pt}}} dz = \frac{\lambda_{\text{sd}}}{d_{\text{Pt}}} \tanh\left(\frac{d_{\text{Pt}}}{2\lambda_{\text{sd}}}\right) J_S^0, \quad (4.15)$$

which allows the charge current to be expressed as

$$I_c = \frac{2e}{\hbar} \theta_{\text{SH}} w \lambda_{\text{sd}} \tanh\left(\frac{d_{\text{Pt}}}{2\lambda_{\text{sd}}}\right) J_S^0 \sin \theta \quad (4.16)$$

The charge current generated in the device has a minimum at around 1.75 nm,

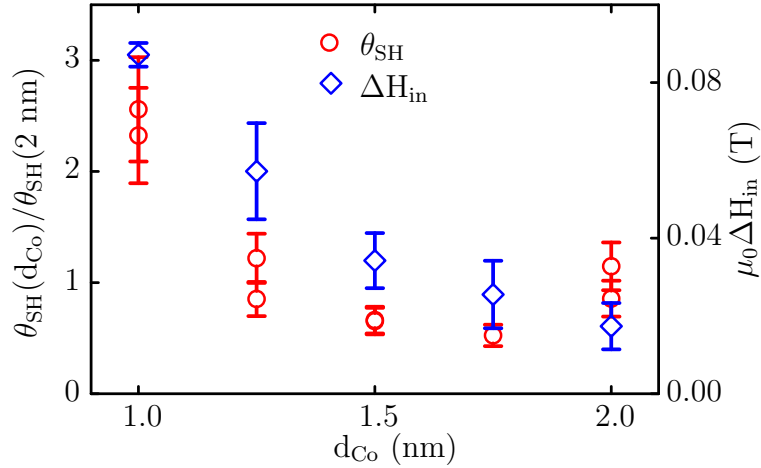


Figure 4.9: The relative size of θ_{ISHE} (red circles) is enhanced in the 1 nm cobalt layer. The error bars show the standard error from fitting the $\sin \theta$ parameter to the angle-dependent symmetric voltage data. The small variance between the data points of the same thickness could also be from a small difference in the size of the microwave field in each device. The inhomogeneous part of the linewidth (blue diamonds) also shows an increase in thinner cobalt layers.

whereas the spin-current decreases to zero as the ferromagnetic layer is reduced. The reproducibility of the results for each repeated measurement demonstrates that the increase in current in the thinnest layers cannot be attributed to variation in h_z between devices. This leads to the main conclusion of from this study: the conversion of the interfacial spin-current to charge current depends on the cobalt thickness. This result is surprising as previous studies of thicker Py/Pt bilayers have shown remarkable agreement with the theoretical model.^{132,137} However, the minimum thickness of the ferromagnetic layer measured in those studies was 5 nm, significantly thicker than the range measured here.

An increased efficiency of spin-current to charge current conversion was observed in the thinnest layers. Since the platinum thickness is the same for each device, the enhancement in the charge current should originate from the ISHE at the interface, and not the bulk ISHE in the platinum layer. The relative size of θ_{ISHE} , calculated from equation 4.4, is plotted in Figure 4.9 and shows an enhancement of 2.4 times between the 2 nm and 1 nm cobalt layer. The microscopic origin of this effect is not clear but the possibility of cobalt impurities in the platinum layer which could lead to a larger extrinsic SHE, as observed for impurities in other

materials,^{139,140} should be noted.

From XRR measurements, the surface roughness of the Co/Pt interface is found to be between 0.6 and 0.8 nm in all of the films, and no clear trend was observed, ruling out a simple explanation for the enhancement based on surface roughness in the thinner films. The inhomogeneous (frequency independent) part of the linewidth shown in Figure 4.9, indicates that the roughness in the cobalt layer increasingly affects the uniformity of magnetic anisotropy in the thinnest films. This increased non-uniformity correlates to the enhancement and may play an, as yet unexplained, part in the enhancement of θ_{SH} .

In the next chapter, spin-orbit effects in addition to the SHE will be considered in these systems. A possibility remains that the enhancement in the conversion of spin to charge current observed here could be due to an additional spin-orbit effect with symmetry indistinguishable from the ISHE.

In conclusion, the experimental observation of the increase in the ISHE in ultra-thin layers will motivate further theoretical work in this area. The observed enhancement raises the possibility of controlling layer thicknesses in the nanoscale regime to create devices for higher efficiency generation and read-out of spin-currents.

Chapter 5

Current induced torques in Co/Pt bilayers

Current-induced spin-orbit torques in ultra-thin ferromagnetic/heavy metal bilayers provide ways to electrically control magnetisation. Two mechanisms for observed torques have been proposed, both of which could contribute to the total torques and both of which originate in the spin-orbit interaction. A schematic of both mechanisms is shown in Figure 5.1a. The first mechanism is due to the spin-Hall effect,^{18–20,89} where a charge current in the heavy metal layer generates spin-currents perpendicular to the charge current. When a spin-current flows into the ferromagnetic layer, it can exert a spin-transfer torque (STT).^{23,24,41} This torque normally follows the anti-damping form predicted by Slonczewski¹⁵ and Berger,¹⁴¹ but it is known that a field-like non-adiabatic spin-transfer torque can also exist.^{51–53}

The second mechanism is a ‘Rashba’ spin-orbit torque. Due to the structural inversion-asymmetry of the two dissimilar materials at the interface, when a current is applied, the spin-orbit Hamiltonian breaks the degeneracy of the electron spin states near the interface, creating a non-equilibrium spin-accumulation. The electron spins in the ferromagnet, through exchange coupling, can then exert a torque on the magnetic moments. This was initially predicted to give a field-like torque, acting perpendicularly to the interface normal and injected current,^{111,142,143} which was later confirmed by experiments in ultra-thin Pt/Co/ AlO_x ^{32,39,50} and Ta/CoFeB/MgO¹⁴⁴ trilayers. However, further measurements in

these layers have confirmed the presence of an additional anti-damping torque.^{34,40} A recent experiment, in a single-layer ferromagnet with broken symmetry, has shown that this anti-damping torque can be explained by the precession of the spins, initially polarised along the magnetisation, around the additional current-induced spin-orbit fields.⁴⁹ These additional torques have also been modelled theoretically in metal bilayer systems.^{113,114}

The torques are further complicated by the additional Oersted torque in the ferromagnetic layer, due to the total current in the heavy metal, which has the same symmetry as the field-like torque. Considering only the lowest order terms,³⁴ the total torques can be formulated as

$$\boldsymbol{\tau} = \tau_{\text{AD}} \hat{\mathbf{m}} \times \hat{\mathbf{y}} \times \hat{\mathbf{m}} - (\tau_{\text{F}} + \tau_{\text{Oe}}) \hat{\mathbf{y}} \times \hat{\mathbf{m}}, \quad (5.1)$$

where the anti-damping (τ_{AD}) and field-like (τ_{F}) torques can have contributions from both the spin-Hall and Rashba effects. Previous studies have tried to disentangle these two effects by studying the dependence of the torques on the thickness of the two layers.^{33,35} In particular, Fan *et al.* observed an additional field-like torque in Py/Pt layers with the same direction as the Oersted field.³⁵ In this study, a similar field-like torque is observed, emerging only in the ultra-thin Co layer regime, but opposing the Oersted field. This suggests that the field-like torque is sensitive to details of the sample composition and growth and can vary significantly, possibly due to competing mechanisms.

5.1 SO-FMR in Co/Pt bilayers

The waveguide devices used in Chapter 4 to measure the spin-pumping in Co/Pt layers were also used to perform spin-orbit FMR measurements. In this case the waveguide was not used to create a microwave field, but the current-induced fields, which are the interest of this study, were used to generate microwave fields from a microwave current injected directly into the device. The symmetry of the detected voltages then allow the form of the current-induced fields to be determined. A schematic of the magnetisation precession, and the directions of the torques in this measurement is shown in Figure 5.1b.

Initially, measurements were made with an external bias tee to separate the

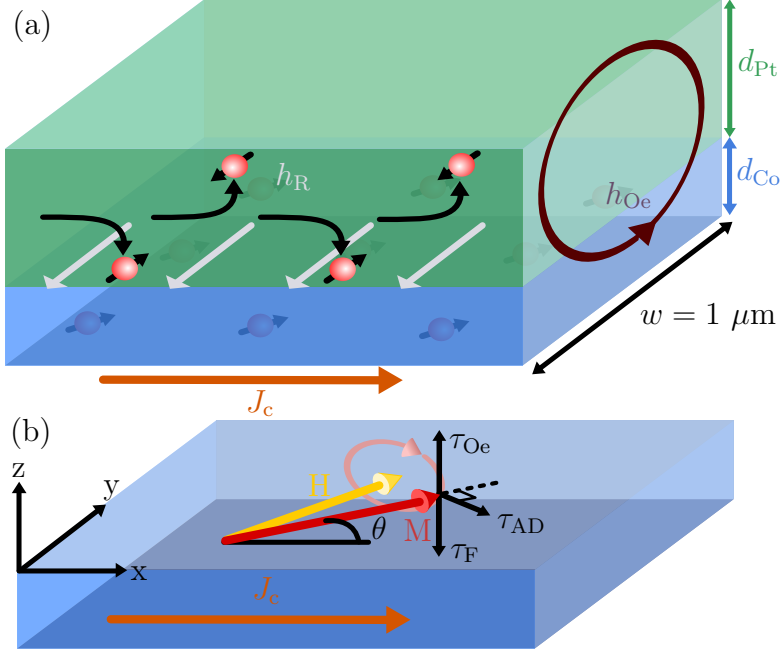


Figure 5.1: (a) A charge current density, J_C passing through the bilayer induces a transverse spin-current in the platinum due to the spin-Hall effect which flows into the cobalt layer. At the interface, due to the structural inversion asymmetry, the conduction electrons experience an effective magnetic field, h_R . The cobalt has an additional oxidised silicon interface which could also similarly produce an effective magnetic field. The current passing through the platinum also induces an Oersted field in the cobalt, due to Ampère's law. (b) The Oersted field induces an out of plane torque on the cobalt magnetisation, τ_{Oe} . Additional anti-damping and field-like torques, τ_{AD} and τ_F respectively, are induced due to the exchange interaction of the non-equilibrium spin-density in the ferromagnet with the magnetisation. A field-like torque with negative coefficient is shown here opposing a positive Oersted torque.

dc and microwave signals. However, as is explained in Appendix A, increased microwave power transmission to the device can be achieved by using a resonator circuit. Microwave power was delivered to the circuit board via a semi-rigid coaxial cable. This was connected to a microstrip transmission line on the circuit board which was terminated by a wirebond to one end of the sample. The other end of the sample was connected to ground via another wirebond. An on-board bias-tee (see Appendix A.3.2),¹⁴⁵ comprising of an in-line gap capacitor and a wirebond as an inductor, was used to separate the injected microwave power from the measurement of the dc voltage, V_{dc} , across the bar.

Measurements were made in the electromagnet system described in Chapter 3.2. The ground plane of the PCB is grounded to the aluminium probe by screwing the PCB into the probe. When the probe is mounted, the PCB is positioned horizontally, with the field in the plane of the sample. A through-connector in the lid of the probe allows a semi-rigid coaxial cable to be connected to a SMP connector on the PCB. A freely rotating right-angled SMP connector is placed in the semi-rigid line to allow rotation of the probe between the electromagnet poles without reconnecting the microwave line.

V_{dc} , generated by the rectifying magnetoresistance of the sample, is measured across the bias-tee wirebond to ground. This is achieved by routing an insulated wire for the bias-tee through a small hole in the probe lid sealed by aluminium tape. On top of the probe, the wire is soldered to a thicker measurement wire and clamped. A second measurement wire is clamped into contact with the probe body. The two measurement wires are twisted together to minimise the ground loop.

A microwave signal pulse-modulated at 234.56 Hz is used to excite FMR, and the modulated V_{dc} is detected with a lock-in amplifier. Source microwave powers of 20 dBm were typically used. The microwave frequencies used for these experiments were between 16 and 19 GHz for each device. The frequency used was high enough that the FMR peak was higher in magnetic field than the saturation curve of the background signal. For each FMR trace, the external magnetic field is swept from high to low field. FMR sweeps are taken every 10 degrees in the plane of the sample by use of a programmable rotation stage to which the probe is fixed. The external field can be rotated out of the plane of the sample by use of a separate probe in which the same PCB is mounted vertically.

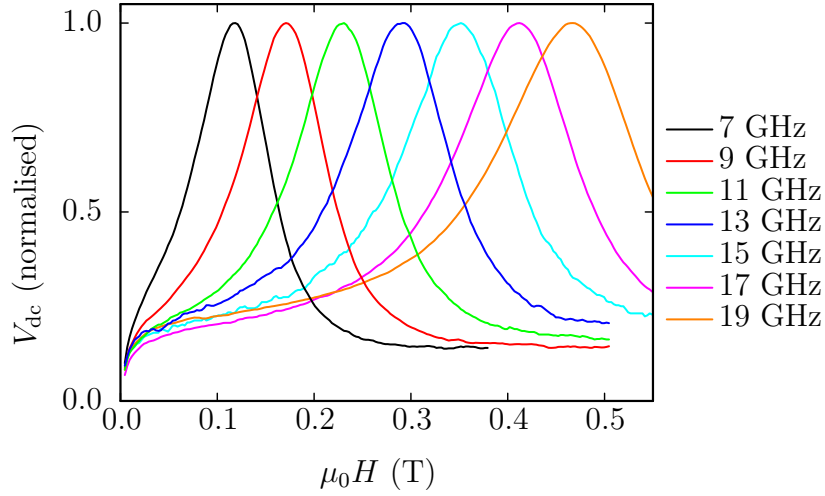


Figure 5.2: Normalised field sweeps measured as a function of external field, H , for a series of frequencies. Data shown is for a $d_{\text{Co}} = 1.25$ nm device.

These measurements were made at room temperature (in contrast to the previous measurements at 250 K in the vector cryostat system). The ambient temperature is controlled by the air-conditioning of the room, which is stable to within approximately 2 K deviation. To properly analyse the SO-FMR data at this different temperature, the magnetic anisotropies must be determined again by taking both a series of frequency and out-of-plane angle dependent FMR sweeps.

To determine the size of the AMR, which allows the resonance to be detected, the bias-tee and ground connections are used to make a 2-point measurement of the resistance. The rotation stage is rotated every degree through a constant saturating field and the resistance measured.

5.2 Results and analysis

To completely characterise the anisotropies of the materials studied, FMR sweeps were made for a series of angles in and out of the sample plane, as well as for a series of microwave frequencies at a constant angle in the plane of the sample. The FMR sweeps were fitted in the same way as the previous chapter with a combination of symmetric and antisymmetric Lorentzian peaks with a linear background. FMR sweeps made for a series of microwave frequencies are shown in Figure 5.2.

First the angle-dependence of the resonant field should be considered. The

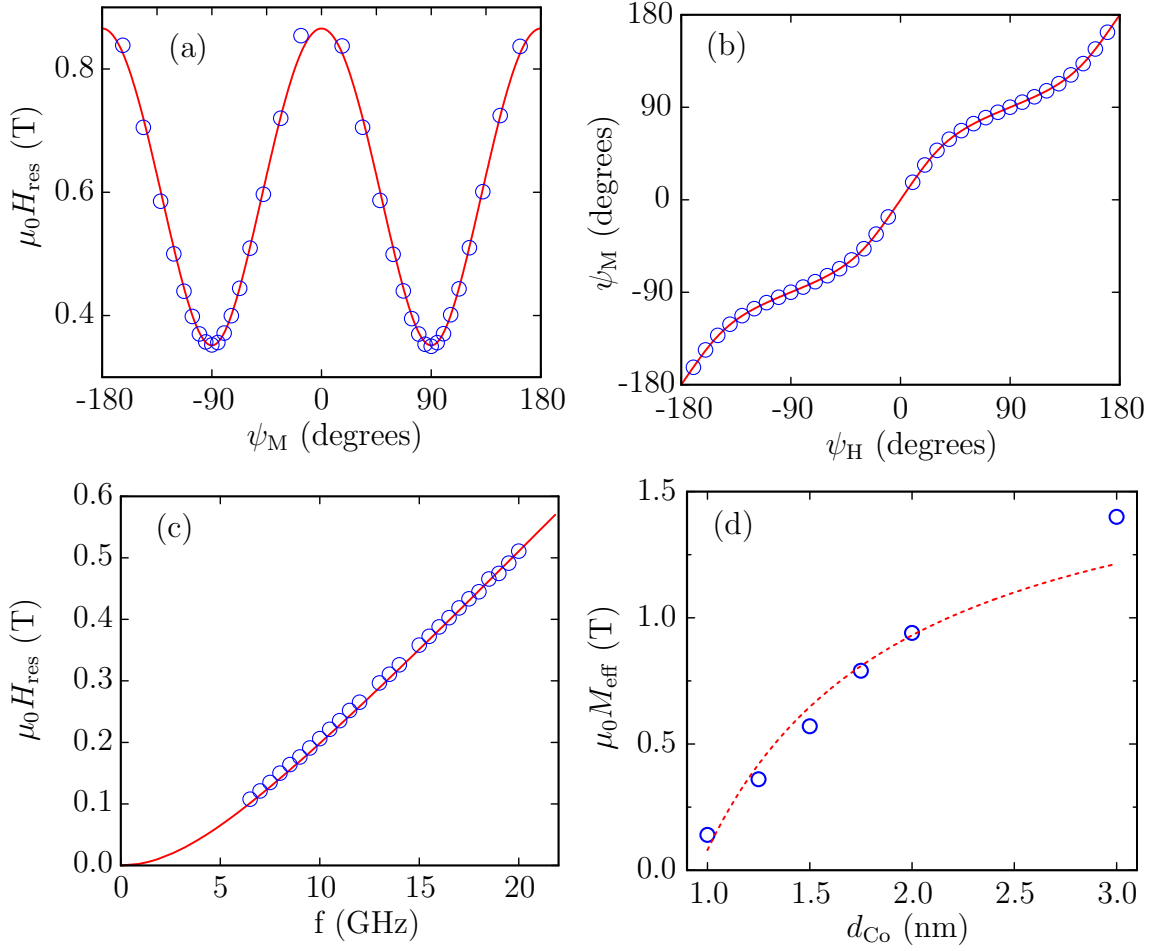


Figure 5.3: For a $d_{\text{Co}} = 1.25$ nm device, self consistent fits of (a) the resonant field, H_{res} , as a function of the out-of-plane magnetisation angle, ψ_M , (b) ψ_M as a function of the out-of-plane field angle, ψ_H and (c) H_{res} as a function of frequency. (d) The self-consistent fits allow the effective magnetisation, M_{eff} to be deduced for each value of d_{Co} . The trend follows closely the predicted $1/d_{\text{Co}}$ dependence.

resonant field shows little dependence on the in-plane magnetisation angle, but for most of the layer types, there is a strong dependence on the out-of-plane angle. This indicates that there is little in-plane anisotropy, which is consistent with the polycrystalline nature of the samples.

The values of M_{eff} and γ , for a particular layer, can be determined by fitting the angle and frequency dependence of the resonant field to the free energy and Kittel equations. The angle of the magnetisation, ψ_M is a variable in the free energy equation which depends on the external field angle, ψ_H and M_{eff} . These angles are defined in Fig. 2.1. The equations are fitted in an iterative process. For a given set of initial fitting parameters, a least squares fit to the Kittel equation is first performed on the out-of-plane and frequency dependent data with M_{eff} and γ as the free parameters. Then the free energy is minimised by varying ψ_M for each data point using the previously fitted parameters as constants. The process is repeated until the fits converge. For a device with $d_{\text{Co}} = 1.5$ nm, the fitted out-of-plane resonant fields are shown in Figure 5.3a; the fitted polar angle, ψ_M , of the magnetisation is plotted in Figure 5.3b and the fitted frequency dependence of the resonant field is shown in Figure 5.3c.

For each layer studied, no trend was observed in the fitted value of γ , with a value determined to be $1.90 \pm 0.05 \times 10^{11}$ rad s⁻¹T⁻¹. This corresponds to a g-factor of 2.16 ± 0.06 , agreeing within error with the literature value of 2.18 for FMR in cobalt.¹⁴⁶ The fitted values of M_{eff} as a function of d_{Co} are plotted in Figure 5.3d. The results, unsurprisingly, are similar to the fitted values from the 250 K spin-pumping data in the previous chapter. M_{eff} decreases with cobalt thickness showing the competing effects of shape anisotropy and the interfacial anisotropy. To find the effective spin-orbit fields from the fitted lorentzian peak voltages, the ac magnetic susceptibility has to be calculated from the resonant field, linewidth and fitted anisotropy values.

For all the sweeps measured, the symmetric part dominates the antisymmetric part. The effective fields are fitted to V_{sym}/A_{yz} and V_{asy}/A_{yy} using equations 3.6 and 3.7 (Figure 5.4a). Empirically it is seen that the symmetric angular dependence can be almost entirely fitted by an anti-damping torque ($h_z \propto \cos \theta$) and that the antisymmetric angular dependence can be almost entirely fitted by a field-like term (h_y independent of magnetisation angle). Small additional terms which are not consistent in size or sign from device to device are needed for the

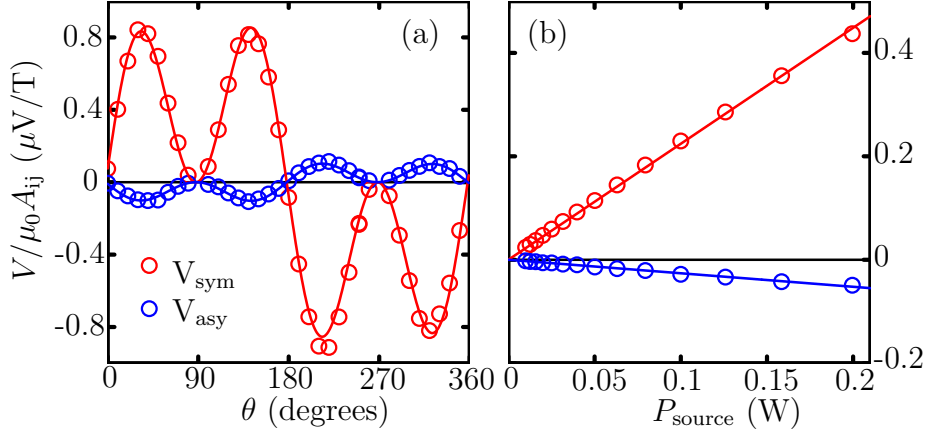


Figure 5.4: (a) The angular dependence of V_{sym}/A_{yz} and V_{asy}/A_{yy} (shown for a device with $d_{\text{Co}} = 1.5$ nm) are fitted well by an in-plane anti-damping torque (τ_{AD}) and a combined out of plane Oersted and field-like driving torque ($\tau_{\text{Oe}} + \tau_{\text{F}}$) respectively. (b) Both voltages peaks observed scale linearly with the microwave source power, as expected from the theoretically linear dependence on current of the spin-Hall and Rashba effects.

fitting (h_z independent of angle and $h_y \propto \cos \theta$). These terms are consistent with additional field-like and anti-damping torques with symmetry $\boldsymbol{\tau} \propto \hat{\mathbf{z}} \times \hat{\mathbf{m}}$ and $\boldsymbol{\tau} \propto \hat{\mathbf{m}} \times \hat{\mathbf{z}} \times \hat{\mathbf{m}}$ respectively. Torques with these symmetries have been proposed to exist due to a combination of a Rashba spin-orbit field and anisotropic spin relaxation rates.¹⁴⁷ Most significantly, it is observed that as the cobalt thickness is reduced from 3 to 1 nm, the sign of the symmetric voltage stays constant, whilst the sign of the antisymmetric voltage flips (see Figures 5.5a and b). This indicates that as the cobalt thickness is reduced the direction of the field-like torque reverses. The voltages measured scale linearly with power (Figure 5.4b), showing the torques are proportional to current density (as V_{mix} is proportional to microwave current).

Previously, in thicker Py/Pt layers, Liu *et al.*²³ calibrated the size of the spin-Hall effect by using the ratio of the symmetric to antisymmetric voltages. In this case, it was assumed that the antisymmetric voltage was purely due to the Oersted field. Because both the spin-Hall and Oersted effective fields are generated from the same current, θ_{SH} can be calculated from the ratio of the voltages.

The Oersted field is given by Ampère's law for an infinite conducting sheet as

$$\mu_0 \mathbf{h}_{\text{Oe}} = -\frac{I_{\text{Pt}}}{2w} \hat{\mathbf{y}} = -\frac{J_{\text{Pt}} d_{\text{Pt}}}{2} \hat{\mathbf{y}}, \quad (5.2)$$

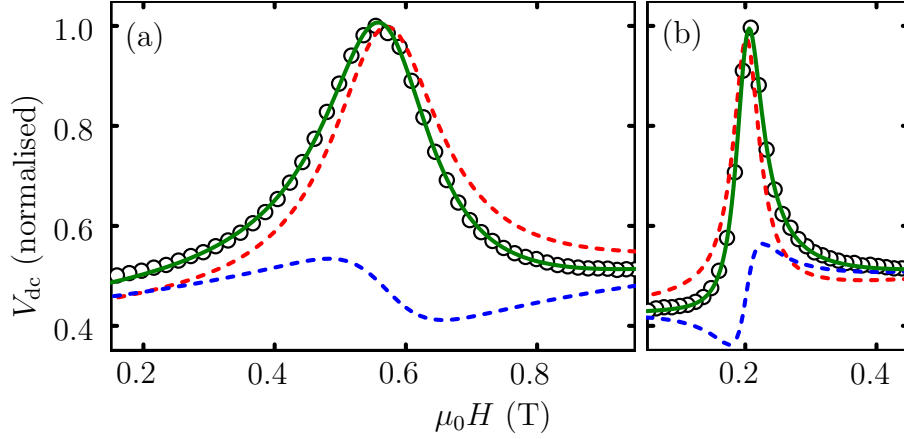


Figure 5.5: (a) The resonance in V_{dc} (open circles) for a device with $d_{Co} = 1$ nm, measured with a microwave frequency of 19 GHz, is fitted (solid green line) by a combination of antisymmetric (dashed blue line) and symmetric (dashed red line) Lorentzians. (b) The resonance fitted for a $d_{Co} = 3$ nm device, measured at 16 GHz, shows a reversal in sign of the antisymmetric part compared to $d_{Co} = 1$ nm.

and the effective field for the spin-Hall spin-transfer torque is

$$\mu_0 \mathbf{h}_{SH} = \frac{-J_S^0}{M_S d_{Co}} \hat{\sigma} \times \hat{\mathbf{m}}. \quad (5.3)$$

These are detected in V_{dc} (for $\hat{\sigma}$ in $-\hat{y}$ direction) as

$$\frac{V_{asy}}{A_{asy}} = \frac{I_{tot} \Delta R}{2} \sin 2\theta \frac{J_{Pt} d_{Pt}}{2} \cos \theta \quad (5.4)$$

and

$$\frac{V_{sym}}{A_{sym}} = \frac{I_{tot} \Delta R}{2} \sin 2\theta \frac{J_S^0}{M_S d_{Co}} \cos \theta \quad (5.5)$$

respectively. The interfacial spin-current density, J_S^0 is related to the total spin-current density by

$$J_S^0 = J_S \left[1 - \operatorname{sech} \left(\frac{d_{Pt}}{\lambda_{sf}} \right) \right]. \quad (5.6)$$

Hence the spin-Hall angle can be calculated from the fitted $\cos \theta \sin 2\theta$ components

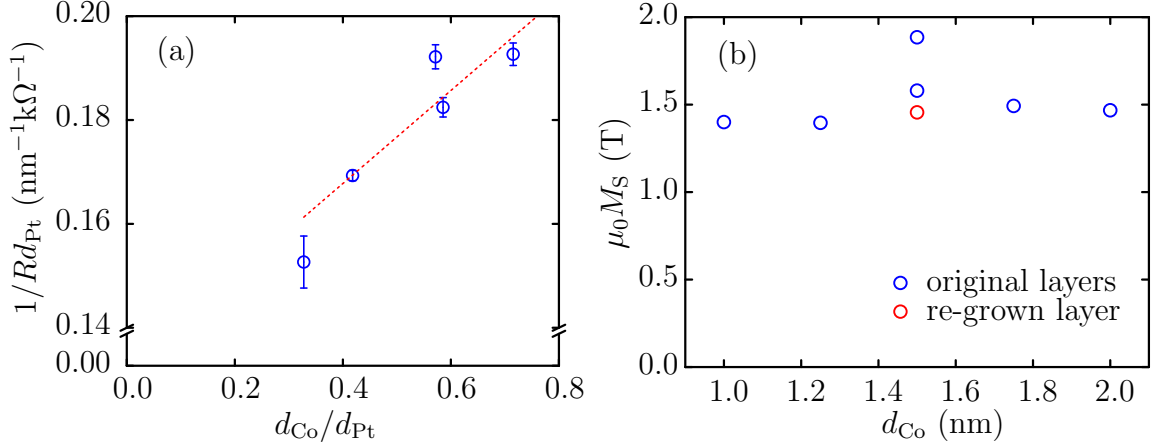


Figure 5.6: (a) The individual resistivities of the Pt and Co layers are deduced by measuring the total resistance of Hall bars as a function of layer thicknesses. (b) The saturation magnetisation of the layers in the range $d_{\text{Co}} = 1$ to 2 nm was measured by SQUID magnetometry as ~ 1.45 T in all layers, except in the $d_{\text{Co}} = 1.5$ nm layer in which measurements of two parts of the wafer showed consistently higher values. A re-grown layer showed a more consistent value, and this was the layer used for the devices presented in this chapter.

(for $\hat{\sigma}$ in $-\hat{y}$ direction) as

$$\theta_{\text{SH}} = \frac{2e}{\hbar} \frac{J_{\text{S}}}{J_{\text{Pt}}} = \frac{V_{\text{sym}} A_{\text{asy}}}{V_{\text{asy}} A_{\text{sym}}} \frac{e}{\hbar} M_{\text{S}} d_{\text{Co}} d_{\text{Pt}} \frac{1}{1 - \text{sech}\left(\frac{d_{\text{Pt}}}{\lambda_{\text{sf}}}\right)}. \quad (5.7)$$

A positive value of σ , in this definition, gives a negative spin-Hall angle.

For the series of layers measured, the saturation magnetisation of the layers was measured by SQUID magnetometry*. These values are shown in Figure 5.6b. Using these measured values, θ_{SH} is plotted against d_{Co} in Figure 5.7. Contrary to the measurements by Liu *et al.*, the values of θ_{SH} calculated in this thickness range are not independent of d_{Co} and change in sign, indicating this calibration is flawed. From the sign flip of τ_{F} , this is partly due to a non-Oersted contribution to τ_{F} .

The relative sizes of the fitted torques can be compared as they are induced by the same current. Figure 5.8 shows the ratio of the total field-like to anti-damping torques ($(\tau_{\text{F}} + \tau_{\text{Oe}})/\tau_{\text{AD}}$) for the range of cobalt thicknesses measured. A

*Mu Wang kindly measured the magnetisation in these layers.

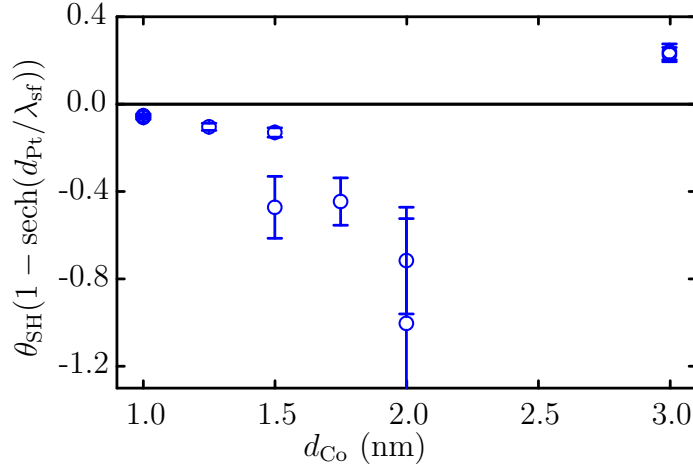


Figure 5.7: The effective spin-Hall angle, $\theta_{\text{SH}}(1 - \text{sech}(d_{\text{Pt}}/\lambda_{\text{sf}}))$, self-calibrated from the fitted Lorentzians using equation 5.7, is not constant with d_{Co} , indicating the calibration is flawed.

theoretically calculated ratio is also shown for the case where the field-like torque is purely Oersted and the anti-damping torque is due to the spin-transfer torque of the spin-Hall spin-current. The calculated ratio depends on the values of θ_{SH} and the spin-diffusion length, λ_{sf} , of platinum.²³ Here, $\theta_{\text{SH}} = 0.08$ has been used (as reported by Liu *et al.*²³) for $\lambda_{\text{sf}} = 1, 2$ and 3 nm. For this calculation saturation magnetisation values, found from SQUID measurements, of $\mu_0 M_{\text{S}} = 1.45 \pm 0.05$ T have been used. As the Co layer becomes thicker the ratio converges with the theoretical curve for $\lambda_{\text{sf}} = 1$ nm.[†] However, as d_{Co} reduces below around 2 nm, the ratio become negative and diverges from the theoretical curves, indicating the presence of an additional field-like torque, τ_{F} , which increasingly opposes the Oersted torque. If more conservative values for the theoretical modelling are used (larger λ_{sf} , smaller θ_{SH}), τ_{F} is even larger.

This reversal in sign of the total field-like torque has not been observed before in Co/Pt. The sign of τ_{F} and τ_{AD} measured here is consistent with the torques observed by Garello *et al.* at low frequency in an AlOx/Co(0.6 nm)/Pt(3nm) device.³⁴ Equally, in the $d_{\text{Co}} = 3$ nm layer, where τ_{F} is weakest, the torques resemble those measured by Liu *et al.* at microwave frequencies in Py(4 nm)/Pt(6 nm)²³ and CoFeB(3 nm)/Pt(6 nm).²⁴

[†]This is smaller than most reported values of the spin diffusion length for platinum, although recent measurements have reported similar values of 1.2¹⁴⁸ and 1.4 nm⁹⁸

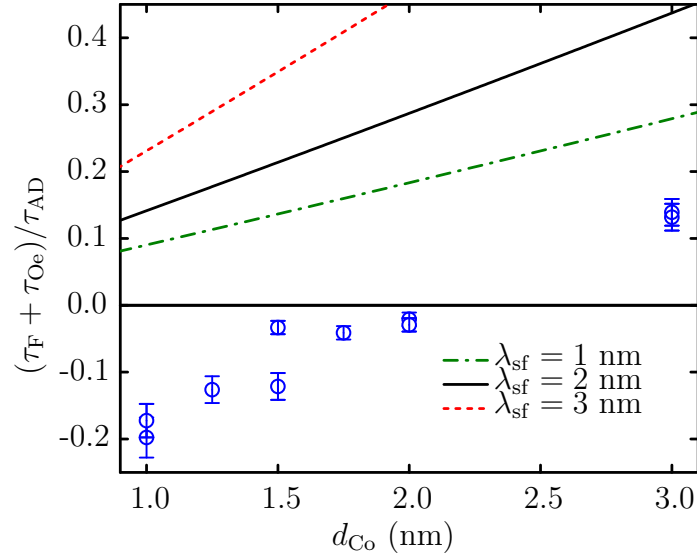


Figure 5.8: The ratio of the sum of the Oersted and field-like torque to anti-damping torque is calculated for a series of cobalt thicknesses ($d_{\text{Pt}} = 3$ nm). The error bars show the uncertainty due to the fitting of the torque values to the data. Further scatter in the data may be due to variation within each layer studied. Additionally shown is the calculated torque ratio for the model presented by Liu *et al.*²³ where only the Oersted torque and the anti-damping torque purely due to the spin-transfer torque of the spin-Hall spin-current are considered. Theoretical curves are plotted for $\theta_{\text{SH}} = 0.08$ (the same as Liu *et al.* reported for their self-calibration method), for Pt spin-diffusion lengths of 1, 2 and 3 nm.

Kim *et al.* have studied the torques at low frequency as a function of ferromagnet thickness (0.9 to 1.3 nm) in CoFeB/Ta(1 nm).³³ They observed a constant τ_{AD} with opposite sign, because the spin-Hall angle is negative in Ta. τ_F increased in the thinner ferromagnet layers, but in contrast to the Co/Pt layers studied here, added to the Oersted torque.

Fan *et al.* have measured the torques at low frequency, with a Cu spacer layer inserted between a Py and Pt layer.³⁵ A field-like torque was observed even with the spacer layer, and reduced with increasing spacer thickness, indicating that the torque was likely to be a non-adiabatic STT. As the ferromagnet thickness was reduced, the torque increased and added to the Oersted torque. This is the opposite sign to the τ_F observed here in Co/Pt. Fan *et al.* also studied CoFeB/Ta layers using electrically driven FMR. It could be seen that as the ferromagnet layer is reduced, the field-like torque increases, and opposes the Oersted field. This is the opposite sign to the observation of Kim *et al.*

When trying to reconcile these previous measurements with the observation made here, it is likely that differing material parameters in each experiment, the quality of the interfaces and the degree of oxidation of the additional ferromagnet interface could give quite different results. Nonetheless, the trend and sign of the field-like torque observed is consistent with the studies by Liu *et al.* and Garello *et al.* Furthermore, if the direction of the Rashba field is inverted in CoFeB/Ta compared to Co/Pt,¹⁴⁴ or if the non-adiabatic STT depends on the negative sign of the SHE in Ta, this result can also be consistent with Kim *et al.* and an earlier measurement by Suzuki *et al.*¹⁴⁴ The sign of τ_F measured here opposes the Oersted field and is opposite to the one measured by Fan *et al.* in Py/Pt. This can be explained by the measured torque having a different origin from Fan *et al.* The measurements by Fan *et al.* with Cu spacers strongly indicate a non-adiabatic STT origin in their case. In contrast, the τ_F observed here opposing the Oersted field is consistent with a Rashba field, with opposite sign to the non-adiabatic STT observed by Fan *et al.*, dominating in this material.

Furthermore, the inverse measurement in these same layers presented in Chapter 4, where an on-chip stripline was used to excite FMR can be considered in the context of this result. In that measurement, spin-current was pumped across the interface, and an induced voltage was measured from the inverse spin-Hall effect. In that measurement, an enhancement in the induced voltage was observed to

which an origin could not be attributed. It should be now noted that the spin-galvanic effect in this system (what could be called the inverse-Rashba effect), has the same symmetry as the inverse spin-Hall effect¹⁴⁹ and can explain the enhanced voltage in the thin ferromagnet layers. This provides further evidence that a proportion of τ_F , observed here, is due to the effective Rashba field.

5.3 Heating calibration

As it is clear that the self-calibration method is not reliable for calculating field sizes in these ultra-thin layers, it would be desirable to have an alternative way of determining the current in these layers. The spin-orbit fields in (Ga,Mn)As layers have previously been calibrated by Joule heating.⁴⁵ The same technique was used to try and calibrate the current-induced torques in these Co/Pt layers.

At low frequencies, the reactance of the circuit is negligible, and therefore the power dissipated is simply given by Joule's Law, $P_{dc} = I_{dc}^2 R$. At higher frequencies, the reactance of the circuit becomes significant and the 50 Ω microwave source and load are not impedance matched. Hence a proportion of the source power is reflected, and without specific knowledge of the reactance of the sample the microwave current, I_{mw} , in the sample is not known.

By comparing the response in sample resistance to heating by the dc power and microwave power, the proportion of microwave source power dissipated in the sample can be calibrated. For a small amount of heating, $\delta R \propto \delta P$, and so the proportion of the source microwave power dissipated in the sample is given by

$$P_{\text{sample}} = \frac{\partial P_{dc}}{\partial R} \frac{\partial R}{\partial P_{mw}} P_{\text{source}}. \quad (5.8)$$

To compare the change in resistance due to heating by dc or microwave currents, a small 20 mV_{p-p} sine wave at 123.45 Hz was applied by a function generator across the sample. The resistance was calculated by measuring the resulting current through the sample with a lock-in amplifier. To measure the effect of dc heating, an offset voltage was added to the sine wave from the function generator. In contrast, to measure the effect of microwave heating, no offset voltage was applied by the function generator, but a constant microwave signal was applied to the sample via the microwave line.

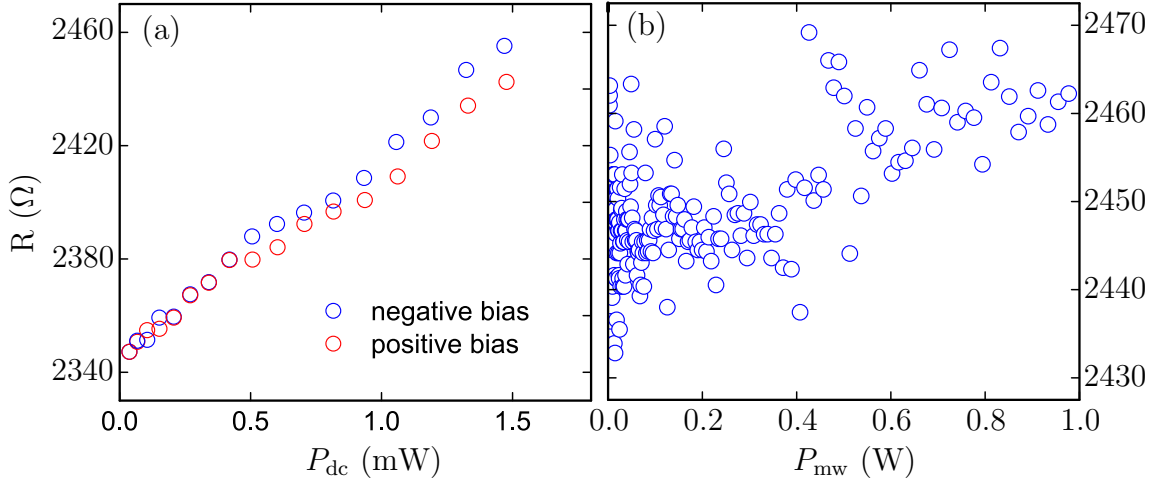


Figure 5.9: (a) Dependence of resistance on dc power in a Co(2nm)/Pt(3nm) sample. The relationship is approximately linear, as expected for small heating. The dependence is similar for positive and negative dc bias. (b) Dependence of resistance on microwave power. There is a positive correlation between resistance and power, but the signal to noise ratio is very poor.

The results for the dc heating are shown in Figure 5.9a. The resistance for both a negative and positive applied dc bias shows a linear response to power. There is a small discrepancy between the gradient for negative and positive bias that becomes particularly apparent at high bias. The effect of heating by microwave current can be seen in Figure 5.9b. In contrast to the dc case, there is not a clear relationship between resistance and applied power as the signal to noise ratio is very poor up to the maximum source power available (1 W). This is partly because the thermal coefficient of resistance is very small. A positive correlation can be seen between R and P_{mw} , but a good calibration can not be made with the data. Notice though, that an upper bound can be put on $\partial R/\partial P_{mw}$ of $30 \text{ } \Omega W^{-1}$, giving a power delivery of no better than $\sim 0.05\%$.

The calibration requires large currents, of order 1 mA, to be put through the samples, because of the small temperature coefficient of resistance. Although for a few samples, this reliably gave data for dc heating, quite frequently this also destroyed the samples. From resistivity studies of thicker cobalt films,^{150,151} the temperature coefficient of resistivity can be estimated as $\partial\rho/\partial T \cdot 1/\rho = 2 \times 10^{-3} \text{ K}^{-1}$. From the heating data this corresponds to a temperature change of 17 K mW^{-1} . This is a very rough estimation, because the dependence of resistivity on

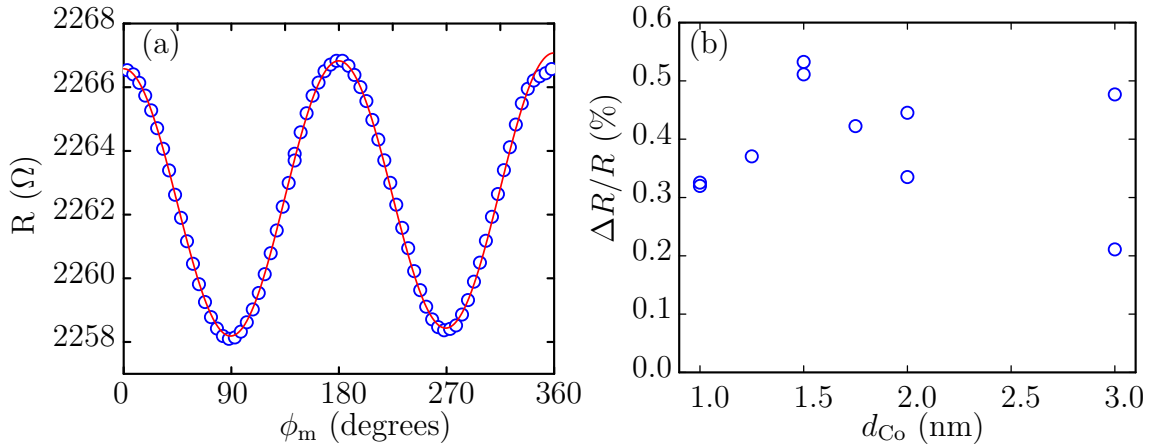


Figure 5.10: (a) A typical AMR curve for a $d_{Co} = 1.25$ nm device. (b) The AMR coefficient shows no trend with d_{Co} , and varies around 0.4% of the resistance

temperature may differ significantly in these ultra-thin films.

5.4 Conclusions

Although the size of the current-induced fields could not be accurately calibrated by the heating calibration, the upper bound it places on the efficiency of the microwave power delivery allows an upper limit for the spin-Hall angle to be calculated. By measuring the resistivity of Hall bars as a function of cobalt thickness (see Figure 5.6a), the resistivity of the Co and Pt layers is calculated as 113 and 76 $\mu\Omega\text{cm}$ in the ultra-thin regime. The proportion of microwave current in the Pt layer can then be derived from these resistivities. Combined with the measured values of M_S from SQUID and the coefficient of AMR from magnetoresistance measurements (see Figure 5.10) and using equation 5.5, the upper-bound of the spin-Hall angle in the 2 nm cobalt layer is calculated to be $\sim 10\%$. This can be compared to the spin-Hall angle of 7.6% calculated by Liu *et al.*,²³ using their similar current-induced FMR technique.

By looking at the ratio $(\tau_{Oe} + \tau_F)/\tau_{AD}$, it becomes easier to study how the additional field-like torque changes with cobalt thickness, relative to the anti-damping torque. As the cobalt layer thickness is reduced, the additional field-like torque increases in size and opposes the Oersted torque, becoming larger in layers thinner than 2 nm. This is consistent with the emergence of a Rashba field with

negative sign.

Chapter 6

A room temperature crystal spin-orbit torque

Although most of the recent research focus concerning spin-orbit torques has been on ultra-thin metal bilayers, the spin-orbit torques were first observed in thin-film (Ga,Mn)As devices.³¹ While this material is only magnetic at cryogenic temperatures, (Ga,Mn)As is an excellent system in which to study the underlying physics. Most importantly, the spin-orbit torques are induced by the bulk inversion-asymmetry of the crystal structure and therefore have a ‘Dresselhaus’ cubic symmetry^{31,45} which enables them to be distinguished from non-crystalline effects. While the ‘Rashba’ symmetry spin-orbit torques observed in metal bilayers^{39,40} can not be easily distinguished by symmetry from the spin-Hall spin-transfer torque or the Oersted torque, the origin of the torques in (Ga,Mn)As is unambiguous.

When a current flows through the inversion-asymmetric zinc-blende (Ga,Mn)As crystal, a spin-accumulation is induced in the hole population.³⁰ In low-temperature ferromagnetic (Ga,Mn)As this exerts a torque through exchange coupling to the local magnetic moments on the Mn ions.^{111,112,152} In room temperature (Ga,Mn)As the spin-accumulation still exists, although the material is no longer ferromagnetic. In analogy to the Rashba symmetry torques which are reported in metal bilayers, one might also consider whether this spin-accumulation could exert a torque on an adjacent ferromagnetic layer.

In this chapter, a room temperature spin-orbit torque arising from crystal

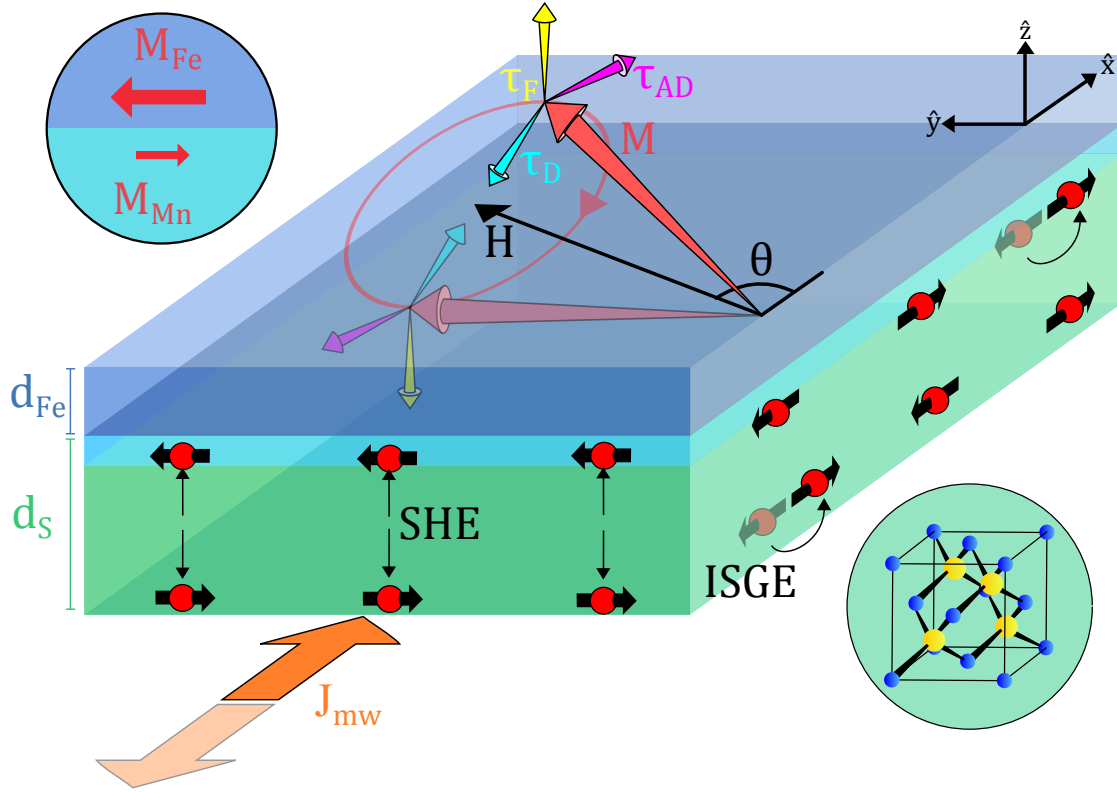


Figure 6.1: Schematic of the device. The Fe ions at the interface, through the exchange interaction, ferromagnetically order a few monolayers of Mn ions opposing the Fe magnetisation. Due to the inversion-asymmetry of the zinc-blende crystal structure, as an applied electric field accelerates the charge carriers through the (Ga,Mn)As, the spins scatter into lower energy spin states generating a spin-accumulation. This is the inverse spin-galvanic effect (ISGE). The spin-Hall effect (SHE) in the semiconductor causes the spins to spatially separate, generating a pure spin-current, J_S , which flows into the Fe layer. Through exchange coupling and a spin-transfer torque, these two effects exert a field-like and anti-damping torque on the magnetisation respectively. An alternating current flowing at the resonance frequency drives FMR.

bulk inversion-asymmetry is demonstrated for the first time. Bilayers of Fe/Ga_{0.97}Mn_{0.03}As, grown by molecular-beam epitaxy (MBE), are measured using spin-orbit FMR.^{23,45} These layers have previously been studied by SQUID and X-ray magnetic circular dichroism (XMCD)¹⁵³ due to reports of proximity exchange polarisation of a (Ga,Mn)As interface layer.¹⁵⁴⁻¹⁵⁶ A magnetic (Ga,Mn)As interface layer of a few monolayers was shown to exist at room temperature, antiferromagnetically coupled to the Fe. Unlike previous SO-FMR measurements of (Ga,Mn)As,^{45,49} to preserve the quality of the interface, the devices studied are not annealed. Consequently the number of compensating interstitial Mn ions is much higher, and the conductivity is comparatively small. Nevertheless, spin-orbit torques with Dresselhaus symmetry, clearly originating from the semiconductor, are shown to drive FMR in the adjacent magnetic Fe layer. These torques are observed alongside the spin-transfer torque arising from the spin-Hall effect in the (Ga,Mn)As layer and are of comparable magnitude.

6.1 SO-FMR in Fe/(Ga,Mn)As bilayers

Wafers of Fe(2 nm)/Ga_{0.97}Mn_{0.03}As(20 nm) and Fe(2 nm)/Ga_{0.97}Mn_{0.03}As(10 nm) were grown by MBE.* $1 \times 10 \mu\text{m}$ bar devices were fabricated by EBL for SO-FMR measurements.[†] The devices were mounted on PCBs as part of a microstrip resonant circuit (see Appendix A) almost identical to the one used for experiments in Chapter 5. In this case, however, a 4-finger in-line capacitor was used to impedance match a typical sample of resistance $\sim 8 \text{ k}\Omega$ at room temperature. A wirebond, attached to the centre of the microstrip resonator allowed the dc voltage, V_{dc} , to be measured across the sample to ground. The inductance of the wirebond, combined with the in-line capacitor forms a bias-tee, separating the alternating and direct currents.

SO-FMR measurements are made at room temperature as described in Chapter 5.1 using the electromagnet system discussed in Chapter 3.2.[‡] A schematic of the device is shown in Figure 6.1. For each FMR sweep, microwave current was pulse modulated at 123.45 Hz in the device as the magnetic field was swept

*The MBE growth was kindly performed by Richard Campion of Nottingham University.

[†]Kamil Olejnik of the Institute of Physics, Prague, kindly performed the sample fabrication.

[‡]Lucy Cunningham kindly assisted with some of these measurements.

from high to low. The resonance was measured in V_{dc} by the AMR rectification effect using a lock-in amplifier. Source microwave powers of 25 dBm were typically used. The microwave frequencies used, typically between 15 and 16.5 GHz, were selected to be close to twice the fundamental frequency of the resonator, to allow high power transmission into the device. For each device, FMR sweeps were made by sweeping the external field every 10 degrees in the plane of the sample. The crystal dependence of the spin-orbit torques was investigated by measuring bars in four different crystal directions (three directions for the 10 nm (Ga,Mn)As wafer).

To determine the size of the AMR (and therefore the efficiency of the resonance detection), the bias-tee was used to make a 2-point resistance measurement of the bar whilst it was rotated through a constant saturating field of 1 T.

6.2 Results and analysis

Each FMR sweep is fitted by a combination of symmetric and antisymmetric Lorentzians as given by equation 3.5 with an additional linear background (see Figure 6.2a). The magnetisation angle dependence of the fitted peaks is studied to determine the symmetries of the current-induced torques. Due to a significant in-plane uniaxial crystal anisotropy in the Fe, the equilibrium magnetisation direction is not the same as the externally applied magnetic field at resonance. The magnetisation angle, uniaxial anisotropy and effective magnetisation are found by self-consistently fitting the Kittel and free energy equations (see Figure 6.2b). From measurements in four crystal directions in each layer, the values of the uniaxial anisotropy and effective magnetisation are found to be $\mu_0 H_U = 0.104 \pm 0.004$ T and $\mu_0 M_{\text{eff}} = 1.90 \pm 0.06$ T in the layer with 10 nm (Ga,Mn)As and $\mu_0 H_U = 0.101 \pm 0.001$ T and $\mu_0 M_{\text{eff}} = 1.85 \pm 0.03$ T in the layer with 20 nm (Ga,Mn)As. In this analysis the gyromagnetic ratio has been assumed to be that of a free electron, $\gamma = 1.76 \times 10^{11}$ radT⁻¹, which is close to the literature value.¹⁵⁷

Empirically it is found that in addition to the expected angle-dependent terms due to the AMR rectification (equations 3.7 and 3.6), small additional terms are needed to completely fit the data. In the case of the antisymmetric coefficients, there is an angle-independent offset as well as a $\sin 2\theta$ term. For the symmetric coefficients this includes a $\sin \theta$ term which may be due to a spin-pumping signal.

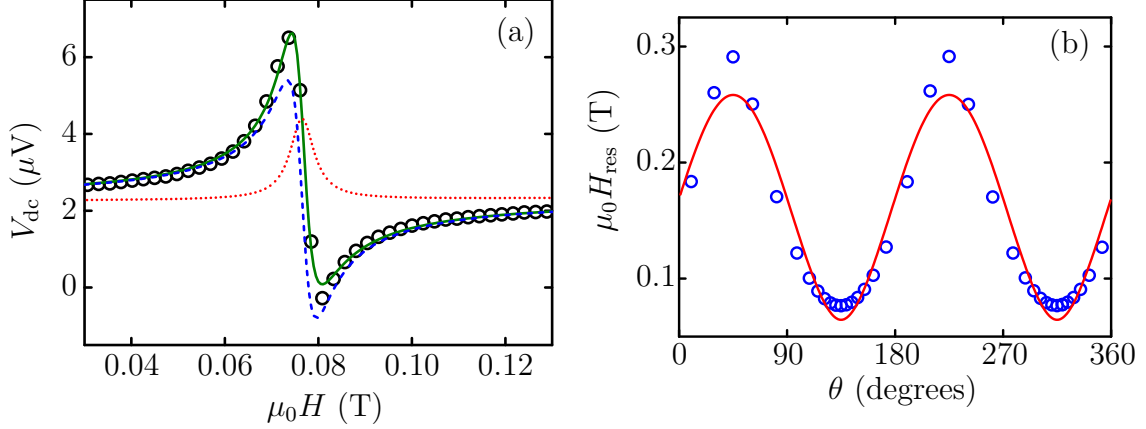


Figure 6.2: (a) Each FMR sweep is fitted by a combination of an antisymmetric (blue dashed line) and a symmetric (red dotted line) Lorentzian with a linear background. (b) For a [010] bar fabricated from the 20 nm layer, the resonant field is plotted as a function of magnetisation angle showing an in-plane uniaxial anisotropy. Both the magnetisation angle and fitted curve are self-consistently fitted to the Kittel and free energy equations.

By fitting these components to V_{asy}/A_{yy} and V_{sym}/A_{yz} (equations 3.7 and 3.6), the symmetries of the torques can be found. In total the fitted components are expressed as

$$\frac{V_{\text{asy}}}{A_{yy}} = C_0 + V_{\text{mix}} (h_y \cos \theta - h_x \sin \theta) \sin 2\theta + C_{\sin 2\theta} \sin 2\theta \quad (6.1)$$

and

$$\frac{V_{\text{sym}}}{A_{yz}} = C_{\sin \theta} \sin \theta + V_{\text{mix}} (h_z^0 + h_z^{\cos \theta} \cos \theta + h_z^{\sin \theta} \sin \theta) \sin 2\theta. \quad (6.2)$$

The fitted angle dependence of the voltages is shown in Figure 6.3 for the layer with 20 nm (Ga,Mn)As. The fitted components for the antisymmetric and symmetric data are shown in Figs. 6.4a and 6.4b respectively.

The antisymmetric components depend on the crystal direction and have mainly the Dresselhaus symmetry ($\mathbf{h}_D \propto (-k_{x'}, k_{y'})$) with a small additional Rashba symmetry component ($\mathbf{h}_R \propto (-k_{y'}, k_{x'})$) as has previously been observed in low temperature measurements of thin-film, annealed (Ga,Mn)As.^{45,49} Here the x' and y' coordinates correspond to the [100] and [010] crystal directions. The symmetric components, which are of comparable magnitude, do not show a significant

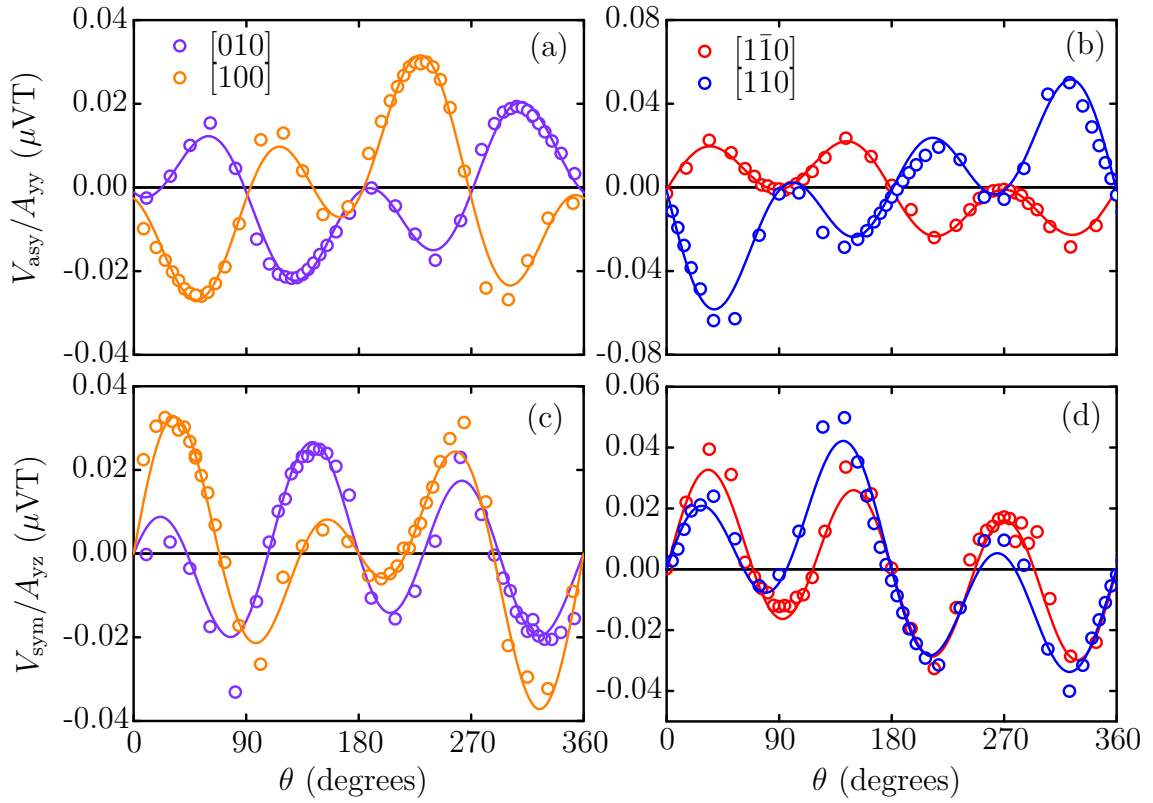


Figure 6.3: (a),(b) The angle dependence of V_{asy}/A_{yy} is fitted by equation 6.1 for devices in each crystal direction (data shown here from 20 nm layer). (c),(d) V_{sym}/A_{yz} from the same devices are fitted with equation 6.2.

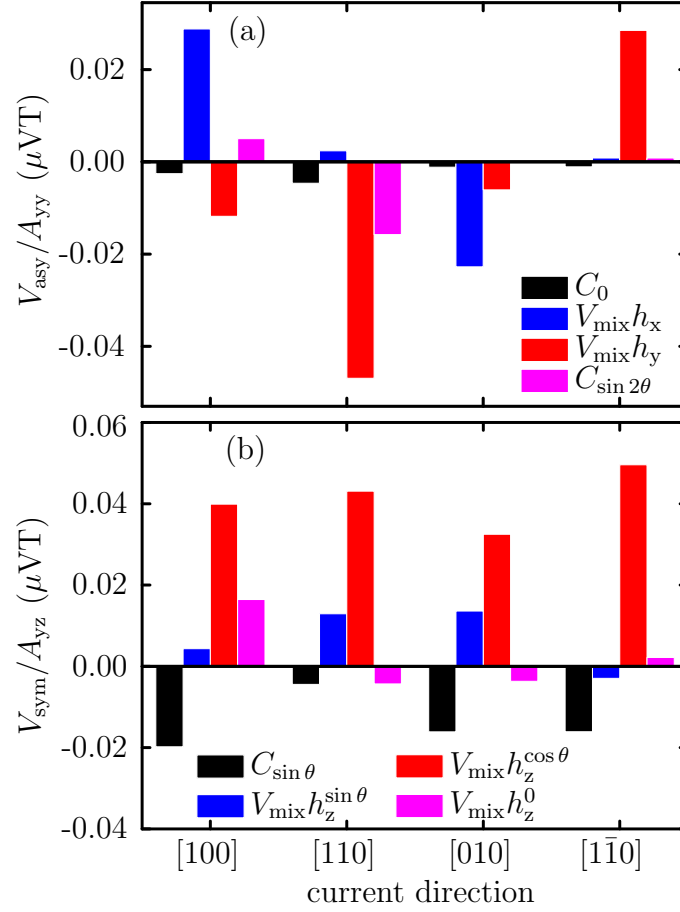


Figure 6.4: (a),(b) Fitted angle-dependent components for V_{asy}/A_{yy} and V_{sym}/A_{yz} for each crystal direction in the 20 nm layer respectively.

variation with crystal direction. The main symmetric component, $h_z^{\cos\theta}$ with a $\cos\theta \sin 2\theta$ symmetry indicates a magnetisation dependent torque. This is the same symmetry that we are familiar with in metal bilayers that is indicative of a spin-Hall effect spin-transfer torque.²³ The independence of this symmetry on crystal direction immediately rules out an anti-damping torque arising from the Dresselhaus spin-orbit fields.

6.3 Calibration of current-induced torques

To calibrate the spin-orbit fields and calculate the spin-Hall angle, both the microwave current in the sample and the AMR need to be measured. Values of the AMR, found from 2-point magnetoresistance measurements, were typically found to be 21 Ω for the layers with 10 nm (Ga,Mn)As and 17 Ω for the 20 nm layers. The current was found using the bolometric heating calibration previously shown in Chapter 5.3. Typically the heating calibration suggests 10 - 30% of the source microwave power is impedance-matched into the sample, resulting in injected microwave currents of the order of 1 mA.

To calibrate the efficiency of the spin-orbit fields, the proportion of current in the (Ga,Mn)As needs to be estimated. Hall bars were fabricated from the 10 nm wafer by photolithography for this purpose. 4-point resistivity measurements were made before and after removal of the Fe and AlO_x capping layers, to estimate the resistivity of the (Ga,Mn)As and Fe. The alumina was removed by a 15 s immersion in 10% HCl solution. The Fe was selectively removed by a 15 s immersion in MF319 developer. The sheet resistance showed a change from 1046 Ω/sq to 9068 Ω/sq after stripping the metal layers, indicating that 12% of the current flows through the 10 nm (Ga,Mn)As layer. The resistivity of the 20 nm layers is assumed to be the same as in the 10 nm layer, giving an equivalent figure of 21%.

The spin-orbit fields were calibrated in each crystal direction for the 20 nm layers. These are shown in Figure 6.5a as well as a vector representation of the fields in Figure 6.5b. In [100] and [010] devices, the Dresselhaus (h_x) and Rashba (h_y) fields are orthogonal and it can be calculated that the Rashba field is 0.37 ± 0.06 the size of the Dresselhaus field. From averaging the fields from each of the crystal directions an estimate of $h_D = 1.6 \pm 1.0 \mu\text{T}/10^6 \text{Acm}^{-2}$ and $h_R = 0.6 \pm 0.4 \mu\text{T}/10^6 \text{Acm}^{-2}$ is found for the efficiency of the Dresselhaus and Rashba

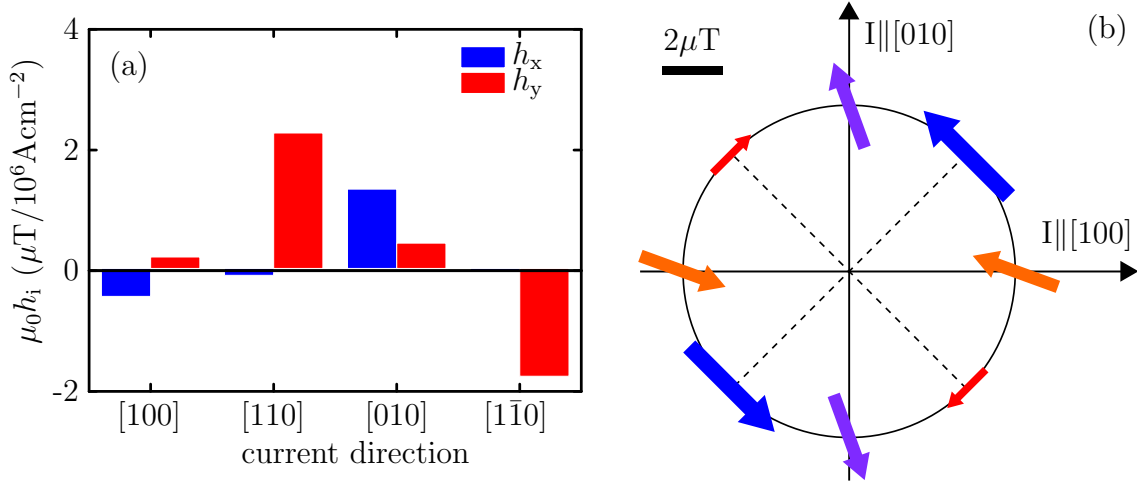


Figure 6.5: (a) Calibrated effective spin orbit fields in each of the measured 20 nm layer crystallographic directions. (b) A vector representation of the combined calibrated Dresselhaus and Rashba fields in the 20 nm layer. The fields are scaled for a current density of 10^6Acm^{-2} .

fields respectively. Here the efficiency is defined as the effective field induced per the current density in the (Ga,Mn)As layer. For an equivalent calibration in three crystal directions of the 10 nm devices, the efficiencies of the fields were estimated to be $h_D = 2.4 \pm 1.5 \mu\text{T}/10^6 \text{Acm}^{-2}$ and $h_R = 1.0 \pm 1.2 \mu\text{T}/10^6 \text{Acm}^{-2}$. The measured parameters used in these calculations are tabulated in Tables 6.1 and 6.2 for the 20 and 10 nm (Ga,Mn)As thicknesses respectively.

6.4 Efficiency of the bulk torques

To compare the efficiency of the Dresselhaus fields measured in the bilayers at room temperature to a bulk value, a $10 \times 100 \mu\text{m}$ bar device was fabricated in the [100] direction by photolithography from the 10 nm layer. The AlO_x and Fe layers were stripped as described above, leaving a device with $\sim 100 \text{k}\Omega$ resistance at room temperature. The device was cooled to below its Curie temperature which, from measurement of the device resistance with temperature (Figure 6.6a), is $\sim 30 \text{K}$. The device was measured in a low temperature vector magnet system at 15 K. The microwave frequency used was close to twice the fundamental frequency of the resonator, 13.95 GHz. The microwave source power was 18.5 dBm.

	Direction			
	[100]	[110]	[010]	[1 $\bar{1}$ 0]
R (Ω)	8460	8264	8419	8496
ΔR (Ω)	17.7	15.4	17.5	16.5
I_0 (mA)	3.5	2.2	1.8	1.8
$\mu_0 H_U$ (T)	0.101	0.101	0.101	0.102
$\mu_0 M_{\text{eff}}$ (T)	1.82	1.83	1.87	1.87
$\mu_0 h_x$ ($\mu\text{T}/10^6 \text{Acm}^{-2}$)	-0.46	-0.11	1.32	-0.05
$\mu_0 h_y$ ($\mu\text{T}/10^6 \text{Acm}^{-2}$)	0.19	2.24	0.42	-1.79
$\mu_0 h_z^{\cos\theta}$ ($\mu\text{T}/10^6 \text{Acm}^{-2}$)	-0.64	-2.06	-1.92	-3.11

Table 6.1: Measurement parameters and calculated effective fields used in the analysis of the Fe(2 nm)/Ga_{0.097}Mn_{0.03}As (20 nm) devices.

	Direction		
	[100]	[010]	[1 $\bar{1}$ 0]
R (Ω)	8907	8695	8805
ΔR (Ω)	23.1	22.9	20
I_0 (mA)	1.43	0.75	4.46
$\mu_0 H_U$ (T)	0.107	0.108	0.098
$\mu_0 M_{\text{eff}}$ (T)	1.95	1.85	1.84
$\mu_0 h_x$ ($\mu\text{T}/10^6 \text{Acm}^{-2}$)	-2.16	3.98	-0.019
$\mu_0 h_y$ ($\mu\text{T}/10^6 \text{Acm}^{-2}$)	0.27	2.37	-0.69
$\mu_0 h_z^{\cos\theta}$ ($\mu\text{T}/10^6 \text{Acm}^{-2}$)	-3.24	-7.62	-1.28

Table 6.2: Measurement parameters and calculated effective fields used in the analysis of the Fe(2 nm)/Ga_{0.097}Mn_{0.03}As (10 nm) devices.

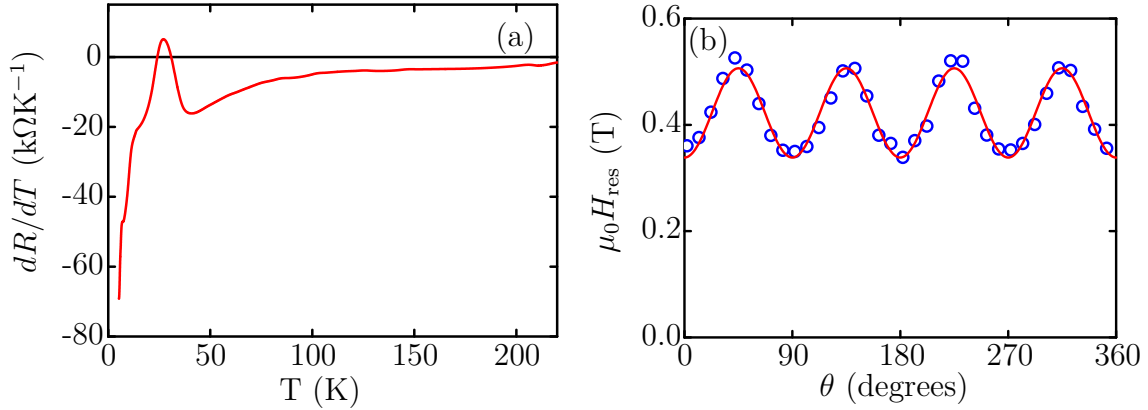


Figure 6.6: (a) Derivative of (Ga,Mn)As resistance with temperature. The peak in derivative gives a Curie temperature of ~ 30 K. (b) Angle dependence of resonant field, for $f = 13.95$ GHz, showing the cubic magnetic anisotropy.

As the (Ga,Mn)As is unannealed and therefore inhomogeneous, the linewidth is very broad (~ 150 mT) compared to the room temperature FMR measurements (~ 3.5 mT) where the precession of the Fe magnetic moments is measured. A typical fitted resonance is shown in Figure 6.7a. The complete removal of the Fe layer can be seen in the change from a uniaxial to a cubic magnetic anisotropy (Figure 6.6b). The angle dependence of $V_{\text{asy}}/A_{\text{asy}}$ and $V_{\text{sym}}/A_{\text{sym}}$ is shown in Figure 6.7b. The angular dependence of the antisymmetric data is fitted by a combination of a $\cos \theta \sin 2\theta$ term, a $\sin \theta \sin 2\theta$ term and a $\sin \theta$ term. In contrast to the bilayer data, the $\cos \theta \sin 2\theta$ term dominates, indicating a h_y effective field mostly exists. This makes interpreting the data difficult. However, there is also a h_x effective field which may correspond to the Dresselhaus spin-orbit field. The current is calibrated using the same heating calibration as before. 0.03% of the microwave source power is estimated to be dissipated in the sample, corresponding to a current of $8.5 \mu\text{A}$ in the device. An estimation of 15 dB loss between the microwave source and sample indicates that $\sim 1\%$ of the incident power is transmitted. This is reasonable given the impedance of the sample (~ 250 k Ω) is far above the matching impedance of the resonator (~ 10 k Ω). An AMR coefficient of $\Delta R = 9000 \Omega$ leads to an estimate for the spin-orbit field efficiency of $h_{\text{D}} = -1.5 \text{ mT}/10^6 \text{ Acm}^{-2}$. Note that this has the opposite sign to the field in the room temperature bilayer and the previous SO-FMR measurements in $\text{Ga}_{0.94}\text{Mn}_{0.06}\text{As}$.⁴⁵

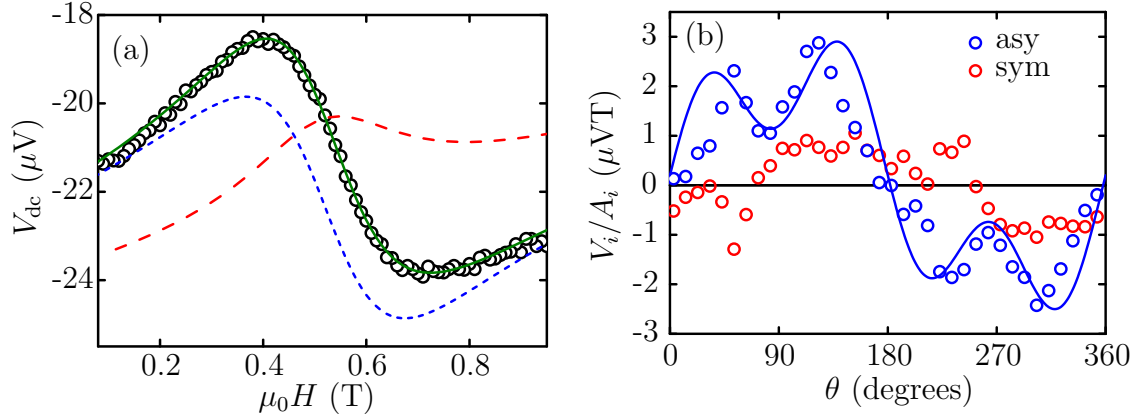


Figure 6.7: (a) A resonance peak in a stripped [100] 20 nm (Ga,Mn)As device measured at 15 K is fitted by a combination of antisymmetric (blue dashed line) and symmetric (red dotted line) Lorentzians with a linear background. (b) The angular dependence of the fitted components in the same device. The antisymmetric dependence is fitted by a $\cos \theta \sin 2\theta$, $\sin \theta \sin 2\theta$ and $\sin \theta$ component.

6.5 Calibration of the spin-Hall angle

The spin-Hall angle of the (Ga,Mn)As layer can be estimated if one assumes that $M_S \approx M_{\text{eff}}$. This is usually a good approximation as long as the demagnetisation field can be treated as that of an infinite plane. The values of $\mu_0 M_{\text{eff}} = 1.85 \pm 0.03$ T measured for these layers is not far from the literature value of 1.7 T for bulk Fe. The spin-Hall angle is then estimated from the calibrated microwave field using equation 5.3 as in metal bilayers,

$$\theta_{\text{SH}} = \frac{2e}{\hbar} \mu_0 M_S d_{\text{Fe}} \frac{h_z^{\cos \theta}}{J_C}, \quad (6.3)$$

where d_{Fe} is the thickness of the Fe layer, $h_z^{\cos \theta}$ is the magnitude of the effective field induced by the spin-Hall effect spin-transfer torque and J_C is the current density in the semiconductor. Note that it has been assumed in this calculation that the thickness of the semiconductor is much thicker than its spin-diffusion length. The experimentally measured values in the 20 nm devices then give a value of $\theta_{\text{SH}} = 0.17 \pm 0.09\%$. From the three calibrated devices in the 10 nm layers, the estimated value is $\theta_{\text{SH}} = 0.20 \pm 0.16\%$.

6.6 Discussion

The observed spin-orbit fields possess the k-linear Dresselhaus symmetry characteristic of the strained zinc-blende lattice of the (III,V) semiconductors. A smaller additional field with Rashba symmetry can also be distinguished from the Dresselhaus symmetry fields in the [100] and [010] current directions, where they are orthogonal. These fields are consistent in symmetry with the fields previously measured in thin-film annealed $\text{Ga}_{0.94}\text{Mn}_{0.06}\text{As}$ devices at low temperatures, but are two orders of magnitude smaller than the $h_{\text{D}} = 180 \mu\text{T}/10^6 \text{Acm}^{-2}$ measured there.⁴⁵ The origin of the Rashba symmetry fields is the same as the uniaxial anisotropy that appears in (Ga,Mn)As, which reduces the symmetry of the zinc-blende crystal. Birowska *et al.* explain this reduction in symmetry by a non-random distribution of Mn ions over cation sites introduced during epitaxial growth.¹⁵⁸ This effect can be parameterised as an effective strain ϵ_{xy} in the lattice.

The field-like nature of these torques indicates that the spin-accumulation induced through the bulk inversion-asymmetry in the semiconductor exerts a torque on the Fe and Mn moments locally through exchange coupling at the interface. This coupling is likely to be strongest in the proximity polarised (Ga,Mn)As layer at the interface where there is both local magnetisation and generation of spin-accumulation. If the coupling can be approximately described as a uniform effective field acting over an effective interface volume, then the effective field acting on the interface moments, $h_{\text{D}}^{\text{int}}$, can be found by the ratio of interface magnetic moments to total magnetic moments,

$$h_{\text{D}}^{\text{int}} = -\frac{V_{\text{tot}}M_{\text{tot}}}{V_{\text{int}}M_{\text{int}}}h_{\text{D}}, \quad (6.4)$$

where M_{tot} and M_{int} are the magnetisations of the total Fe layer and at the interface respectively and V_{tot} and V_{int} are the volumes of the Fe layer and the effective interface volume which experiences the torque.

If one assumes that this interface volume consists solely of the proximity polarised magnetic (Ga,Mn)As layer, then the ratio of moments can be estimated from previous 5 K SQUID measurements of the Fe and (Ga,Mn)As moments. There, the interface thickness was measured as 0.7 nm and the magnetic moments of the 2 nm Fe and 20 nm (Ga,Mn)As layers were $4.5 \times 10^{-8} \text{Am}^2$ and

$0.3 \times 10^{-8} \text{ Am}^2$ respectively.¹⁵³ An estimated ratio of $V_{\text{tot}}M_{\text{tot}}/V_{\text{int}}M_{\text{int}} = 430$ results in an interface field of $h_{\text{D}}^{\text{int}} \sim -0.7 \text{ mT}/10^6 \text{ Acm}^{-2}$. This is around half the size of the bulk effective field found from the low temperature measurement of the stripped $\text{Ga}_{0.97}\text{Mn}_{0.03}\text{As}$. It is surprising that this and the low temperature value are significantly bigger than the fields previously measured in annealed $\text{Ga}_{0.94}\text{Mn}_{0.06}\text{As}$ ($180 \mu\text{T}/10^6 \text{ Acm}^{-2}$), as the lower Mn concentration should result in a smaller lattice growth strain. However, the torques have not previously been measured in unannealed samples and the interstitial Mn content may have a significant effect on the lattice strain and spin-orbit coupling.

The low-temperature measurements of a 10 nm thin-film $(\text{Ga},\text{Mn})\text{As}$ [100] device suggest that, because the sign of the measured h_x field is inverted, the sign of the spin-accumulation induced by the current is inverted with respect to that of thin-film annealed $\text{Ga}_{0.94}\text{Mn}_{0.06}\text{As}$. The spin-accumulation in the itinerant hole population of the $(\text{Ga},\text{Mn})\text{As}$ could exert a torque either through ferromagnetic exchange with the Fe magnetisation at the interface, or with antiferromagnetic exchange with the interfacial Mn magnetisation.^{159,160} The strong antiferromagnetic coupling between the magnetic interfacial $(\text{Ga},\text{Mn})\text{As}$ layer and the Fe magnetisation¹⁵³ (see Figure 6.8) leads to a torque with opposite sign to that in the low-temperature measurements of stripped $(\text{Ga},\text{Mn})\text{As}$.

A torque with anti-damping Dresselhaus symmetry can arise intrinsically due to precession of the spins around the sum of the spin-orbit fields and local magnetisation as they are accelerated by the electric field. However, unlike low-temperature measurements in thin-film annealed $\text{Ga}_{0.94}\text{Mn}_{0.06}\text{As}$,⁴⁹ this symmetry is not seen. The spin-diffusion length and momentum scattering times are likely to be significantly shorter in these unannealed samples due to the higher number of interstitial Mn ions. This may have some effect on the size of this torque. If the effective spin-orbit fields arise mainly due to exchange coupling from spin-accumulation in the non-magnetic part of the semiconductor one would also expect a much smaller intrinsic anti-damping torque.

Alongside the field-like spin-orbit torque there also exists an isotropic anti-damping torque, due to the spin-Hall effect. This different type of torque arises because the spin-Hall effect drives a spin-current into the ferromagnet which exerts a spin-transfer torque.²³ The induced spin-accumulation, in contrast, causes little spin-current to flow, evidenced by the non-crystalline dependence of the

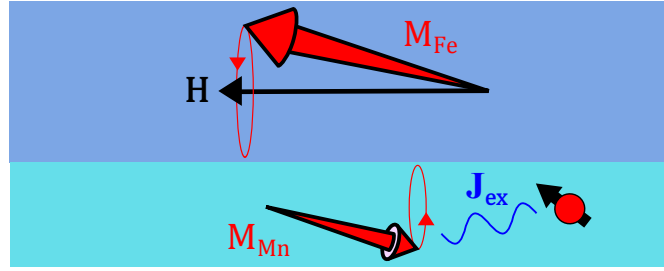


Figure 6.8: The spin-accumulation in the magnetic (Ga,Mn)As interface layer can exert a torque on the local magnetisation through antiferromagnetic exchange coupling. This magnetisation, M_{Mn} , strongly antiferromagnetically coupled to the magnetisation in the much larger Fe layer, M_{Fe} , exerts a torque with opposite sign on M_{Fe} .

anti-damping torque. The spin-Hall angle of 0.2% measured in the unannealed $\text{Ga}_{0.97}\text{Mn}_{0.03}\text{As}$ is close to the value of 0.6% previously measured in p-doped GaAs using a spin-pumping technique.¹⁶¹ In the analysis, perfect transmission of spin-current across the interface was assumed as in the case for metal bilayers. However, in this material there should be a Schottky barrier at the interface which could lead to a significant imaginary part of the spin-mixing conductivity.¹⁶ Therefore, the estimated spin-Hall angle should be seen as a lower bound.

6.7 Conclusions

The current-induced spin-accumulation, which exerts a torque on the local magnetic moments in low-temperature (Ga,Mn)As, also exists in non-magnetic room temperature (Ga,Mn)As. By depositing a layer of Fe on top of the (Ga,Mn)As, the spin-accumulation in the (Ga,Mn)As exerts a torque on the Fe magnetisation through exchange coupling at the interface. It is still an open question as to what extent the proximity polarised layer of (Ga,Mn)As at the interface plays a role in this exchange coupling. Unlike Rashba symmetry torques, which originate from the structural inversion-asymmetry of the interface, these torques, which originate from the bulk inversion-asymmetry of the semiconductor, can be distinguished from torques due to the spin-Hall effect by their dependence on crystal direction. Ferromagnet/semiconductor bilayers are therefore an attractive system in which to unambiguously study the fundamental physics of current-induced torques. Fur-

Conclusions

thermore, this study motivates research into spin-orbit torques in single-layer ferromagnetic metals with bulk inversion-asymmetry, with the aim of creating new spintronic memories.

Chapter 7

Conclusions and outlook

This thesis has presented experimental studies of spin dynamics in two different spin-orbit coupled room temperature ferromagnetic systems: bilayers of Co/Pt and Fe/(Ga,Mn)As. It is instructive to compare the current-induced torques that have been observed in these similar ferromagnet/non-magnet bilayer systems. The current-induced torques in both materials consist of a field-like and an anti-damping term. There is something quite fundamental about this; the field-like and anti-damping torques are the lowest order possible torques which are odd and even functions of magnetisation respectively. Some measurements of metal bilayers now suggest the presence of higher order terms that require the theoretical models of these effects to be refined further.³⁴

In Chapter 5, the measurements of the torques in Co/Pt showed the emergence of a field-like torque in the thinnest ferromagnetic films, consistent with a Rashba field. However, it is not simple to separate from this the field-like component of the SHE-STT which one would also expect to become largest in the thinnest ferromagnets. In contrast, in Chapter 6, the measurements of the spin-orbit torques in Fe/(Ga,Mn)As bilayers showed a field-like torque with a Dresselhaus symmetry originating from the inversion-asymmetry of the zinc blende crystal. This is easily separated from the SHE-STT contribution which has an anti-damping symmetry and is isotropic with respect to the crystal direction. Not only is this the first demonstration of a spin-orbit torque arising from a bulk inversion-asymmetry at room temperature, but the ability to separate the Dresselhaus and SHE-STT contributions makes Fe/(Ga,Mn)As an attractive system in which to study the

spin-orbit torques.

The measurements of Co/Pt in Chapter 5 and the continuing debate amongst the spintronics community about the origins of the torques in metal bilayers demonstrates the difficulty of disentangling the spin-Hall and Rashba effects. Recent measurements of domain wall propagation in these systems also suggest that the Dzyaloshinskii-Moriya interaction^{162,163} (DMI) may also play a role in magnetisation switching with these torques.^{164–166} The DMI is an antisymmetric exchange interaction that can exist when there is spin-orbit coupling and an inversion-asymmetry. This leads to chiral magnetic structures such as conical, helical and skyrmion formations. Micromagnetic simulations suggest that in some metal layers, intermediate helical states can form during current-induced switching due to the DMI at the interface.¹⁶⁷

Spin-orbit torque physics is still in its infancy, but clearly has a role to play in many spintronic systems. An immediate goal, in response to the study of Fe/(Ga,Mn)As in Chapter 6, should be the growth and measurement of the current-induced torques in a room temperature ferromagnet with a BIA. The experimental developments regarding the DMI in metal layers suggests that new physics involving the spin-orbit torques could also be found in chiral magnetic structures with a bulk DMI, such as MnSi.¹⁶⁸ Another set of interesting materials which are likely to be explored are topological insulators (TI). There is already one report of large current-induced torques, attributed to the spin-splitting of the surface TI states in Bi₂Se₃/permalloy bilayers.¹⁶⁹ Whilst the fundamental physics in the metallic bilayer structures is complicated, research in these materials is likely to intensify due to the immediate potential for commercialisation of spintronic memories.

Appendices

Appendix A

Impedance matching

The high-frequency experiments described in Chapter 4 were performed without impedance matching. That is to say, the characteristic impedance of the transmission line, $Z_0 = 50\Omega$, is not equal to the impedance of the load, Z_L . At the impedance-mismatch, the reflection coefficient is given by

$$\Gamma = \frac{Z_L - Z_0}{Z_L + Z_0}. \quad (\text{A.1})$$

For the $\sim 2\text{ k}\Omega$ samples typically measured, $\sim 90\%$ of the microwave power is reflected from the sample. This is undesirable, firstly because microwave sources with high power outputs must be used to compensate for the low transmission and secondly, because we cannot directly calibrate the amount of microwave power in the sample. To overcome this, a matching network must be used. One way to achieve this is by using a microstrip resonator circuit.

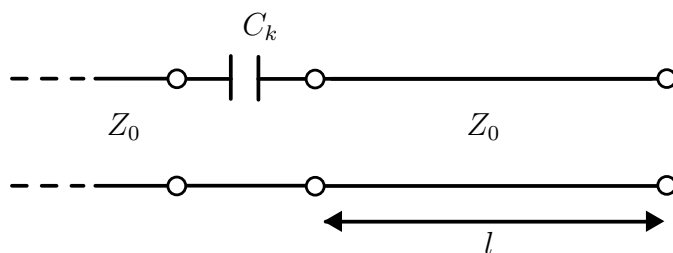


Figure A.1: Schematic representation of a gap-coupled microstrip resonator of length l .

A.1 Microstrip resonators

The unloaded resonator consists of an unterminated microstrip transmission line separated from the incident transmission line by an in-line gap-coupled capacitor. This can be represented schematically as shown in Figure A.1.

For a lossless, loaded transmission line, the input impedance at a distance l from the load is given by¹⁷⁰

$$Z_{in} = Z_0 \frac{Z_L + jZ_0 \tan(\beta l)}{Z_0 + jZ_L \tan(\beta l)}, \quad (\text{A.2})$$

where $\beta = \frac{\omega}{v_p}$, and v_p is the phase velocity of the electromagnetic waves on the transmission line. For a lossless unterminated microstrip resonator of length l , the input impedance reduces to

$$Z_{in} = -jZ_0 \cot(\beta l). \quad (\text{A.3})$$

Combined in series with the gap-coupled capacitor this gives a total impedance of

$$Z = -j \frac{1}{\omega C_k} - jZ_0 \cot(\beta l). \quad (\text{A.4})$$

For a real resonator, there will also be some real impedance due to losses. Given this, it can be seen that the coefficient of reflected power, $|\Gamma|^2$, is minimised when the imaginary part of the impedance goes to zero, i.e. when $\cot(\beta l) = \frac{1}{Z_0 \omega C_k}$. For weak capacitive coupling, $Z_0 \omega C_k \ll 1$, and therefore the first harmonic resonance (the fundamental) occurs at $\lambda \approx 2l$. Hence this type of resonator is known as a **half-wavelength resonator**.

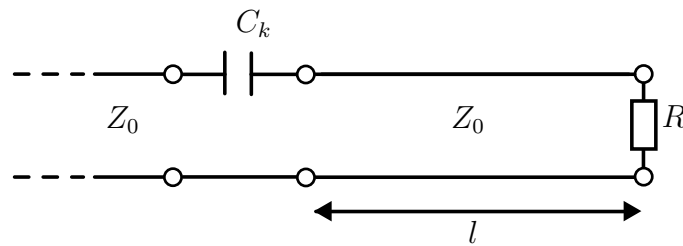


Figure A.2: Schematic representation of a loaded gap-coupled microstrip resonator.

A.1.1 Loaded half-wavelength resonator

Now consider the case where the resonator is loaded, as in Figure A.2. The microstrip resonator is now terminated by a real impedance, R , and the total resonator impedance becomes

$$Z = -j\frac{1}{\omega C_k} + Z_0 \frac{R + jZ_0 \tan(\beta l)}{Z_0 + jR \tan(\beta l)}. \quad (\text{A.5})$$

If R is large, we can look for solutions for the resonant frequency close to the unloaded solution of $\omega_0 = \frac{\pi v_p}{l}$. Expressing the solution as $\omega_1 = \omega_0 + \delta\omega$ we can expand to first order $\tan(\beta l) \approx \pi \frac{\delta\omega}{\omega_0}$. By setting the imaginary part of the impedance to zero, and assuming $R \gg \frac{1}{\omega_0 C_k}$ it can be seen that the resonance occurs when

$$\frac{\delta\omega}{\omega_0} = -\frac{\omega_0 C_k Z_0}{\pi}. \quad (\text{A.6})$$

From substituting this frequency shift into equation A.5, the impedance at resonance becomes¹⁴⁵

$$Z(\omega_1) \approx \frac{1}{\omega_1^2 C_k^2 R}. \quad (\text{A.7})$$

The effect of the coupling capacitor is to invert the real impedance of the load on resonance. By selecting a suitable coupling capacitor so that $Z(\omega_1) = 50 \Omega$, the transmission line and sample can be matched on resonance.

A.2 Measurements of half-wavelength resonators

Half-wavelength microstrip resonators have previously been used to match $\sim 10 \text{ k}\Omega$ (Ga,Mn)As samples for current-induced FMR experiments.¹⁴⁵ The resonators used a 4-finger interdigitated capacitor. FMR can be electrically detected with a wirebond bias-tee. A wirebond attached to the centre of the resonator does not disturb the standing wave in the resonator because there is a node of microwave voltage. The inductance of the wirebond acts as a high-pass filter, only allowing low-frequency signals through. V_{dc} can then be measured from the wirebond to ground.

Modified boards with 8-finger capacitors were used to try to match $\sim 2 \text{ k}\Omega$ Co/Pt samples. The resonance in reflected power is measured by using a direc-

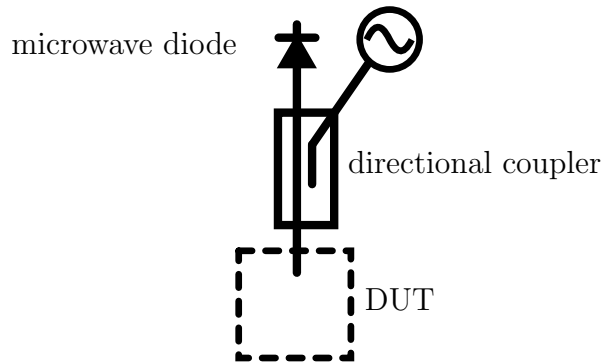


Figure A.3: Measuring reflected power from a device under test (DUT). The 10 dB directional coupler couples 10% of the power from the signal generator into the DUT. The reflected power is mostly coupled into the microwave diode, and the voltage generated across the diode can be calibrated to measure the reflected power.

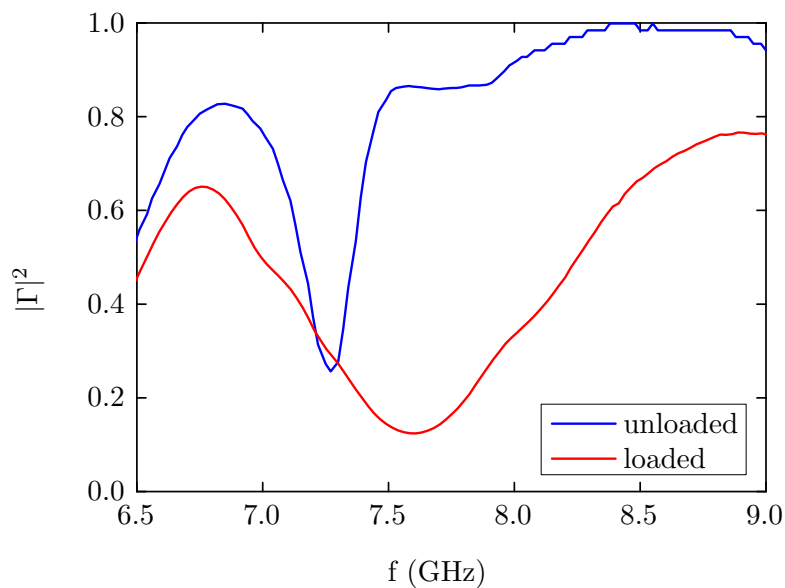


Figure A.4: Dependence of reflected power on frequency for an unloaded and loaded half-wavelength microstrip resonator with an 8-finger capacitor. The loaded resonator is better matched, and has a larger half-power bandwidth at resonance than the unloaded resonance. The unloaded resonator still shows significant power absorption at resonance due to losses. The losses may be through dissipation in the substrate or radiation from a poorly sealed enclosure. Notice also the increase in resonant frequency upon loading, the opposite of what is predicted by equation A.6.

tional coupler and microwave diode, configured as shown in Figure A.3. The resonance in reflected power is shown for the loaded and unloaded cases in Figure A.4. The loading increases the matching on resonance and increases the half-power bandwidth, both indicating good matching.

The resonators have to be enclosed in a copper box to reduce radiation losses and microwave noise coupling into the resonators. The largest dimensions of the boxes are 27 mm x 18 mm. In the vector cryostat system, used for measurements in Chapter 4, this can be easily positioned in the centre of the field. However, for the room-temperature electromagnet system, discussed in Chapter 5, the resonators have to be re-designed as discussed below.

A.3 Compact microstrip resonators for FMR

To achieve magnetic fields approaching 1 T, the pole spacing of the electromagnet described in Chapter 3.2 has to be reduced to ~ 32 mm. To allow the PCB to be rotated through any angle within the pole spacing, this restricts the size of the PCB to a square of 20 mm x 20 mm. Furthermore, the sample should be mounted in the centre of the board to allow it to rotate in a uniform field. This heavily restricts the design of the resonator as for a typical FMR frequency of 7 GHz, the corresponding half-wavelength is ~ 14 mm on a low-loss dielectric substrate of $\epsilon_r \sim 2$. The resonator length could be reduced by using a dielectric substrate with higher ϵ_r , but the resonator would be more lossy. Possible implementations are discussed below.

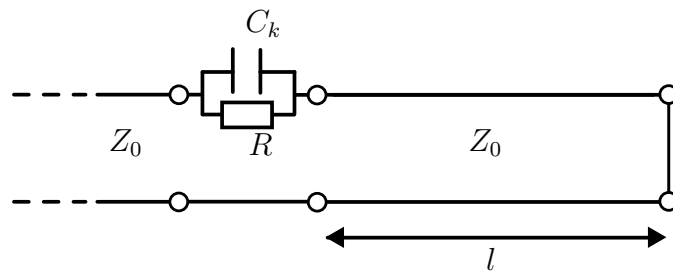


Figure A.5: Schematic representation of the shunted quarter-wavelength microstrip resonator.

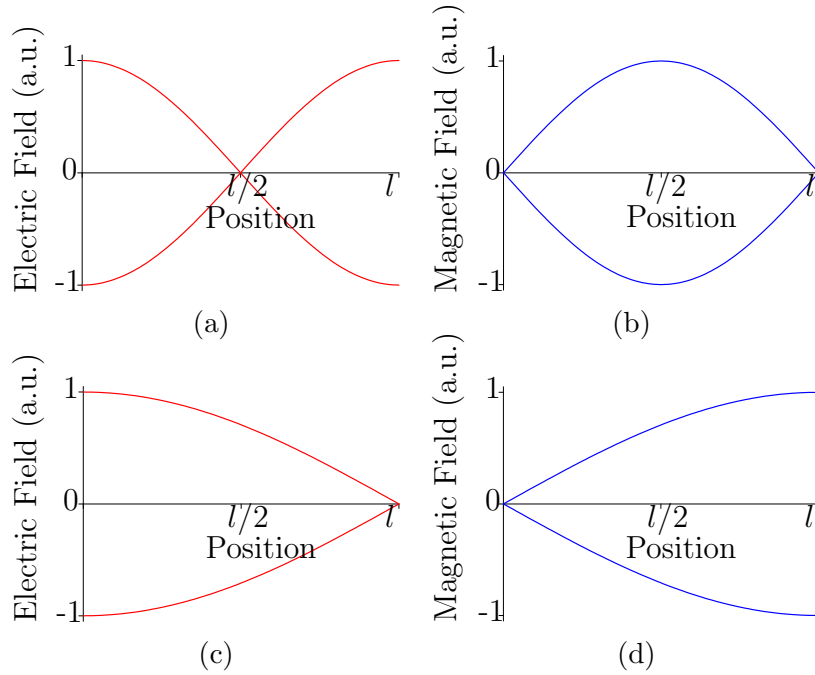


Figure A.6: (a),(b) Amplitude of the electric and magnetic field standing waves in a half-wavelength resonator of length l . (c),(d) Equivalent standing waves in a quarter-wavelength resonator.

A.3.1 Shunted quarter-wavelength resonators

A quarter-wavelength resonator, as the name suggests, has its first harmonic mode when $l = \lambda/4$. This allows a more compact resonator. To create the mode, the resonator is shorted at the free end, creating a node of electric field. The standing waves in a half- and quarter-wavelength resonator are shown in Figure A.6. By setting $R = 0$ in equation A.5, the expression for the impedance of the unloaded resonator becomes

$$Z = -j \frac{1}{\omega C_k} + j Z_0 \tan(\beta l), \quad (\text{A.8})$$

and it can be seen for weak coupling that the first harmonic resonance occurs at $\lambda = 4l$.

The resonator cannot be loaded in the same way as the half-wavelength resonator, as the resonator is already terminated by a short. Instead, the resistor can be used to short the coupling capacitor. Figure A.5 shows a schematic of the

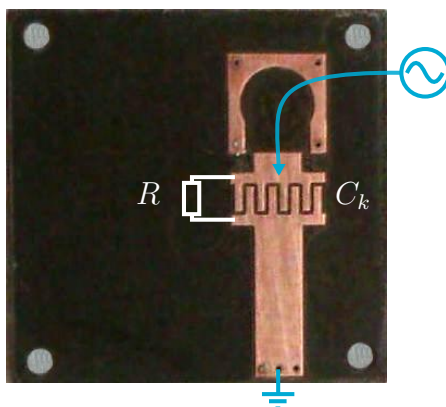


Figure A.7: Photograph of quarter wavelength resonator. The microwave power is coupled onto the board via an SMP connector (not shown). The microstrip end is grounded with conductive epoxy filled via-holes to the ground plane. When loaded, the sample is attached with wirebonds, shunting the interdigitated coupling capacitor.

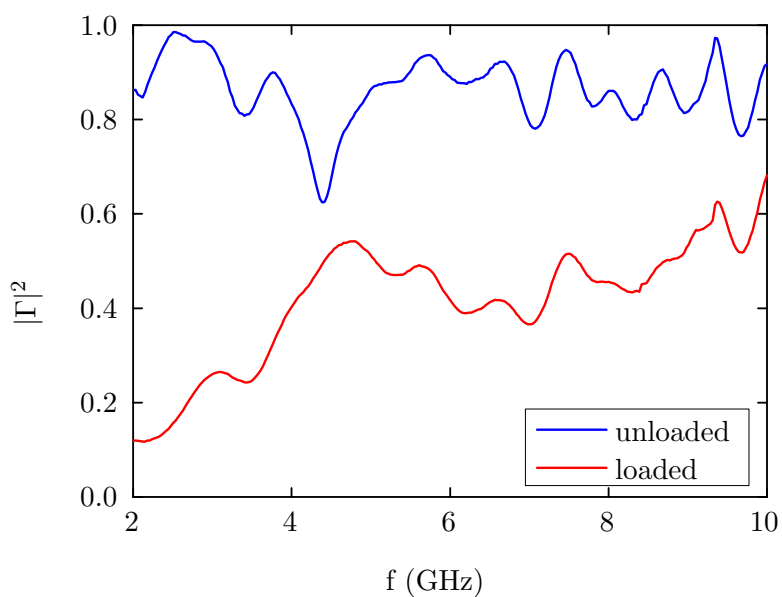


Figure A.8: Dependence of reflected power on frequency for an unloaded and shunted quarter-wavelength resonator. The unloaded resonator shows a small resonance at ~ 4.5 GHz. The loaded resonator shows no resonance, but a broadband matching which is most significant at low frequency.

resonator. In this case the loaded impedance becomes

$$Z = \frac{R}{1 + j\omega C_k R} + jZ_0 \tan(\beta l). \quad (\text{A.9})$$

Solving in a similar way to equation A.5, looking for solutions close to $\omega_0 = \frac{\pi v_p}{2l}$, the shift in resonant frequency becomes

$$\frac{\delta\omega}{\omega_0} = -\frac{2Z_0(1 + \omega_0^2 C_k^2 R^2)}{\pi\omega_0 C_k R^2}, \quad (\text{A.10})$$

and the impedance at resonance becomes

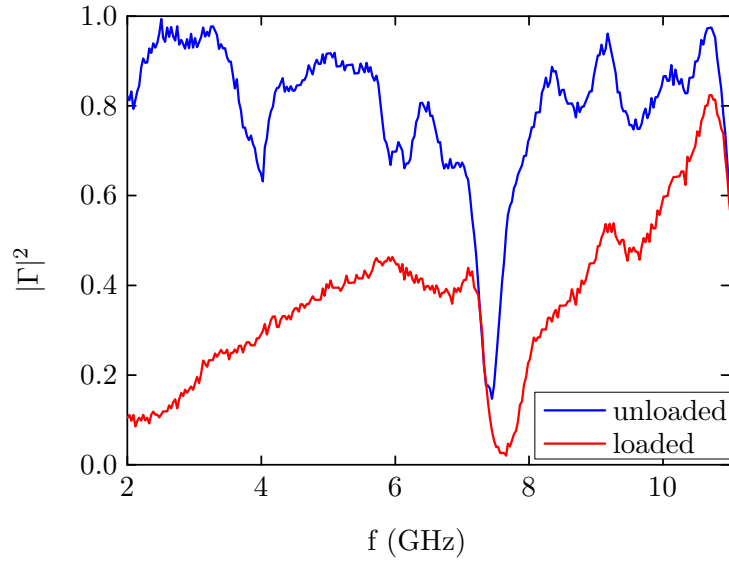
$$Z(\omega_1) \approx \frac{1}{\omega_1^2 C_k^2 R}, \quad (\text{A.11})$$

where it has been assumed that $\omega_1 C_k R \gg 1$. Notice that this impedance is identical to the result obtained when the resistor is used to terminate a half-wavelength resonator.

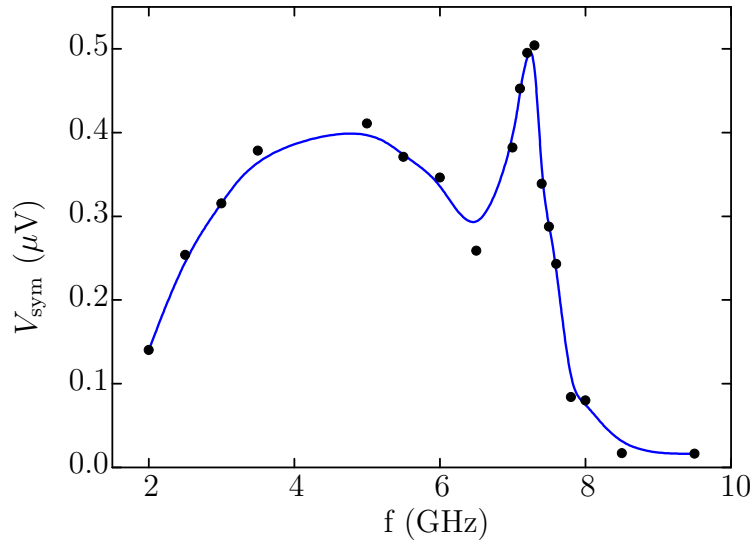
To test the performance of this resonator design, resonator PCBs were fabricated from copper-clad, 0.8 mm thick dielectric with constant $\epsilon = 2.2$ (Rogers corp. Duroid 5880). A photograph of the PCB is shown in Figure A.7. Via holes, filled with conductive epoxy resin, were used to short the microstrip to the ground plane at the end of the resonator. The resonator length is 8 mm, and an 8-finger capacitor was used to try to match a ~ 2 k Ω sample. FMR can be electrically detected with this design by measuring V_{dc} from the microwave line (with a bias-tee component) to ground.

The frequency dependence of the reflected power is shown in Figure A.8. In the unloaded case, a resonance can be observed just below 5 GHz. However, in the loaded case there is no clear transmission peak, but rather a broadband transmission which is largest at low frequency.

To try to understand the behaviour due to the shunting resistor, the half-wavelength resonator used in Appendix A.2 was measured in the shunted configuration. The frequency dependence of the reflected power is shown in Figure A.9a. Again, the same low-frequency broadband transmission is observed, but also a resonance peak at around the same frequency as the unloaded peak. Clearly then, this low frequency transmission is independent of the predicted resonance.



(a) Dependence of reflected power on frequency for an unloaded and shunted half-wavelength resonator.



(b) Dependence of FMR V_{sym} on frequency for the same shunted half-wavelength resonator.

Figure A.9: (a) Unlike the quarter wavelength resonator, the loaded resonator shows the predicted resonance at nearly the same frequency as the unloaded resonator. However, like the quarter wavelength resonator, there is a broadband matching which is most significant at low frequency. (b) V_{sym} is a measure of the power dissipated in the sample. The narrow peak corresponds to the predicted half-wavelength resonance as seen also in the unloaded resonator. However there is also a much broader peak at ~ 4.5 GHz which is not well understood, but must correspond to a different resonant mode.

A direct measure of the power dissipated in the sample is given by the size of the FMR resonance, as $V_{dc} \propto I_{mw}^2$. For an in-plane angle of 45° , FMR is electrically measured for a set of frequencies in a Co(1 nm)/Pt(3 nm) sample. The symmetric lorentzian peak height is plotted against frequency in Figure A.9. There are clearly two peaks, the narrower peak corresponding to the predicted microstrip resonance at ~ 7.5 GHz and the broader peak corresponding to a resonance mode that was not predicted.

Although this resonator design may provide good broadband matching, it would be difficult to use it to calibrate the current in the matched sample as the mechanism for the broad resonance is not understood. A different design will be considered below.

A.3.2 Inverted half-wavelength resonators

A better, but perhaps unobvious, solution is to attach the sample to the resonator at the same end as the coupling capacitor. As the electric fields in the resonator should be nearly symmetric in the weak-coupling limit (see Figure A.6), the sample should experience similar electric fields when attached at either end. In effect, this is the same as a half-wavelength resonator, but with the microwave power coupled in from the same end as the terminating resistor. A schematic representation is shown in Figure A.10. This inverted resonator design has a smaller footprint than the non-inverted design, because the sample is easily arranged close to the centre of the board. A curvature can also be added to the resonator to save space. The impedance of a curved microstrip will not differ significantly from a straight microstrip as long as the radius of the curve is approximately greater than three times the strip width.¹⁷¹

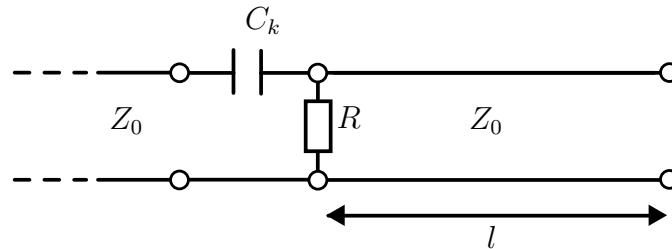


Figure A.10: Schematic representation of the inverted half-wavelength microstrip resonator.

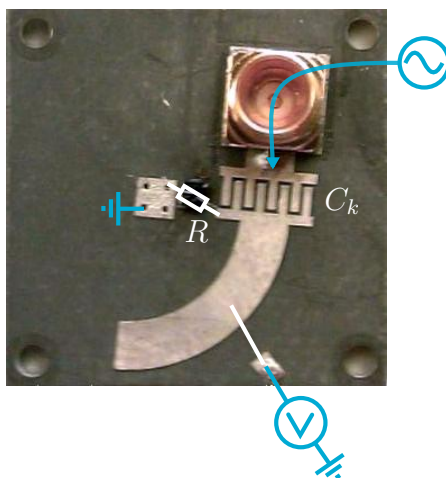


Figure A.11: Photograph of the inverted half-wavelength microstrip resonator. The microwave power is coupled onto the board via a surface-mounted SMP connector. The sample is mounted on the centre of the board and is wirebonded to the end of the resonator and a ground pad. The dc voltage across the sample can be measured with a wirebond bias-tee which is attached to the centre of the resonator.

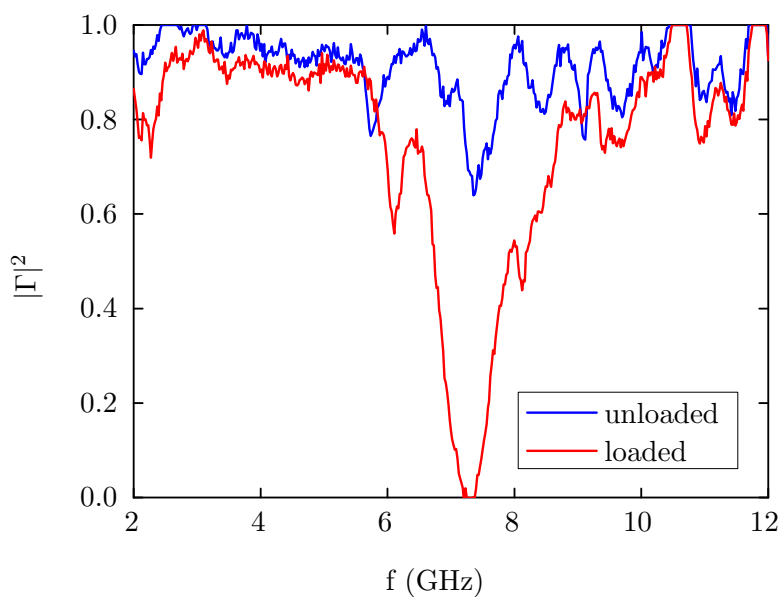


Figure A.12: Dependence of reflected power on frequency for an unloaded and loaded inverted half-wavelength microstrip resonator. The loaded resonator has almost perfect matching for a $\sim 2 \text{ k}\Omega$ sample.

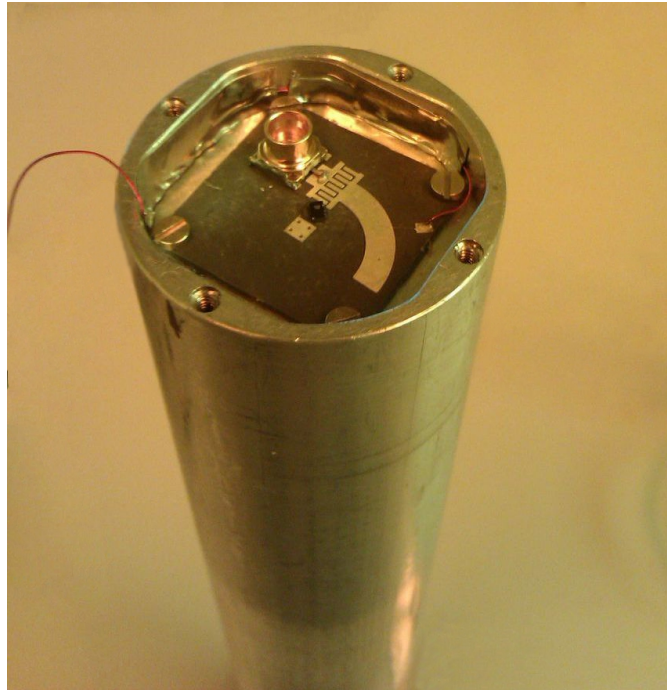


Figure A.13: Inverted half-wavelength resonator mounted on probe with sample and bias-tee connection. The compact design allows a small electromagnet pole separation, allowing fields of up to 1 T to be generated. The bias-tee wire is shielded with aluminium tape to reduce coupling between the wire and the resonator.

The design, a photograph of which is shown in Figure A.11, is fabricated from the same substrate as the the quarter-wavelength resonator design. The resonator length is approximately 11 mm.

The frequency dependence of the reflected power is shown in Figure A.12. The loaded resonator shows very little reflected power at resonance, and a broader resonance than the unloaded resonator, indicating excellent impedance matching.

The resonator PCB is shown mounted in the probe in Figure A.13. This resonator design gives good impedance matching to a sample of $\sim 2 \text{ k}\Omega$ whilst allowing the sample to be uniformly rotated through a magnetic field of up to 1 T. This resonator can be adapted for samples with larger resistance by reducing the interdigitated capacitance. The wirebond bias-tee allows the dc voltage across the sample to be measured while microwave power induces FMR.

Discussed below is how the reflection characteristics of the resonator could be used to calibrate the microwave current in the samples.

A.4 Q factor calibration

To calibrate the amount of microwave current in the devices measured, the amount of power dissipated through other losses must be taken into account. First the simple case of a series resonator will be considered.

A.4.1 Series resonator

A series resonator consists of a resistor, inductor and capacitor in series. A schematic is shown in Figure A.14. The impedance of the resonator is formulated as

$$Z(\omega) = R + j\left(\omega L - \frac{1}{\omega C}\right). \quad (\text{A.12})$$

A resonance must occur when the imaginary part of the impedance goes to zero. i.e. $\omega_0 = \frac{1}{\sqrt{LC}}$. Therefore close to resonance the impedance becomes

$$Z(\omega) = R + j2L\Delta\omega. \quad (\text{A.13})$$

The quality factor, Q , of the resonator is defined as

$$Q = \omega \frac{\text{average energy stored}}{\text{rate of energy loss}}. \quad (\text{A.14})$$

For a series resonator the average dissipated power is given by $P_{loss} = \frac{1}{2}|I|^2 R$, and the average energy stored in the electric and magnetic fields as $E_e = \frac{1}{4}|I|^2 \frac{1}{\omega^2 C}$ and $E_m = \frac{1}{4}|I|^2 L$ respectively. On resonance, $E_e = E_m$ and the Q factor is given by

$$Q = \omega_0 \frac{L}{R}, \quad (\text{A.15})$$

and so it can be written generally for a series resonator that

$$Z(\omega) = R(1 + j2Q \frac{\Delta\omega}{\omega_0}). \quad (\text{A.16})$$

Usefully, the average real power delivered to the resonator, $P_{in} = \frac{1}{2}\Re\{VI^*\} = \frac{1}{2}R|\frac{V}{Z}|^2$, is reduced by half when $2Q\frac{\Delta\omega}{\omega_0} = 1$ and so Q can also be defined using the half-power bandwidth as

$$Q = \frac{\omega_0}{\Delta\omega_{FWHM}}. \quad (\text{A.17})$$

However, this is not a complete picture, because this analysis has ignored dissipation from the external network connected to the resonator.

A.4.2 External coupling

Standard coaxial cables have a characteristic impedance of $Z_0 = 50 \Omega$. A microwave source delivering power to the cable will have 50Ω of internal resistance so that it is matched to the cable. When considering where the microwave current is dissipated, as well as the internal Q factor of the network being probed, the

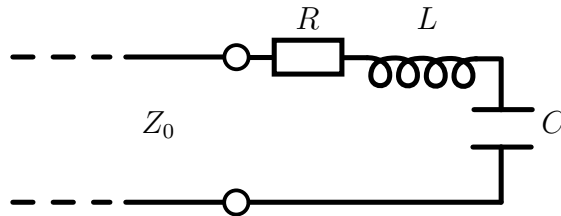


Figure A.14: Schematic representation of a transmission line series resonator.

external Q factor due to the resistance of the source must be considered. For a series resonator, the external and internal resistance add in series, and so from equation A.15 the Q factors add reciprocally to give a total Q factor,

$$\frac{1}{Q_{total}} = \frac{R_{int} + Z_0}{\omega_0 L} = \frac{1}{Q_{int}} + \frac{1}{Q_{ext}}. \quad (\text{A.18})$$

When the resonator is impedance matched to the external network, $Q_{int} = Q_{ext}$. If we introduce a coupling factor,

$$g = \frac{Z_0}{R_{int}} \equiv \frac{Q_{int}}{Q_{ext}}, \quad (\text{A.19})$$

then there are three general cases for coupling to the external network:¹⁷⁰

$$\begin{aligned} g < 1 &: \text{undercoupled to the external network.} \\ g = 1 &: \text{critically coupled to the external network.} \\ g > 1 &: \text{overcoupled to the external network.} \end{aligned} \quad (\text{A.20})$$

With the external network connected, $Q_{total} = \frac{\omega_0}{\Delta\omega_{FWHM}}$, and we can rewrite equation A.17 as

$$Q_{int} = \frac{\omega_0}{\Delta\omega_{FWHM}}(1 + g). \quad (\text{A.21})$$

It is worth considering what effect the coupling has on the reflected signal as experimentally this can be measured relatively easily with a microwave mixer component as shown in Figure A.15. From equation A.1, the coefficient of the reflected power becomes

$$|\Gamma|^2 = \frac{4Q_{int}^2 \left(\frac{\Delta\omega}{\omega_0}\right)^2 + (1 - g)^2}{4Q_{int}^2 \left(\frac{\Delta\omega}{\omega_0}\right)^2 + (1 + g)^2}, \quad (\text{A.22})$$

and it is simple to see at resonance that this becomes

$$|\Gamma_0|^2 = \left(\frac{1 - g}{1 + g}\right)^2. \quad (\text{A.23})$$

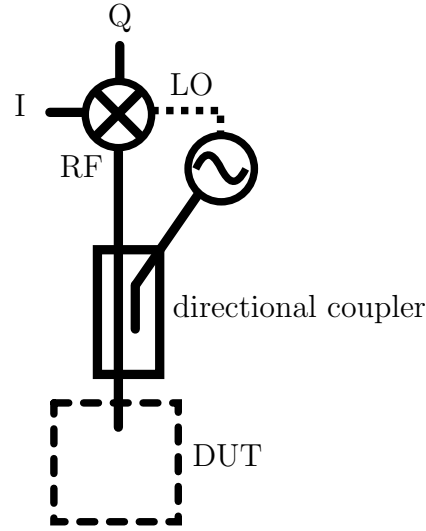


Figure A.15: Measuring the reflected signal from a device under test (DUT). The 10 dB directional coupler couples $\sim 10\%$ of the power from the signal generator into the DUT. The reflected signal is mostly coupled into the RF port of the mixer. When the signal at the rf port is mixed with the reference signal at the local oscillator (LO) port, the in phase (I) and quadrature (Q) components of the reflected signal can be extracted.

There is perfect transmission at resonance when the resonator is critically coupled, but at large over- or under-coupling there is much weaker transmission and the Q factor is much more difficult to measure from the half-power bandwidth. It is interesting to also consider how the phase of the reflected signal around the resonance depends on the coupling:

$$\tan \phi = \frac{4gQ_{int} \frac{\Delta\omega}{\omega_0}}{(1 - g^2) + 4Q_{int}^2 \left(\frac{\Delta\omega}{\omega_0}\right)^2}. \quad (\text{A.24})$$

This has the form of an antisymmetric Lorentzian peak. The width of the peak goes as $(1 - g^2)/Q_{int}^2$ and the height as $1/Q_{ext}$. These results in themselves are experimentally not particularly useful, as the expression is only valid for small $\Delta\omega$. However, the gradient of the phase at resonance is exactly given by

$$\left. \frac{\partial \phi}{\partial \omega} \right|_{\omega_0} = \frac{4Q_{int}}{\omega_0} \frac{g}{(1 - g^2)}, \quad (\text{A.25})$$

which diverges to $\pm\infty$ at critical coupling.

These results are also applicable to the microstrip resonators, as will be shown below.

A.4.3 Calibration using half-wavelength microstrip resonators

Close to resonance, any resonator looks like a series or parallel RLC circuit in the simple harmonic limit. The reactance of the resonator looks capacitive below and inductive above the resonant frequency if it behaves as a series resonator. The opposite is true if it behaves as a parallel resonator. For the half-wavelength resonator shown in Appendix A.1.1, without the coupling capacitor it is a simple parallel resonator. However the effect of the coupling capacitor at resonance is to make it look series.

Performing a simple Taylor expansion of the impedance given by equation A.5 around the resonance, in the simple harmonic limit the impedance is approximately

$$Z(\omega) \approx \frac{1}{\omega_1^2 C_k^2 R} + j \frac{\pi}{\omega_1^3 C_k^2 Z_0} \Delta\omega. \quad (\text{A.26})$$

Using equations A.15 and A.13, this result leads to an expression for Q_{int} ,

$$Q_{int} = \frac{\pi R}{2Z_0}, \quad (\text{A.27})$$

which is approximately the ratio of the load resistor to the characteristic impedance of the microstrip.

Because the impedance can be described perfectly by an equivalent series RLC circuit at resonance, the results derived in equations A.21, A.23 and A.25 can be used to determine g and Q_{int} from the reflected signal for the microstrip resonators.

Finally, when trying to determine to calibrate the current dissipated in the sample, one must also consider the proportion of energy stored in the resonator dissipated through losses. An unloaded, low-loss microstrip resonator can be described by an equivalent parallel RLC circuit, where the resistance, R_{loss} is the effective loss resistance. When the resonator is loaded, the loss resistance adds in parallel with the load resistance. From equation A.27, Q_{int} can then be written as

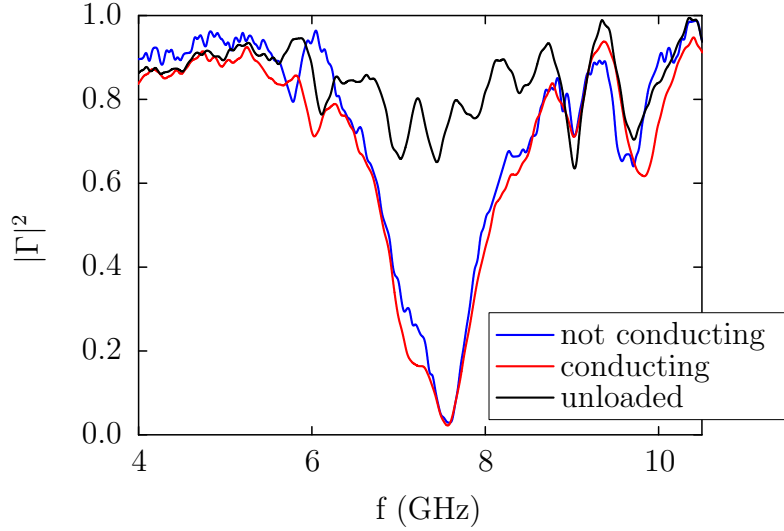


Figure A.16: Dependence of reflected power on frequency for a half-wavelength microstrip resonator. When the sample is unloaded the resonator is unmatched. When the resonator is loaded with a Co/Pt sample, nearly all of the power is absorbed on resonance, indicating excellent matching. However when the same sample is broken, leaving only unconnected bond-pads, the absorption is almost identical to the conducting sample. This strongly suggests that most of the matched power is dissipated in the substrate and not the metal.

$$\frac{1}{Q_{int}} = \frac{1}{Q_{load}} + \frac{1}{Q_{loss}}. \quad (\text{A.28})$$

By measuring Q_{int} in the unloaded and loaded cases, the contributions from the loss and the load are separated.

A.5 Effects of sample substrate

So far the effects of loss have been considered by comparing the absorption and Q factor of the resonance with and without loading from the sample. Therefore, the losses from the microstrip and substrate have been taken into account. However, one additional detail is the loss from the sample substrate. This is easy to neglect but can have a dramatic impact on the absorption by the sample. The Co/Pt samples used to test these resonators were sputtered onto thermally oxidised Si substrates. These are fully insulating when measuring dc transport properties.

When a sample is destroyed by passing very high currents, the bond pads remain, connected by the substrate. The frequency dependence of the reflected power was measured for a typical Co/Pt sample before and after destruction (see Figure A.16). Compared to the unloaded resonator, when loaded, nearly all the power was absorbed on resonance, indicating the sample was matched. However, after destruction the reflected power was almost indistinguishable, indicating that most of the power was not dissipated by the metal layers, but by the sample substrate. The origin of this loss cannot be precisely determined, but a strong possibility is that the thermally oxidised Si substrate forms a 2D electron gas (2DEG) with the unoxidised Si below. At high frequencies, the microwave currents capacitively couple to the 2DEG which acts as a ground, shorting the metal layers above. The severe loss in these samples may explain the unexpected behaviour of the shunted quarter wavelength resonators in Appendix A.3.1. This loss in the sample prevents the matching network from being used to calibrate the current dissipated in the metal of these Co/Pt samples.

A.6 Conclusions

The microstrip resonators described in this appendix have allowed impedance matching of $\sim k\Omega$ samples for SO-FMR. This provides increased detection sensitivity, improving the signal to noise ratio. Despite the failure of the microstrip resonators to allow a calibration of the microwave current in the Co/Pt samples studied in this thesis, the resonators described in this appendix should allow calibration of samples which do not suffer the same substrate loss. This will be important for future SO-FMR measurements which can not be calibrated with a bolometric technique. Furthermore, the analytical approach described here for calculating the resonance and matching conditions of microstrip resonators can easily be extended to new microstrip networks.

Bibliography

- [1] Wolf, S. A., Awschalom, D. D., Buhrman, R. A., Daughton, J. M., Von Molnar, S., Roukes, M. L., Chtchelkanova, A. Y., and Treger, D. M. *Science* **294**(5546), 1488–1495 (2001).
- [2] Awschalom, D. D., Bassett, L. C., Dzurak, A. S., Hu, E. L., and Petta, J. R. *Science* **339**(6124), 1174–1179 (2013).
- [3] Carus, T. L. and Sisson, C. H. *De Rerum Natura*. Fyfield Books. Routledge, (2003).
- [4] In *Early Work (1905-1911)*, Rosenfeld, L. and Nielsen, J. R., editors, volume 1 of *Niels Bohr Collected Works*, 163–393. Elsevier (1972).
- [5] Van Leeuwen, H. J. *J. Phys. Radium* **2**(12), 361–377 (1921).
- [6] Feynman, R. P., Leighton, R. B., and Sands, M. *The Feynman Lectures on Physics: Mainly Mechanics, Radiation, and Heat*. Basic Books, (2011).
- [7] Baibich, M. N., Broto, J., Fert, A., Van Dau, F. N., Petroff, F., Etienne, P., Creuzet, G., Friederich, A., and Chazelas, J. *Phys. Rev. Lett.* **61**(21), 2472 (1988).
- [8] Binasch, G., Grünberg, P., Saurenbach, F., and Zinn, W. *Phys. Rev. B* **39**, 4828–4830 (1989).
- [9] Butler, W. H., Zhang, X.-G., Schulthess, T. C., and MacLaren, J. *Phys. Rev. B* **63**(5), 054416 (2001).
- [10] Mathon, J. and Umerski, A. *Phys. Rev. B* **63**(22), 220403 (2001).

- [11] Yuasa, S., Nagahama, T., Fukushima, A., Suzuki, Y., and Ando, K. *Nat. Mater.* **3**(12), 868–871 (2004).
- [12] Parkin, S. S. P., Kaiser, C., Panchula, A., Rice, P. M., Hughes, B., Samant, M., and Yang, S.-H. *Nat. Mater.* **3**(12), 862–867 (2004).
- [13] Ikeda, S., Hayakawa, J., Ashizawa, Y., Lee, Y., Miura, K., Hasegawa, H., Tsunoda, M., Matsukura, F., and Ohno, H. *Appl. Phys. Lett.* **93**(8), 082508–082508 (2008).
- [14] Žutić, I., Fabian, J., and Sarma, S. D. *Rev. Mod. Phys.* **76**(2), 323 (2004).
- [15] Slonczewski, J. C. *J. Magn. Magn. Mater.* **159**(1), L1–L7 (1996).
- [16] Ralph, D. C. and Stiles, M. D. *J. Magn. Magn. Mater.* **320**(7), 1190–1216 (2008).
- [17] Everspin Technologies. Press release, Nov (2012). http://www.everspin.com/PDF/ST-MRAM_Press_Release.pdf.
- [18] Hirsch, J. E. *Phys. Rev. Lett.* **83**(9), 1834 (1999).
- [19] Kato, Y. K., Myers, R. C., Gossard, A. C., and Awschalom, D. D. *Science* **306**(5703), 1910–1913 (2004).
- [20] Wunderlich, J., Kaestner, B., Sinova, J., and Jungwirth, T. *Phys. Rev. Lett.* **94**(4), 047204 (2005).
- [21] Dyakonov, M. I. and Perel, V. I. *J. Exp. Theor. Phys. Lett.* **13**, 467 (1971).
- [22] Dyakonov, M. I. and Perel, V. I. *Phys. Lett. A* **35**(6), 459–460 (1971).
- [23] Liu, L., Moriyama, T., Ralph, D. C., and Buhrman, R. A. *Phys. Rev. Lett.* **106**(3), 036601 (2011).
- [24] Liu, L., Pai, C.-F., Li, Y., Tseng, H. W., Ralph, D. C., and Buhrman, R. A. *Science* **336**(6081), 555–558 (2012).
- [25] Dresselhaus, G. *Phys. Rev.* **100**(2), 580–586 (1955).

-
- [26] Stein, D., Klitzing, K. v., and Weimann, G. *Phys. Rev. Lett.* **51**(2), 130 (1983).
- [27] Bychkov, Y. A. and Rashba, E. I. *J. Exp. Theor. Phys. Lett.* **39**(2), 78 (1984).
- [28] Bychkov, Y. A. and Rashba, E. I. *J. Phys. C: Solid State Phys.* **17**(33), 6039 (1984).
- [29] Ganichev, S. D., Ivchenko, E. L., Bel’Kov, V. V., Tarasenko, S. A., Sollinger, M., Weiss, D., Wegscheider, W., and Prettl, W. *Nature* **417**(6885), 153–156 (2002).
- [30] Edelstein, V. M. *Solid State Commun.* **73**(3), 233–235 (1990).
- [31] Chernyshov, A., Overby, M., Liu, X., Furdyna, J. K., Lyanda-Geller, Y., and Rokhinson, L. P. *Nature Phys.* **5**(9), 656–659 (2009).
- [32] Pi, U. H., Won Kim, K., Bae, J. Y., Lee, S. C., Cho, Y. J., Kim, K. S., and Seo, S. *Appl. Phys. Lett.* **97**(16), 162507–162507 (2010).
- [33] Kim, J., Sinha, J., Hayashi, M., Yamanouchi, M., Fukami, S., Suzuki, T., Mitani, S., and Ohno, H. *Nat. Mater.* **12**(3), 240–245 (2013).
- [34] Garello, K., Miron, I. M., Avci, C. O., Freimuth, F., Mokrousov, Y., Blügel, S., Auffret, S., Boule, O., Gaudin, G., and Gambardella, P. *Nat. Nanotechnol.* **8**(8), 587–593 (2013).
- [35] Fan, X., Wu, J., Chen, Y., Jerry, M. J., Zhang, H., and Xiao, J. Q. *Nat. Commun.* **4**, 1799 (2013).
- [36] Fan, X., Celik, H., Wu, J., Ni, C., Lee, K.-J., Lorenz, V. O., and Xiao, J. Q. *Nat. Commun.* **5** (2014).
- [37] Sim, C. H., Huang, J. C., Tran, M., and Eason, K. *Appl. Phys. Lett.* **104**(1), 012408 (2014).
- [38] Endo, M., Matsukura, F., and Ohno, H. *Appl. Phys. Lett.* **97**(22), 222501–222501 (2010).

- [39] Miron, I. M., Gaudin, G., Auffret, S., Rodmacq, B., Schuhl, A., Pizzini, S., Vogel, J., and Gambardella, P. *Nat. Mater.* **9**(3), 230–234 (2010).
- [40] Miron, I. M., Garello, K., Gaudin, G., Zermatten, P.-J., Costache, M. V., Auffret, S., Bandiera, S., Rodmacq, B., Schuhl, A., and Gambardella, P. *Nature* **476**(7359), 189–193 (2011).
- [41] Liu, L., Lee, O. J., Gudmundsen, T. J., Ralph, D. C., and Buhrman, R. A. *Phys. Rev. Lett.* **109**, 096602 (2012).
- [42] Avci, C. O., Garello, K., Miron, I. M., Gaudin, G., Auffret, S., Boulle, O., and Gambardella, P. *Appl. Phys. Lett.* **100**(21), 212404 (2012).
- [43] Cubukcu, M., Boulle, O., Drouard, M., Garello, K., Avci, C. O., Miron, I. M., Langer, J., Ocker, B., Gambardella, P., and Gaudin, G. *Appl. Phys. Lett.* **104**(4), 042406 (2014).
- [44] Zhang, C., Yamanouchi, M., Sato, H., Fukami, S., Ikeda, S., Matsukura, F., and Ohno, H. *J. Appl. Phys.* **115**(17), 17C714 (2014).
- [45] Fang, D., Kurebayashi, H., Wunderlich, J., Vybourný, K., Zârbo, L. P., Campion, R. P., Casiraghi, A., Gallagher, B. L., Jungwirth, T., and Ferguson, A. J. *Nat. Nanotechnol.* **6**(7), 413–417 (2011).
- [46] Pai, C.-F., Liu, L., Li, Y., Tseng, H. W., Ralph, D. C., and Buhrman, R. A. *Appl. Phys. Lett.* **101**(12), 122404 (2012).
- [47] Kondou, K., Sukegawa, H., Mitani, S., Tsukagoshi, K., and Kasai, S. *Appl. Phys. Express* **5**(7), 073002 (2012).
- [48] Skinner, T. D., Wang, M., Hindmarch, A. T., Rushforth, A. W., Irvine, A. C., Heiss, D., Kurebayashi, H., and Ferguson, A. J. *Appl. Phys. Lett.* **104**(6), 062401–062401–4 (2014).
- [49] Kurebayashi, H., Sinova, J., Fang, D., Irvine, A. C., Skinner, T. D., Wunderlich, J., Novák, V., Campion, R. P., Gallagher, B. L., Vohstetdt, E. K., Zarbo, L. P., Vyborny, K., Ferguson, A. J., and Jungwirth, T. *Nat. Nanotechnol.* (2014).

-
- [50] Miron, I. M., Moore, T., Szambolics, H., Buda-Prejbeanu, L. D., Auffret, S., Rodmacq, B., Pizzini, S., Vogel, J., Bonfim, M., Schuhl, A., and Gaudin, G. *Nat. Mater.* **10**(6), 419–423 (2011).
- [51] Zhang, S., Levy, P. M., and Fert, A. *Phys. Rev. Lett.* **88**, 236601 (2002).
- [52] Zimmerler, M. A., Özyilmaz, B., Chen, W., Kent, A. D., Sun, J. Z., Rooks, M. J., and Koch, R. H. *Phys. Rev. B* **70**, 184438 (2004).
- [53] Sankey, J. C., Cui, Y.-T., Sun, J. Z., Slonczewski, J. C., Buhrman, R. A., and Ralph, D. C. *Nature Phys.* **4**(1), 67–71 (2007).
- [54] Costache, M. V., Sladkov, M., Watts, S. M., van der Wal, C. H., and van Wees, B. J. *Phys. Rev. Lett.* **97**, 216603 (2006).
- [55] Ando, K., Kajiwara, Y., Takahashi, S., Maekawa, S., Takemoto, K., Takatsu, M., and Saitoh, E. *Phys. Rev. B* **78**, 014413 (2008).
- [56] Mosendz, O., Vlaminck, V., Pearson, J. E., Fradin, F. Y., Bauer, G. E. W., Bader, S. D., and Hoffmann, A. *Phys. Rev. B* **82**, 214403 (2010).
- [57] Czeschka, F. D., Dreher, L., Brandt, M. S., Weiler, M., Althammer, M., Imort, I.-M., Reiss, G., Thomas, A., Schoch, W., Limmer, W., Huebl, H., Gross, R., and Goennenwein, S. T. B. *Phys. Rev. Lett.* **107**, 046601 (2011).
- [58] Ando, K., Takahashi, S., Ieda, J., Kurebayashi, H., Trypiniotis, T., Barnes, C. H. W., Maekawa, S., and Saitoh, E. *Nat. Mater.* **10**(9), 655–659 (2011).
- [59] Kimura, T., Otani, Y., Sato, T., Takahashi, S., and Maekawa, S. *Phys. Rev. Lett.* **98**, 156601 (2007).
- [60] Johnson, M. T., Bloemen, P. J. H., den Broeder, F. J. A., and de Vries, J. J. *Rep. Prog. Phys.* **59**, 14091458 (1996).
- [61] Liu, X. and Furdyna, J. K. *J. Phys.: Condens. Matter* **18**(13), R245 (2006).
- [62] Farle, M. *Rep. Prog. Phys.* **61**(7), 755 (1998).

- [63] Heinrich, B., Cochran, J. F., Arrott, A. S., Purcell, S. T., Urquhart, K. B., Dutcher, J. R., and Egelhoff, W. F. *Appl. Phys. A Mater. Sci. Process.* **49**, 473–490 (1989).
- [64] Yang, F. Y., Chien, C. L., Ferrari, E. F., Li, X. W., Xiao, G., and Gupta, A. *Appl. Phys. Lett.* **77**(2), 286–288 (2000).
- [65] Ikeda, S., Hayakawa, J., Lee, Y. M., Matsukura, F., Ohno, Y., Hanyu, T., and Ohno, H. *IEEE Trans. Electron Dev.* **54**(5), 991–1002 (2007).
- [66] Mangin, S., Ravelosona, D., Katine, J. A., Carey, M. J., Terris, B. D., and Fullerton, E. E. *Nat. Mater.* **5**(3), 210–215 (2006).
- [67] Ikeda, S., Miura, K., Yamamoto, H., Mizunuma, K., Gan, H. D., Endo, M., Kanai, S., Hayakawa, J., Matsukura, F., and Ohno, H. *Nature Mater.* **9**(9), 721–724 (2010).
- [68] Kittel, C. *Phys. Rev.* **73**(2), 155–161 (1948).
- [69] Gilbert, T. L. *IEEE Trans. Magn.* **40**(6), 3443 – 3449 (2004).
- [70] Dorman, V. L. and Sobolev, V. L. *J. Phys. C: Solid State Phys.* **21**(33), 5663 (1988).
- [71] Suhl, H. *Phys. Rev.* **97**(2), 555–557 (1955).
- [72] Liu, X., Sasaki, Y., and Furdyna, J. K. *Phys. Rev. B* **67**(20), 205204 (2003).
- [73] Thomson, W. *Proc. R. Soc.* **8**, 546–550 (1856).
- [74] McGuire, T. and Potter, R. *IEEE Trans. Magn.* **11**(4), 1018–1038 (1975).
- [75] Jan, J.-P. *Solid State Phys.* **5**, 1–96 (1957).
- [76] Mott, N. F. *Proc. R. Soc. A* **156**(888), 368–382 (1936).
- [77] Smit, J. *Physica* **17**(6), 612–627 (1951).
- [78] Pugh, E. M. *Phys. Rev.* **36**, 1503–1511 (1930).

-
- [79] Nagaosa, N., Sinova, J., Onoda, S., MacDonald, A. H., and Ong, N. P. *Rev. Mod. Phys.* **82**, 1539–1592 (2010).
- [80] Smit, J. *Physica* **24**(1), 39–51 (1958).
- [81] Berger, L. *Phys. Rev. B* **2**, 4559–4566 (1970).
- [82] Karplus, R. and Luttinger, J. M. *Phys. Rev.* **95**, 1154–1160 (1954).
- [83] Jungwirth, T., Niu, Q., and MacDonald, A. H. *Phys. Rev. Lett.* **88**, 207208 (2002).
- [84] Julliere, M. *Physics Lett. A* **54**(3), 225 – 226 (1975).
- [85] Yuasa, S. and Djayaprawira, D. D. *J. Phys. D: Appl. Phys.* **40**(21), R337 (2007).
- [86] Miyazaki, T. and Tezuka, N. *J. Magn. Magn. Mater.* **139**(3), L231 – L234 (1995).
- [87] Moodera, J. S., Kinder, L. R., Wong, T. M., and Meservey, R. *Phys. Rev. Lett.* **74**, 3273–3276 (1995).
- [88] Lee, Y. M., Hayakawa, J., Ikeda, S., Matsukura, F., and Ohno, H. *Appl. Phys. Lett.* **90**(21), 212507 (2007).
- [89] Sinova, J., Culcer, D., Niu, Q., Sinitsyn, N. A., Jungwirth, T., and MacDonald, A. H. *Phys. Rev. Lett.* **92**, 126603 (2004).
- [90] Moodera, J. S., Santos, T. S., and Nagahama, T. *J. Phys.: Condens. Matter* **19**(16), 165202 (2007).
- [91] Vouille, C., Barthélémy, A., Elokani Mpondo, F., Fert, A., Schroeder, P. A., Hsu, S. Y., Reilly, A., and Loloee, R. *Phys. Rev. B* **60**, 6710–6722 (1999).
- [92] Parkin, S. S. P., Roche, K. P., Samant, M. G., Rice, P. M., Beyers, R. B., Scheuerlein, R. E., O’Sullivan, E. J., Brown, S. L., Bucchigano, J., Abraham, D. W., Lu, Y., Rooks, M., Trouilloud, P. L., Wanner, R. A., and Gallagher, W. J. *J. Appl. Phys.* **85**(8), 5828–5833 (1999).

- [93] Butler, W. H. *Sci. Tech. Adv. Mater.* **9**(1), 014106 (2008).
- [94] Li, Z., Zhang, S., Diao, Z., Ding, Y., Tang, X., Apalkov, D. M., Yang, Z., Kawabata, K., and Huai, Y. *Phys. Rev. Lett.* **100**, 246602 (2008).
- [95] Gradhand, M., Fedorov, D. V., Zahn, P., and Mertig, I. *Phys. Rev. Lett.* **104**, 186403 (2010).
- [96] Guo, G. Y., Murakami, S., Chen, T.-W., and Nagaosa, N. *Phys. Rev. Lett.* **100**, 096401 (2008).
- [97] Resta, R. *J. Phys.: Condens. Matter* **22**(12), 123201 (2010).
- [98] Liu, L., Buhrman, R. A., and Ralph, D. C. *preprint arXiv:1111.3702* (2011).
- [99] Tserkovnyak, Y., Brataas, A., and Bauer, G. E. W. *Phys. Rev. Lett.* **88**, 117601 (2002).
- [100] Brataas, A., Tserkovnyak, Y., Bauer, G. E., and Kelly, P. J. *preprint arXiv:1108.0385* (2011).
- [101] Mizukami, S., Ando, Y., and Miyazaki, T. *Phys. Rev. B* **66**, 104413 (2002).
- [102] Ando, K., Takahashi, S., Ieda, J., Kajiwara, Y., Nakayama, H., Yoshino, T., Harii, K., Fujikawa, Y., Matsuo, M., Maekawa, S., and Saitoh, E. *J. Appl. Phys.* **109**(10), 103913 (2011).
- [103] Jacquod, P., Whitney, R. S., Meair, J., and Büttiker, M. *Phys. Rev. B* **86**, 155118 (2012).
- [104] Inoue, H. Y., Harii, K., Ando, K., Sasage, K., and Saitoh, E. *J. Appl. Phys.* **102**(8), 083915 (2007).
- [105] Saitoh, E., Ueda, M., Miyajima, H., and Tatara, G. *Appl. Phys. Lett.* **88**(18), 182509 (2006).
- [106] Mosendz, O., Pearson, J. E., Fradin, F. Y., Bauer, G. E. W., Bader, S. D., and Hoffmann, A. *Phys. Rev. Lett.* **104**, 046601 (2010).
- [107] Kato, Y. K. and Awschalom, D. D. *J. Phys. Soc. Jpn.* **77**(3), 031006 (2008).

-
- [108] La Rocca, G. C., Kim, N., and Rodriguez, S. *Phys. Rev. B* **38**(11), 7595–7601 (1988).
- [109] Silver, M., Batty, W., Ghiti, A., and O’Reilly, E. P. *Phys. Rev. B* **46**, 6781–6788 (1992).
- [110] Silov, A. Y., Blajnov, P. A., Wolter, J. H., Hey, R., Ploog, K. H., and Averkiev, N. S. *Appl. Phys. Lett.* **85**(24), 5929–5931 (2004).
- [111] Manchon, A. and Zhang, S. *Phys. Rev. B* **79**(9), 094422 (2009).
- [112] Garate, I. and MacDonald, A. H. *Phys. Rev. B* **80**, 134403 (2009).
- [113] Wang, X. and Manchon, A. *Phys. Rev. Lett.* **108**(11), 117201 (2012).
- [114] Pesin, D. A. and MacDonald, A. H. *Phys. Rev. B* **86**, 014416 (2012).
- [115] Hayashi, T., Hashimoto, Y., Katsumoto, S., and Iye, Y. *Appl. Phys. Lett.* **78**(12), 1691–1693 (2001).
- [116] Ohno, H., Shen, A., Matsukura, F., Oiwa, A., Endo, A., Katsumoto, S., and Iye, Y. *Appl. Phys. Lett.* **69**(3), 363–365 (1996).
- [117] Jungwirth, T., Sinova, J., Mašek, J., Kučera, J., and MacDonald, A. H. *Rev. Mod. Phys.* **78**(3), 809–864 (2006).
- [118] Van Esch, A., Van Bockstal, L., De Boeck, J., Verbanck, G., van Steenberghe, A. S., Wellmann, P. J., Grietens, B., Bogaerts, R., Herlach, F., and Borghs, G. *Phys. Rev. B* **56**(20), 13103–13112 (1997).
- [119] Edmonds, K. W., Bogusławski, P., Wang, K. Y., Champion, R. P., Novikov, S. N., Farley, N. R. S., Gallagher, B. L., Foxon, C. T., Sawicki, M., Dietl, T., Buongiorno Nardelli, M., and Bernholc, J. *Phys. Rev. Lett.* **92**(3), 037201 (2004).
- [120] Wang, M., Champion, R. P., Rushforth, A. W., Edmonds, K. W., Foxon, C. T., and Gallagher, B. L. *Appl. Phys. Lett.* **93**(13), 132103 (2008).
- [121] Braunstein, R. and Kane, E. *J. Phys. Chem. Solids* **23**(10), 1423 – 1431 (1962).

- [122] Lim, W. L., Wojtowicz, T., Liu, X., Dobrowolska, M., and Furdyna, J. K. *Physica E* **20**(3-4), 346 – 349 (2004).
- [123] Jungwirth, T., Novák, V., Martí, X., Cukr, M., Máca, F., Shick, A. B., Mašek, J., Horodyská, P., Němec, P., Holý, V., Zemek, J., Kužel, P., Němec, I., Gallagher, B. L., Campion, R. P., Foxon, C. T., and Wunderlich, J. *Phys. Rev. B* **83**(3), 035321 (2011).
- [124] Novák, V., Cukr, M., Sobán, Z., Jungwirth, T., Martí, X., Holý, V., Horodyská, P., and Nemeč, P. *J. Cryst. Growth* **323**(1), 348 – 350 (2011).
- [125] Park, B. G., Wunderlich, J., Martí, X., Holy, V., Kurosaki, Y., Yamada, M., Yamamoto, H., Nishide, A., Hayakawa, J., Takahashi, H., Shick, A. B., and Jungwirth, T. *Nat. Mater.* **10**(5), 347–351 (2011).
- [126] Shick, A. B., Khmelevskiy, S., Mryasov, O. N., Wunderlich, J., and Jungwirth, T. *Phys. Rev. B* **81**(21), 212409 (2010).
- [127] Manchon, A., Ducruet, C., Lombard, L., Auffret, S., Rodmacq, B., Dieny, B., Pizzini, S., Vogel, J., Uhlir, V., Hochstrasser, M., and Panaccione, G. *J. Appl. Phys.* **104**(4), 043914 (2008).
- [128] Costache, M. V., Sladkov, M., van der Wal, C. H., and van Wees, B. J. *Appl. Phys. Lett.* **89**(19), 192506 (2006).
- [129] Costache, M. V., Watts, S. M., Sladkov, M., van der Wal, C. H., and van Wees, B. J. *Appl. Phys. Lett.* **89**(23), 232115 (2006).
- [130] Yamaguchi, A., Motoi, K., Hirohata, A., Miyajima, H., Miyashita, Y., and Sanada, Y. *Phys. Rev. B* **78**(10), 104401 (2008).
- [131] Mecking, N., Gui, Y. S., and Hu, C.-M. *Phys. Rev. B* **76**(22), 224430 (2007).
- [132] Azevedo, A. and Vilela-Leão, L. H. and Rodríguez-Suárez, R. L. and Lacerda Santos, A. F. and Rezende, S. M. *Phys. Rev. B* **83**, 144402 (2011).
- [133] Feng, Z., Hu, J., Sun, L., You, B., Wu, D., Du, J., Zhang, W., Hu, A., Yang, Y., Tang, D. M., Zhang, B. S., and Ding, H. F. *Phys. Rev. B* **85**, 214423 (2012).

-
- [134] Bai, L., Hyde, P., Gui, Y. S., Hu, C.-M., Vlaminck, V., Pearson, J. E., Bader, S. D., and Hoffmann, A. *Phys. Rev. Lett.* **111**, 217602 (2013).
- [135] Harder, M., Cao, Z., Gui, Y., Fan, X., and Hu, C.-M. *Phys. Rev. B* **84**(5), 054423 (2011).
- [136] Bai, L., Feng, Z., Hyde, P., Ding, H. F., and Hu, C. M. *Appl. Phys. Lett.* **102**, 242402 (2013).
- [137] Nakayama, H., Ando, K., Harii, K., Yoshino, T., Takahashi, R., Kajiwara, Y., Uchida, K., Fujikawa, Y., and Saitoh, E. *Phys. Rev. B* **85**, 144408 (2012).
- [138] Draaisma, H., de Jonge, W., and den Broeder, F. *J. Magn. Magn. Mater.* **66**(3), 351 – 355 (1987).
- [139] Gu, B., Sugai, I., Ziman, T., Guo, G. Y., Nagaosa, N., Seki, T., Takanashi, K., and Maekawa, S. *Phys. Rev. Lett.* **105**, 216401 (2010).
- [140] Niimi, Y., Kawanishi, Y., Wei, D. H., Deranlot, C., Yang, H. X., Chshiev, M., Valet, T., Fert, A., and Otani, Y. *Phys. Rev. Lett.* **109**, 156602 (2012).
- [141] Berger, L. *Phys. Rev. B* **54**, 9353–9358 (1996).
- [142] Manchon, A. and Zhang, S. *Phys. Rev. B* **78**, 212405 (2008).
- [143] Obata, K. and Tataru, G. *Phys. Rev. B* **77**, 214429 (2008).
- [144] Suzuki, T., Fukami, S., Ishiwata, N., Yamanouchi, M., Ikeda, S., Kasai, N., and Ohno, H. *Appl. Phys. Lett.* **98**(14), – (2011).
- [145] Fang, D., Skinner, T. D., Kurebayashi, H., Champion, R. P., Gallagher, B. L., and Ferguson, A. J. *Appl. Phys. Lett.* **101**(18), 182402–182402 (2012).
- [146] Wiedwald, U., Spasova, M., Farle, M., Hilgendorff, M., and Giersig, M. *J. Vac. Sci. Technol., A* **19**(4), 1773–1776 (2001).
- [147] Ortiz Pauyac, C., Wang, X., Chshiev, M., and Manchon, A. *Appl. Phys. Lett.* **102**(25) (2013).
- [148] Zhang, W., Vlaminck, V., Pearson, J. E., Divan, R., Bader, S. D., and Hoffmann, A. *Appl. Phys. Lett.* **103**(24), 242414 (2013).

- [149] Ganichev, S. D., Belkov, V. V., Golub, L. E., Ivchenko, E. L., Schneider, P., Giglberger, S., Eroms, J., De Boeck, J., Borghs, G., Wegscheider, W., Weiss, D., and Prettl, W. *Phys. Rev. Lett.* **92**(25), 256601 (2004).
- [150] Pal, A. K., Chaudhuri, S., and Barua, A. K. *J. Phys. D: Appl. Phys.* **9**(15), 2261 (1976).
- [151] De Vries, J. W. C. *Thin Solid Films* **167**(1), 25–32 (1988).
- [152] Bernevig, B. A. and Vafeek, O. *Phys. Rev. B* **72**(3), 33203 (2005).
- [153] Olejnik, K., Wadley, P., Haigh, J. A., Edmonds, K. W., Champion, R. P., Rushforth, A. W., Gallagher, B. L., Foxon, C. T., Jungwirth, T., Wunderlich, J., Dhessi, S. S., Cavill, S. A., van der Laan, G., and Arenholz, E. *Phys. Rev. B* **81**(10), 104402 (2010).
- [154] Maccherozzi, F., Sperl, M., Panaccione, G., Minár, J., Polesya, S., Ebert, H., Wurstbauer, U., Hochstrasser, M., Rossi, G., Woltersdorf, G., Wegscheider, W., and Back, C. H. *Phys. Rev. Lett.* **101**(26), 267201 (2008).
- [155] Sperl, M., Maccherozzi, F., Borgatti, F., Verna, A., Rossi, G., Soda, M., Schuh, D., Bayreuther, G., Wegscheider, W., Cezar, J. C., Yakhov, F., Brookes, N. B., Back, C. H., and Panaccione, G. *Phys. Rev. B* **81**(3), 035211 (2010).
- [156] Menshov, V. N., Tugushev, V. V., Caprara, S., and Chulkov, E. V. *Phys. Rev. B* **81**(23), 235212 (2010).
- [157] Scott, G. G. *Phys. Rev.* **82**(4), 542 (1951).
- [158] Birowska, M., Śliwa, C., Majewski, J. A., and Dietl, T. *Phys. Rev. Lett.* **108**(23), 237203 (2012).
- [159] Dietl, T., Ohno, H., Matsukura, F., Cibert, J., and Ferrand, D. *Science* **287**(5455), 1019–1022 (2000).
- [160] Berciu, M. and Bhatt, R. N. *Phys. Rev. Lett.* **87**(10), 107203 (2001).
- [161] Chen, L., Matsukura, F., and Ohno, H. *Nat. Commun.* **4** (2013).

- [162] Dzyaloshinsky, I. *J. Phys. Chem. Solids* **4**(4), 241–255 (1958).
- [163] Moriya, T. *Phys. Rev.* **120**(1), 91 (1960).
- [164] Ryu, K.-S., Thomas, L., Yang, S.-H., and Parkin, S. S. P. *Nat. Nanotechnol.* **8**(7), 527–533 (2013).
- [165] Emori, S., Bauer, U., Ahn, S.-M., Martinez, E., and Beach, G. S. D. *Nat. Mater.* **12**(7), 611–616 (2013).
- [166] Emori, S., Martinez, E., Bauer, U., Ahn, S.-M., Agrawal, P., Bono, D. C., and Beach, G. S. D. *preprint arXiv:1308.1432* (2013).
- [167] Perez, N., Martinez, E., Torres, L., Woo, S.-H., Emori, S., and Beach, G. S. D. *preprint arXiv:1401.3526* (2014).
- [168] Ishikawa, Y., Tajima, K., Bloch, D., and Roth, M. *Solid State Commun.* **19**(6), 525–528 (1976).
- [169] Mellnik, A. R., Lee, J. S., Richardella, A., Grab, J. L., Mintun, P. J., Fischer, M. H., Vaezi, A., Manchon, A., Kim, E.-A., Samarth, N., and C, R. D. *preprint arXiv:1402.1124* (2014).
- [170] Pozar, D. M. *Microwave engineering*. John Wiley & Sons, (2009).
- [171] Lee, T. H. *Planar Microwave Engineering: A Practical Guide to Theory, Measurement, and Circuits*. Cambridge University Press, (2004).